



**HAL**  
open science

# Role of seepage forces on hydraulic fracturing and failure patterns

Alexander Rozhko

► **To cite this version:**

Alexander Rozhko. Role of seepage forces on hydraulic fracturing and failure patterns. Geophysics [physics.geo-ph]. Université Joseph-Fourier - Grenoble I, 2007. English. NNT: . tel-00179530

**HAL Id: tel-00179530**

**<https://theses.hal.science/tel-00179530>**

Submitted on 15 Oct 2007

**HAL** is a multi-disciplinary open access archive for the deposit and dissemination of scientific research documents, whether they are published or not. The documents may come from teaching and research institutions in France or abroad, or from public or private research centers.

L'archive ouverte pluridisciplinaire **HAL**, est destinée au dépôt et à la diffusion de documents scientifiques de niveau recherche, publiés ou non, émanant des établissements d'enseignement et de recherche français ou étrangers, des laboratoires publics ou privés.



# **Role of seepage forces on hydraulic fracturing and failure patterns**

**Alexander Rozhko**

**Thesis submitted for the degree of Philosophiae Doctor  
Department of Physics University of Oslo, Norway**

**Thèse présentée pour obtenir le titre de docteur de  
l'Université Joseph Fourier - Grenoble I - France  
Spécialité: Sciences de la Terre et de l'Univers**

Ph. D. committee:

Pr. Bjorn Jamtveit, Professor, University of Oslo

Pr. Steve Miller, Professor, University of Bonn

Pr. Chaouqi Misbah, Directeur de Recherche, University of Grenoble

**September 2007**

## **Preface**

The work presented in this dissertation was conducted at the Department of Physics, University of Oslo in collaboration with the Department of Geosciences, Universite Joseph Fourier, Grenoble, during a period of three years.

I would like to thank my main supervisor, Professor Yuri Podladchikov, for shearing his knowledge, giving valuable criticism and inspiration. Many thanks to my second supervisor, Professor Francois Renard, for his advices, continuous encouragement and motivation. Special thanks to Dr. Galen Gisler for the proof reading and corrections of the scientific manuscripts.

Many thanks to Filip Nicolaisen and Christophe Calerne for being very nice officemates and friends. I am also very grateful towards all people who work and study at PGP for the rich scientific arguments and informal discussions.

During this work I was happy to receive a full financial support from PGP (Physics of Geological Processes), a Norwegian Center of Excellence at University of Oslo.

Finally, thanks to my wife Jana and son Ivan for their love, patience and support during my PhD education.

Alexander Rozhko

September 2007

## **Role of seepage forces on hydraulic fracturing and failure patterns**

**Abstract.** The mechanical role of seepage forces on hydraulic fracturing and failure patterns was studied both by the analytical methods of the continuum mechanics and by numerical simulations. Seepage forces are frictional forces caused by gradients of pore-fluid pressure. Formation of different failure patterns (localized shear bands or tensile fractures) driven by the localized fluid overpressure in the poro-elasto-plastic medium was studied using a numerical code specially developed for this purpose. The pre-failure condition for different failure patterns and fluid pressure at the failure onset was predicted using a new analytical solution.

In the analytical solution the elliptical cavity filled with fluid in the non-hydrostatic far-field stress-state is considered. Since, the fluid pressure inside cavity differs from the far-field pore-fluid pressure; the poroelastic coupling is taking into account in the calculation of the deformation. Using Griffith's theory for failure and this analytical solution, the generalized equation for the effective stress law was obtained. This generalized effective stress law controls the failure in the fluid-saturated porous medium with a non-homogeneous fluid pressure distribution.

## **Rôle des forces de succion sur le mode de fracturation des roches en présence de fluides**

**Résumé.** L'effet mécanique des forces de succion, forces exercées par un fluide qui se déplace dans un milieu poreux, a été étudié dans le cadre de la fracturation hydraulique des roches de la croûte terrestre. Cet effet a été étudié par des méthodes analytiques issues de la mécanique des milieux continus, et par des simulations numériques. Ces forces de succion sont des forces de frottement causées par des gradients de pression fluide dans les milieux poreux. Différents modes de fracturation (bandes de cisaillement localisées, fractures en mode I) causés par une augmentation localisée de la pression fluide dans la croûte ont été reproduits dans un milieu poro-élastique grâce à plusieurs codes numériques spécialement développés à cet effet. La valeur de la pression fluide lors de la nucléation de la fracturation est aussi prédite à l'aide d'une nouvelle solution analytique.

Dans la solution analytique, une cavité elliptique dans un solide poreux est remplie avec un fluide à une pression non-hydrostatique. On considère aussi que le milieu poreux est soumis à un champ de contrainte externe. Puisque la pression du

fluide dans la cavité est différente de la pression de pore dans la roche; le couplage poro-élastique est pris en compte dans le calcul des déformations. A partir de la théorie de Griffith qui donne une condition pour la propagation d'une fracture, et en utilisant la solution analytique obtenue, une équation généralisée a été obtenue pour la contrainte effective dans le milieu. Cette nouvelle loi décrit la fracturation dans un milieu poreux saturé avec un fluide, et dans lequel la distribution de pression fluide n'est pas homogène.

## CONTENTS

<b>Preface</b>	<b>i</b>
<b>Abstract</b>	<b>ii</b>
<b>Contents</b>	<b>iv</b>
<b>Part I Theory</b>	<b>1</b>
<b>1. Introduction</b>	<b>2</b>
<b>2. Theoretical foundations</b>	<b>4</b>
2.1 Poroelasticity and thermoelasticity	5
2.2 Pore-fluid pressure effect on deformation and failure	6
2.3 Failure envelope for rock	7
2.4 Poro-elasto-plasticity	8
2.5 Linear poro-elastic fracture mechanics	10
<b>3. Summary of the papers</b>	<b>13</b>
Resume of Paper I	13
Resume of Paper II	13
Resume of Paper III	14
Resume of Paper IV	15
<b>Bibliography</b>	<b>17</b>
<b>Appendix</b> The numerical modeling of the fluid flow in a porous elastoplastic medium (MatLab code)	<b>19</b>
<b>Part II Scientific papers</b>	<b>28</b>

**Paper 1:** A.Y. Rozhko, Y.Y. Podladchikov, and F. Renard, Failure patterns caused by localized rise in pore-fluid overpressure and effective strength of rocks, *accepted for publication in Geophysical Research Letters*.

**Paper 2:** A.Y. Rozhko, Role of seepage forces in faulting and earthquake triggering, *submitted to Tectonophysics*.

**Paper 3:** A.Y. Rozhko and Y.Y. Podladchikov, Role of fluid diffusion on failure and effective stress of porous solids, *in preparation*.

**Paper 4:** A.Y. Rozhko, Hydraulic fracturing of elliptical boreholes and stress measurements in a highly permeable poroelastic reservoirs, *in preparation*.

**Scientific advisors:**

Professor Yuri Podladchikov

Professor Francois Renard



## **Part I Theory**

## 1. INTRODUCTION

In this dissertation I will study the role of *gradients of pore-fluid pressure* on the mechanical strength and failure patterns of the porous, fluid saturated materials. Mechanical role of *pore-fluid pressure* on the failure is well recognized nowadays in the literature, starting from the pioneering work of [Von Terzaghi \[1943\]](#), who demonstrated on the experimental ground that the failure of the fluid saturated porous material is controlled by the effective stress that is equal to the total stress minus fluid pressure. Later [Murrell \[1964\]](#) applied [Griffith's theory \[1920\]](#) to the elliptical crack, filled with fluid and demonstrated that Terzaghi's effective stress principle follows from Griffith's theory of failure. However, the mechanical role of *gradients of pore-fluid pressure* on failure is not well recognized. Since, it is common to assume that for any variation in pore-fluid pressure, the total stresses are constant. Such an assumption is not always warranted; because the gradients in pore-fluid overpressure create seepage forces and that these seepage forces modify the total stresses. The recent publications of [[Mourgues and Cobbold, 2003](#); [Cobbold and Rodrigues, 2007](#)] show the experimental evidence that the seepage forces have a strong effect on the initiation and direction of propagation for both shear and tensile fractures. In addition, there is a recent experimental evidence that the aftershocks can be triggered by the local decrease of the fluid pressure on the fault zone [[Miller et al, 2004](#)], these may be explained by the rise of seepage forces due to the pore-fluid pressure gradients.

Since most of the materials like rocks, soils, concretes and human bones are porous with a non-homogeneous fluid-pressure distribution, it is very important to understand the role of pore-fluid pressure gradients on the mechanical strength and possible failure patterns, developed during a mechanical failure. In this dissertation I made an attempt to improve the understanding of mechanical role of pore-fluid pressure gradients on failure. The investigation was conducted both by the analytical methods of the continuum mechanics and by numerical simulations. In order to study a possible failure patterns, driven by pore-fluid pressure gradients, I have developed two numerical codes (finite difference and finite element) that allowed me to model both tensile and shear fractures in porous elastoplastic medium. In order to predict the pre-failure condition I have developed two analytical solutions in which I calculated the seepage forces around the open and closed elliptical crack. These analytical solutions are developed using a Complex potentials method [[Muskhelishvili, 1977](#); [Timoshenko](#)

*and Godier,1982*] applied to the linear poroelastic medium [*Biot, 1941; Rice and Cleary, 1976*]. Applying a new analytical solution in the Griffith's theory of failure, I have found a new effective stress law that governs the failure in a porous solid with a non-homogeneous fluid pressure distribution.

The dissertation has two parts: the theory and the scientific manuscripts. In the first part of the thesis I briefly introduce the theoretical background in the context of the previous works, the overview of the literature and the main results of the thesis. In the appendix I present the numerical code which was developed to study the failure patterns. In the second part I analyze four scientific manuscripts, which reflect the main results of the thesis in details.

## 2. THEORETICAL BACKGROUND

The purpose for this chapter is to give a brief theoretical introduction to the scientific manuscripts presented in the second part of the thesis. More detailed description of the theory is better explained in the cited literature.

### 2.1 Poroelasticity and thermoelasticity

#### *Governing equations*

The poro-elastic model is an extension of linear elasticity that allows for and takes into account the presence of a diffusing pore fluid; it is relevant to the deformation and fracture of the porous elastic materials with applications to geophysics. The pore fluid is free to diffuse through the material and interact with the solid elastic skeleton. The diffusion process introduces the time dependence into the otherwise quasi-static elasticity equations. The poroelastic equations derived by [Biot \[1941\]](#), subsequently reformulated by [Rice and Cleary \[1976\]](#) are that the stress tensor  $\sigma_{ij}$  is given by

$$\sigma_{ij} = 2\mu\varepsilon_{ij} + 2\mu\varepsilon_{kk} \frac{\nu}{1-2\nu} \delta_{ij} + \alpha p_f \delta_{ij}, \quad (1)$$

where the repeated indices denote summation; the relation between the strain tensor  $\varepsilon_{ij}$  and the displacements  $u_i$  is  $\varepsilon_{ij} = \frac{1}{2} \left( \frac{\partial u_i}{\partial x_j} + \frac{\partial u_j}{\partial x_i} \right)$ ;  $\delta_{ij} = \begin{cases} 1 & \text{for } i = j \\ 0 & \text{for } i \neq j \end{cases}$  is the Kronecker delta (the positive compressive stress as a sign convention is used here).

According to equation (1) the deformation is controlled by the effective stress  $\sigma'_{ij} = \sigma_{ij} + \alpha p_f \delta_{ij}$  [[Garg and Nur, 1973](#)], thus, the rheology relation for the effective stress can be formulated as follows

$$\sigma'_{ij} = \sigma_{ij} - \alpha p_f \delta_{ij} = 2\mu\varepsilon_{ij} + 2\mu\varepsilon_{kk} \frac{\nu}{1-2\nu} \delta_{ij}. \quad (1a)$$

The pore pressure  $p_f$  is related via

$$p_f = Q\zeta + \alpha Q\varepsilon_{kk} \quad (2)$$

to the variation of fluid volume content  $\zeta$ , and the dilation,  $e = \varepsilon_{kk}$ . The constants and their physical interpretation are given in the next subsection. Provided there are no body

forces or fluid sources in the material the governing equations are written as the equilibrium equation for the stresses

$$\sum_j \frac{\partial}{\partial x_j} \sigma_{ij} = 0. \quad (3)$$

The force balance equation formulated for effective stress as follows

$$\sum_j \frac{\partial}{\partial x_j} \sigma'_{ij} = \alpha \frac{\partial}{\partial x_i} p_f. \quad (3a)$$

The term which appears on the right hand side in equation (3a) is commonly referred as *seepage force*. According to equation (3a) the physical meaning for seepage force is equivalent to the *volume force* which is acting along the gradients of the fluid pressure and equal to zero, when the fluid pressure is homogeneous, i.e. when the gradients are zero.

Darcy's law which relates mass flux to the gradient of pore pressure

$$q_i = -\rho_0 \kappa \frac{\partial}{\partial x_i} p_f, \quad (4)$$

and a mass-conservation equation for the pore fluid

$$\frac{\partial}{\partial t} m = -\frac{\partial}{\partial x_i} q_i, \quad (5)$$

where  $m$  is the mass of fluid per unit volume and  $\rho_0$  is the reference density. Using equations (2, 4 and 5) the fluid diffusion equation for the pore pressure with a coupling term for the dilation can be written in the form:

$$\frac{\partial p_f}{\partial t} - \kappa Q \sum_j \frac{\partial^2 p_f}{\partial x_j^2} = \alpha Q \frac{\partial e}{\partial t}. \quad (6)$$

### ***Poroelastic constants and their physical interpretation***

The following symbolism is used in the previous subsection:  $\alpha$  is the Biot-Willis poroelastic constant, that is, the ratio of fluid volume to the volume change of solid allowing the fluid to drain, where  $0 \leq \alpha \leq 1$ ;  $\mu$  is the shear modulus;  $\nu, \nu_u$  are drained and undrained Poisson ratios, where  $0 \leq \nu \leq \nu_u \leq \frac{1}{2}$ ;  $\kappa$  is the permeability coefficient;  $d\zeta / dp_f = 1/Q$  is a measure of the change in the fluid content generated in a unit reference volume during the change of the pressure with the strains kept constant,

where  $Q = \frac{2\mu(v_u - \nu)}{\alpha^2(1-2\nu)(1-2\nu_u)}$  and  $Q \geq 0$ ; and finally,  $\zeta$  is the variation of fluid content per unit reference volume, i.e. mass of fluid per unit volume/initial density  $\rho_0$ .

### ***Similarity and difference between poro- and thermo- elasticity***

The thermoelastic continuative equation is equivalent to the poroelastic continuative equation (1) if the fluid pressure  $p_f$  is changed to the temperature  $T$  ( $p_f \rightarrow T$ ) and the Biot-Willis poroelastic constant is changed as follows  $\alpha \rightarrow \frac{\alpha_T E}{1-2\nu}$ , where  $\alpha_T$  is the thermal expansion coefficient and  $E$  is a Young modulus [Rice and Cleary, 1976; Timoshenko and Goodier, 1982]. The difference between thermo and poro elasticity will appear in equation (6), i.e. the heat conduction equation is governed by equation

$$\frac{\partial T}{\partial t} - \kappa_h \sum_j \frac{\partial^2 p_f}{\partial x_j^2} = 0, \quad (7)$$

here  $\kappa_h$  is the heat conduction coefficient. In equation (7) the change in dilation does not contribute to the change in temperature. The seepage force in poroelastic equation (3a) is equivalent to the thermal stress in thermoelasticity.

### ***Steady-state (quasi-static) poroelasticity***

In case of a steady-state fluid filtration no time dependence is introduced to the fluid diffusion equation (6), which can be simplified to the ordinary Laplace equation as the following:

$$\sum_j \frac{\partial^2 p_f}{\partial x_j^2} = 0. \quad (8)$$

Now, as one can see from (6) and (7) in the case of the steady-state problems the poroelastic and thermoelastic equations are equivalent.

## **2.2 Pore-fluid pressure effect on deformation and failure**

It is generally recognized that the pore-pressure has different effects on deformation and failure of the fluid saturated porous solid [Terzaghi, 1923; Skempton, 1961; Garg and Nur, 1973 Jaeger and Cook, 1979; Paterson and Wong, 2005]. Both the theoretical analysis and experimental observations show that, provided that the

rocks contain a connected system of pores, the failure is controlled by the Terzaghi effective stress  $\sigma''_{ij}$  defined as

$$\sigma''_{ij} = \sigma_{ij} - p_f \delta_{ij}. \quad (9)$$

However, the deformation is controlled by another effective stress law  $\sigma'_{ij}$ , formulated as follows

$$\sigma'_{ij} = \sigma_{ij} - \alpha p_f \delta_{ij}, \quad (10)$$

where  $\sigma_{ij}$  is the total stress tensor;  $p_f$  is the pore fluid pressure,  $\alpha$  is the Biot-Willis coupling poroelastic constant (by convention, compressive stress is positive).

### 2.3 Failure envelope for rock

In nature, the rock failure occurs in two different modes: in the shear bands and in the tensile fractures. The laboratory triaxial experiments show that the Mohr-Coulomb criterion provides an accurate prediction for a shear failure [*Jaeger and Cook, 1979; Paterson and Wong, 2005*]:

$$\tau - \sigma''_m \sin(\phi) = C \cos(\phi), \quad (11)$$

where  $\tau = \sqrt{\frac{(\sigma_{xx} - \sigma_{yy})^2}{4} + \sigma_{xy}^2}$  is the stress deviator,  $\sigma''_m = \frac{\sigma_{xx} + \sigma_{yy}}{2} - p_f$  is the mean Terzaghi effective stress,  $C$  is the rock cohesion and  $\phi$  is the internal friction angle.

On the other hand, Griffith's theory provides a theoretical criterion for tensile failure of a fluid-filled crack [*Murrell, 1964*]:

$$\tau - \sigma''_m = \sigma_T, \quad (12)$$

where  $\sigma_T$  is the tensile strength of the rock. This criterion has also been verified experimentally [*Jaeger, 1963; Paterson and Wong, 2005*].

Both the tensile and shear failure criteria are shown on the Mohr diagram (*Figure 1*), where *lm* is the Mohr-Coulomb envelope (eq. 11) and *kl* is the tensile cut-off limit (eq. 12). Any stress-state in a particular point of the solid can be shown by the Mohr circle on this diagram with radius  $\tau$  and center  $\sigma''_m$  ( $\tau$  and  $\sigma''_m$  are defined after equation (11)).

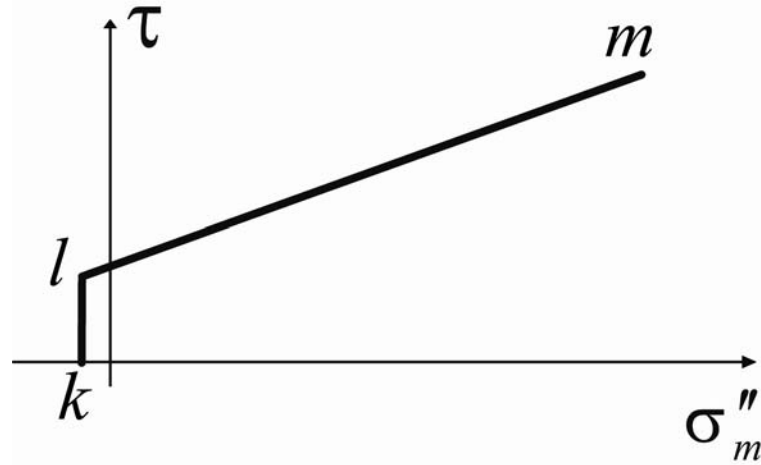


**Figure 1.** Failure envelope for rocks ( $lm$  is the Mohr-Coulomb envelope (eq. 11) and  $kl$  is the tensile cut-off limit (eq. 12)).

All Mohr-circles on the Mohr-diagram located below  $lm$  and on the right side of  $kl$  represent the stable combination of stresses in the elastic domain. However, if the Mohr circle touches the failure envelope  $klm$ , the solid undergoes the irreversible plastic deformation, which leads to the formation of shear bands and tensile fractures. Depending on the location of the circle touching the failure envelope, the formation of the shear bands ( $lm$ ) or the tensile fractures ( $kl$ ) takes place. The shear bands form at the angle of  $\frac{\pi}{4} - \frac{\phi}{2}$  to the direction of maximum compressive (Terzaghi effective) stress; the tensile fractures develop perpendicularly to the direction of the maximum tensile (Terzaghi effective) stress.

## 2.4 Poro-elasto-plasticity

In physics and materials science plasticity is a property of a material to undergo a non-reversible deformation in response to an applied force. For many natural materials, the load applied to the sample will cause the deformation to behave in an elastic manner. Each increment of the load is accompanied by a proportional increment in extension, and when the load is removed, the piece returns exactly to its original size (Figure 2, blue line). However, once the load exceeds some threshold (described by equation (11) for shear loading and by equation (12) for tensile loading) the deformation increases more rapidly than in the elastic region (Figure 2, green curve), and when the load is removed, some amount of the extension remains. The further deformation of the material could lead to the fracture.



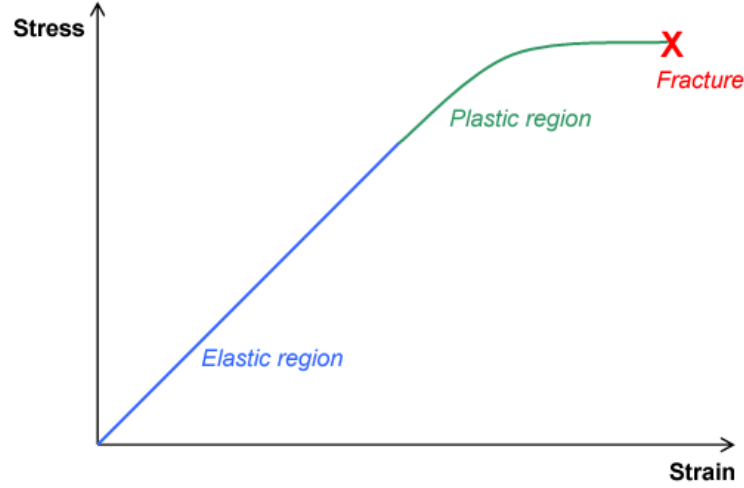


**Figure 2.** A stress-strain diagram. (The blue line shows the reversible elastic deformation domain, while the green curve shows the irreversible plastic deformation in the process zone, which accompanies the formation of the fracture.)

According to the general approach for poro-elasto-plastic deformation [*Rice and Cleary, 1976; Vermeer, 1990*], the full strain rate tensor is given by

$$\dot{\epsilon}_{ij} = \dot{\epsilon}_{ij}^{pe} + \dot{\epsilon}_{ij}^{pl} \quad (13)$$

where the superscripts *pe* and *pl* denote the poro-elastic and the plastic components, respectively. The poro-elastic strain rates can be written as:

$$\dot{\epsilon}_{ij}^{pe} = \frac{\dot{\sigma}_{ij} - \dot{\sigma}_m \delta_{ij}}{2G} + \frac{\dot{\sigma}_m - \alpha \dot{p}^f}{2G} \delta_{ij} \frac{1-2\nu}{1+\nu}. \quad (14)$$

The plastic strain rates are given by

$$\begin{aligned} \dot{\epsilon}_{ij}^{pl} &= 0 \text{ for } f < 0 \text{ or } (f = 0 \text{ and } \dot{f} < 0) \\ \dot{\epsilon}_{ij}^{pl} &= \lambda \frac{\partial q}{\partial \sigma_{ij}''} \text{ for } f = 0 \text{ and } \dot{f} = 0 \end{aligned} \quad (15)$$

The yield function in the form  $f = \max(f_{tension}, f_{shear})$ , where  $f_{tension}$  and  $f_{shear}$  are the yield functions for a failure in tension and in shear, respectively, defined as:

$$\begin{aligned} f_{tension} &= \tau - \sigma_m'' - \sigma_T \\ f_{shear} &= \tau - \sigma_m'' \sin(\phi) - C \cos(\phi) \end{aligned} \quad (16)$$

The parameter  $\lambda$  in (eq. 15) is the non-negative multiplier of the plastic loading [*Vermeer, 1990*], and  $q$  is the plastic flow function, defined as follows for a tensile (the associated flow rule) and shear failure (the non-associated flow rule):

$$\begin{aligned} q_{tension} &= \tau - \sigma_m'' \\ q_{shear} &= \tau - \sigma_m'' \sin(\nu) \end{aligned} \quad (17)$$

where  $\nu$  is the dilation angle ( $\nu < \phi$ ), that disappears after a few percent of strain. Note that in (eq. 14) the total stress is used, whereas the Terzaghi effective stress (eq. 9) applies in the failure equations (15-17).

Equations (13-17) along with (3, 8, 9) represent the full set of equations which governs a quasi-static propagation of the plastic deformations into either shear bands or tensile fractures (The numerical code which solves the system of equations is presented in the Appendix). The term tensile fracture is not used here in its classical sense as a discontinuity in both traction and displacement fields. Rather, it describes the inelastic material response in the process zone area that accompanies fracture onset and propagation [Ingraffea, 1987].

## 2.5. Linear elastic fracture mechanics

Fracture mechanics is the field of solid mechanics that deals with the behavior of the cracked bodies subjected to stresses and strains. The modern fracture mechanics is based on the Griffith's theory [1920], outlined below.

In order to explain why the experimental tensile strength of brittle materials is many times lower than the ultimate stress required for the breaking of the atomic bonds, Griffith [1920] proposed that the failure of materials may be controlled by the presence of small defects, which may propagate as cracks into the solid. This assumption was based on the work of Inglis who showed that the local stress at the tip of an elliptical crack can be concentrated many times higher than the macroscopic stress. Griffith proposed that the propagation requires the creation of the surface energy, which is supplied by the loss of the strain energy accompanying the relaxation of the local stresses as the crack advances. The failure occurs when the loss of the strain energy is sufficient to provide the increase in the surface energy.

The Griffith's theory was not accepted with proper attention for over twenty years both in Engineering and Academics communities. The consequences of the ignorance are devastating (Figure 3a), as for example, in order to estimate the strength of the structural constructions like ships, a simple beam theory (Figure 3b) was considered sufficient. The construction engineers measured the stresses in the various

parts of the hull with strain-gauges, and “proved” that simple beam theory gave results well inside the safety envelope of the materials. [Gordon, 1991].

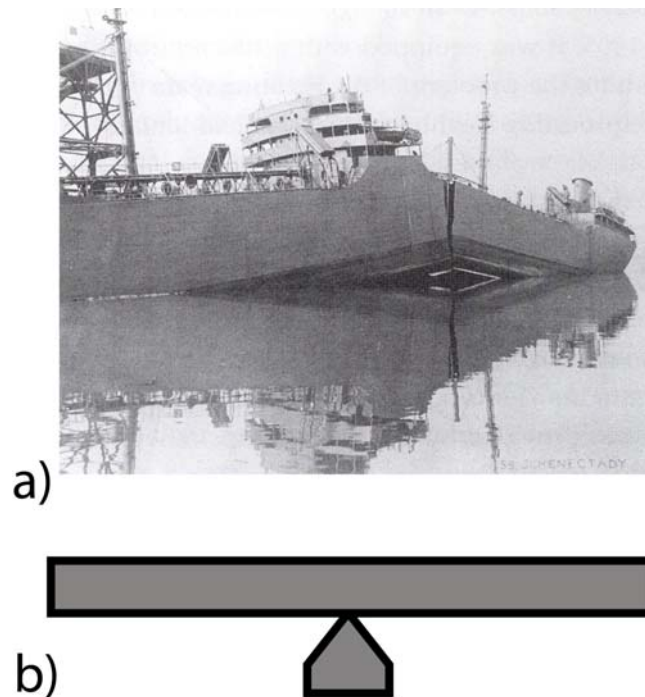


**Figure 3a.** Tanker SS Schenectady, fractured a day after its launch in January 1941.

**Figure 3b.** An elastic beam in the gravitation field was used as a standard method for calculating of ship’s strength.

Later in 1948, the naval research engineer Irwin formulated the Griffith’s theory in terms of stress concentrations rather than in terms of energy. Irwin introduced the *fracture toughness* concept which is universally accepted as the defining property of fracture mechanics. Irwin demonstrated that the Griffith’s theory can also be applied to ductile materials, provided that the size of the plastic zone located at the fracture tip is much smaller than the fracture length. Based on the Griffith’s theory, he represented the concept of a *strain-energy realize rate*, controlling the initiation and propagation of a fracture. Later in 1968 Rice introduced the *J-integral*, a method of calculation of the energy realized during a fracture propagation. This method is applicable for the materials with a generalized constitutive rheology, for example, for poro-elasto-plastic materials.

The Griffith’s energy criterion can be represented equivalently via the path-independent *J-integral* [Rice, 1968; Hellan, 1984]:

$$2\gamma \leq J, \quad (18)$$

here  $2\gamma$  is the specific surface energy, assigned to one side of the fracture surface; and the path-independent  $J$ -integral is defined as:

$$J = \int_{\Gamma} [U dx_2 - \vec{T} \cdot \frac{\partial \vec{u}}{\partial x_1} ds], \quad (19)$$

here  $U$  is the strain energy density function, defined as [Atkinson and Craster, 1991; Wang, 2000]:

$$U = \frac{1}{2} \sigma_{ij} \varepsilon_{ij} + p_f \zeta, \quad (20)$$

where  $\zeta$  is the variation of fluid content per unit reference volume, introduced in equation (2).

In equation (19) the integral is taken along any path  $\Gamma$  (counter-clockwise) around the crack tip;  $\vec{T}$  is the vector of traction on  $\Gamma$ , with components  $T_i = \sigma_{ij} n_j$ ,  $n_j$  is the normal to the curve  $\Gamma$ ;  $s$  is the arc length along  $\Gamma$ . Since a path of integration can be arbitrary chosen in the poroelastic regime, the curve  $\Gamma$  can be taken from the lower side ( $x_1 = a$ ,  $x_2 = 0^-$ ), past ( $x_1 = a + \Delta a$ ,  $x_2 = 0$ ), to the upper side at ( $x_1 = a$ ,  $x_2 = 0^+$ ). Since  $dx_2 = 0$ , equation (19) becomes ([Rice, 1968; Hellan, 1984]):

$$J = \lim_{\Delta a \rightarrow 0} \frac{1}{2\Delta a} \int_a^{a+\Delta a} \sigma_{2i}(x_1, 0, a) [u_i(x_1, 0^+, a + \Delta a) - u_i(x_1, 0^-, a + \Delta a)] dx_1, \quad (21)$$

where  $\sigma_{2i}(x_1, 0, a)$  is the stress on the crack tip of the length  $2a$ ;  $u_i(x_1, 0^\pm, a + \Delta a)$  are the displacements on the crack tip of the length  $2(a + \Delta a)$  [Hellan, 1984].

### 3. SUMMARY OF THE PAPERS

A brief summary of the papers is presented in the following order. The results of the papers I and II are based on the new analytical solution derived for a closed crack, while in the papers III and IV, I derived the analytical solution for an open crack. Yuri Podladchikov introduced me to the numerical modeling which made me possible to develop my own numerical codes in order to study the failure patterns in the paper I. Both Yuri Podladchikov and Francois Renard helped me to formulate the problem for the first manuscript and improve the text. Yuri Podladchikov also helped me to formulate the problem for the third paper. Papers II and IV have a single author.

#### **Resume of Paper I**

In the first paper we have studied various failure patterns, driven by a localized fluid source at the depth. The reasons why the fluid pressure can be laterally localized at the depth in the earth's crust are reviewed in [[Hickman et al, 1995](#)]. There have been developed two numerical codes using a finite difference and finite element methods which allowed to model failure patterns caused by the tensile and/or shear failures in a porous elastoplastic medium [[Biot, 1941](#); [Rice and Cleary, 1976](#); [Vermeer and de Borst, 1984](#); [Wang, 2000](#)]. It is demonstrated that at least five failure patterns (tensile or shear) can occur. Moreover, we calculate analytically the critical pressure at which a failure nucleates and we propose a phase-diagram of the failure patterns, illustrating the dependence on the model parameters. The results of the paper have a direct application to the geological problems, because many natural systems, such as magmatic dykes, mud volcanoes, hydrothermal vents, or fluid in faults, show the evidence that the pore pressure increase is localized instead of being homogeneously distributed. This paper contains animations in the Auxiliary Materials section, which illustrate the evolution of failure patterns during the increase of the pore-fluid pressure at the localized source.

#### **Resume of Paper II**

In the second paper we discuss the effects of the coupling between the deformation and pore-fluid diffusion on faulting and failure processes. We consider an arbitrarily oriented preexisting fault zone of finite length, located at the depth with a

given fluid overpressure in it and surrounded by the porous and permeable rocks. The intrinsic elastic and transport properties of these rocks are assumed to be isotropic and homogeneous. The seepage forces caused by the steady-state fluid diffusion from the fault zone to the surrounding permeable rocks are calculated analytically using the complex-potentials method for the pore-elasticity and conformal mapping. The pore-fluid overpressure required for the fault reactivation is calculated analytically in 2D, assuming that the tectonic stress state, the rock intrinsic properties and the geometry of the pre-existing fault are known. The solution is applied to the micro-earthquake triggering caused by the hydrocarbon withdrawals from a reservoir. Other applications such as the storage of carbon dioxide in porous rocks and geothermic exploitation are also considered.

### Resume of Paper III

In the third paper we calculate explicitly a seepage forces caused by the coupling of pore-pressure gradients to the rock deformation. We apply the obtained analytical solution [[Auxiliary materials for paper 3](#)] to the Griffith's theory of failure and demonstrate that the failure is controlled by a *new effective stress law*:

$$\sigma_{\infty} + Wp_{\infty} + (1-W)p_c \geq T_0 = \sqrt{\frac{4\gamma\mu}{\pi a(1-\nu)}},$$

$$\text{with } W = \frac{\alpha}{2} \frac{1-2\nu}{1-\nu} \left(1 - \frac{1}{\ln \frac{2c}{a}}\right) \quad (22)$$

where  $\sigma_{\infty}$  is the macroscopic far-field stress and  $T_0$  is the theoretical tensile strength of the material, which depends on the length of preexisting crack  $a$ ; the specific surface energy  $\gamma$  required for the creation of a new fractured surface; the shear modulus  $\mu$ ; and the Poisson ratio  $\nu$ ;  $\alpha$  is the Biot-Willis poroelastic constant [[Paterson and Wong, 2005](#)];  $c$  is the size of a body containing a crack;  $p_{\infty}$  is the far-field pore-fluid pressure and  $p_c$  is the crack fluid pressure.

According to equation (22), during the uniform rise of the pore fluid pressure inside the porous medium the onset of fracture growth is controlled by the remote Terzaghi's effective stress,

$$\sigma' = \sigma_{\infty} + p_{\infty}, \quad (23)$$

since the fracture pressure  $p_c$  at the onset of the fracture growth is equal to the pore pressure  $p_\infty$  in the surrounding fluid-saturated rock. The tensile strength decreases as the fracture grows in length. Therefore, the fracture is accelerated by an increase in a tensile excess load (and by the release of elastic strain energy), if the remote stress and the pore pressure are kept constant. In reality, however, the fracture pressure  $p_c$  in a propagating double-ended fracture does drop because the volume of the growing fracture increases. This causes an inflow of the pore-fluid from the surrounding rock at a rate depending on the hydraulic conductivity of the rock. At the same time, the decrease in fracture pressure will entail a decrease in the driving stress, which will retard, possibly stabilize, or even temporary stop the propagation of a tensile fracture inside the fluid saturated rock. Since the rocks in the earth's crust are mostly under a compressive stress state at the depth ( $\sigma_\infty < 0$ ), the presence of fluid in the pores  $p_\infty > 0$  could promote the propagation of fracture during an earthquake, which takes place when

$$\sigma'' = \sigma_\infty + Wp_\infty \geq 0. \quad (24)$$

Thus, the main result of this paper is the following: we demonstrate that the initiation of a tensile fracture is controlled by the Terzaghi's effective stress, while the propagation of a tensile fracture is controlled by the effective stress:

$$\sigma'' = \sigma_\infty + \frac{\alpha}{2} \frac{1-2\nu}{1-\nu} p_\infty. \quad (25)$$

### **Resume of Paper IV**

In the forth paper we propose a hydraulic fracturing criterion for an elliptical cavity in a permeable poroelastic medium under a non-hydrostatic far-field stress state. The elliptical cavity is filled with a constant fluid pressure  $p_c$  inside the cavity. The far-field pore fluid pressure  $p_\infty$  is different from the fluid pressure in the cavity ( $p_c \neq p_\infty$ ), therefore the fluid can infiltrate from the cavity into surrounding permeable rock. The diffusive fluid couples to the rock deformation, creating an additional stress field via seepage forces which has an additional effect on the initiation of a fracture. We considered the steady-state fluid flux from the cavity into a surrounding permeable reservoir with the homogeneous and isotropic intrinsic properties. We considered two applications of the analytical solution: the hydraulic fracturing of boreholes with an

elliptical cross-section and the *in situ* stress measurements in a highly permeable formation. We demonstrate that the small deviations of the borehole's cross-section from the circular have an additional effect on the *breakout pressure* and show that the *fluid leakage* has a strong influence on the fracture *closure pressure*. It is shown that if a reservoir is highly permeable then a fracture closure pressure is equal to

$$p_c = -\frac{\sigma_h + \eta p_\infty}{1 - \eta}, \quad (26)$$

where  $\sigma_h$  is the minimum *in situ* stress,  $p_\infty$  is the far-field pore pressure;  $\eta = \frac{\alpha}{2} \frac{1 - 2\nu}{1 - \nu}$

here  $\alpha$  is the Biot-Willis poroelastic constant and  $\nu$  is the Poisson ratio. This formula shows that the poroelastic coupling must be taken into account in the highly permeable reservoirs, since nowadays it is assumed in industry that  $p_c = -\sigma_h$ .



## BIBLIOGRAPHY

- Atkinson, C., Craster R.V. 1991. Plane strain fracture in Poroelastic Media. Proceedings: Mathematical and Physical Sciences, 434(1892), 605-633.
- Biot, M. A. 1941. General theory of three-dimensional consolidation. *Journal of Applied Physics* 12, 155-164.
- Cobbold, P.R., Rodrigues, N. 2007. Seepage forces, important factors in the formation of horizontal hydraulic fractures and bedding-parallel fibrous veins ('beef' and icone-in-cone). *Geofluids* 7 (3): 313-322.
- Garg, S. K., and Nur, A. 1973. Effective stress laws for fluid-saturated porous rocks. *Journal of Geophysical Research*, 78(26), 5911-5921.
- Gordon, J.E. 2006. *The New Science of Strong Materials or Why You Don't Fall through the Floor*. Princeton University Press. pp. 328.
- Griffith, A. A. 1920. The Phenomena of Rupture and Flow in Solids, *Phil. Trans. Roy. Soc., London*, A, 221, 163-198.
- Hellan, K. 1984. *Introduction to fracture mechanics*. McGraw-Hill, Inc., New York. 302 pp.
- Hickman, S., Sibson, R., Bruhn, R. 1995. Introduction to special section: Mechanical involvement of fluids in faulting. *Journal of Geophysical Research*, 100(B7), 12831-12840.
- Ingrafea, A. R. 1987. Theory of crack initiation and propagation in rock, in *Fracture Mechanics of Rock*, edited by B. K. Atkinson, pp. 71-110, Academic Press, London.
- Irwin, G. R. 1948 *Fracture of metals* (ed.F. Jonassen, W. B. Roop & R. T. Bayless),pp. 147-166. Cleveland, OH: ASM.
- Miller S. A., Collettini, C., Chiaraluce, L., Cocco, M., Barchi, M. and Kaus, B. 2004. Aftershocks driven by a high pressure CO<sub>2</sub> source at depth. *Nature*, 427, 724-727.
- Mourgues R., and Cobbold, P.R. 2003. Some tectonic consequences of fluid overpressures and seepage forces as demonstrated by sandbox modeling, *Tectonophysics*, 376, 75-97.
- Murrell, S. A. F. 1964. The theory of propagation of elliptical Griffith cracks under various conditions of plane strain or plain stress. Parts 2, 3; *British Journal of Applied Physics*, 15, 1211-23.

- Muskhelishvili, N.I. 1977. Some Basic Problems in the Mathematical Theory of Elasticity. Springer, Berlin. 768 pp.
- Paterson, M. S., and Wong, T.-F. 2005. *Experimental Rock Deformation-The Brittle Field*, 346 pp., Springer, Berlin.
- Rice, J. 1968. Mathematical analysis in the mechanics of fracture. In Liebowitz, H., editor, *Fracture - An advanced treatise*, volume 2, pages 191–311. Pergamon Press, Oxford.
- Rice, J. R., and Cleary, M. P. 1976. Some basic stress-diffusion solutions for fluid-saturated elastic porous media with compressible constituents. *Reviews of Geophysics and Space Physics*, 14, 227-241.
- Terzaghi, K. 1943. *Theoretical Soil Mechanics*, John Wiley and Sons, 528 pp., New York.
- Timoshenko, S. P., Goodier, J.N. 1982. *Theory of Elasticity*. McGraw-Hill, New York. 608 pp.
- Vermeer, P.A., de Borst, R. 1984. Non-associated plasticity for soils, concrete and rock. *Heron*, 29(3), 3-62.
- Wang, H.F. 2000. *Theory of Linear Poroelasticity with Applications to Geomechanics and Hydrology*. Princeton University Press, Princeton and Oxford. 276 pp.

## APPENDIX: THE NUMERICAL MODELING OF THE FLUID FLOW IN A POROUS ELASTOPLASTIC MEDIUM (MatLab code)

In this appendix I will present an explicit finite difference MatLab code based on the Fast Lagrange Analysis of Continua, which I have developed during my PhD in order to model various failure patterns caused by the localized pore-pressure increase. The results of the modeling are presented in the first scientific manuscript. The animations that show the evolution of failure patterns during the localized increase of a fluid overpressure is presented in the Auxiliary materials for first paper.

The code consists of the main (calling) program: **Main.m** and five subroutines: **Pressure\_Initialization.m**, **Pcrit.m**, **YieldFunction\_array.m**, **YieldFunction\_new.m** and **Plasticity.m** .

In order to run the code, all files must be located in the same folder. One should run **Main.m** program in MatLab.

### Main.m

```
clear;
%physics
H      = [4,1];      % Box size L and h
dH     = H(2)/10;   % Fluid source size w
ro_i   = 1e8;       % 'computational' density
phi    = 35*pi/180; % friction angle
psi    = 0*pi/180;  % dilation angle
tan_phi = tan(phi);
sin_phi = sin(phi);
cos_phi = cos(phi);
sin_psi = sin(psi);
A       = 0.2;      % Sh=A*Sv
Earr    = 2.6667e7; % Young modulus
nu      = 0.3;      %Poison ratio
K       = Earr/3/(1 - 2*nu); % Bulk modulus
G       = Earr/2/(1 + nu); % Shear modulus
kf      = 0.4*1.05e6;
Vp      = sqrt(max(9*K*G/(3*K+G))/ro_i); % Wave velos
Cohesion = 0.1; % Cohesion
St      = Cohesion/8; % Tensile strength
%numerics
nx      = [151,51]; % Resolution
dx      = H./(nx-1); %
dt      = 1/4*min(dx)/Vp/2; % Time step
damp    = 1e-1; % 'Elastic' damper
time_out = 40;
% initialization
x       = [0:dx(1):H(1)]';
y       = [0:dx(2):H(2)]';
x2D    = repmat(x,[1,nx(2)]);
```

```

y2D      = repmat(y,[nx(1),1]);
xc       = [dx(1)/2:dx(1):H(1)-dx(1)/2]';
yc       = [dx(2)/2:dx(2):H(2)-dx(2)/2];
x2Dc     = repmat(xc,[1,nx(2)-1]);
y2Dc     = repmat(yc,[nx(1)-1,1]);
Pre_flu  = zeros(nx(1),nx(2)); % Fluid pressure
Pressure_Initialization; % Steady-state fluid pressure calculation
[Pc,Mode] =Pcrit(A,phi,Cohesion,St,H(2)/dH,nu); % Pc 'estimation'
Stress_check = zeros(3,nx(1)-1,nx(2)-1);
% F_plot    = zeros(nx(1)-1,nx(2)-1);
Size_S    = (nx(1)-1)*(nx(2)-1);
F         = -100*ones(nx(1)-1,nx(2)-1);
dStrain   = zeros(3,nx(1)-1,nx(2)-1);
% Terzaghi effective stress
Txy_eff   = zeros(nx(1)-1,nx(2)-1);
Syy_eff   = -(H(2)- y2Dc(:, :))*1/H(2);
Sxx_eff   = -A*(H(2)- y2Dc(:, :))*1/H(2);
% Total stress
Txy_tot   = zeros(nx(1)+1,nx(2)+1);
Syy_tot   = zeros(nx(1)+1,nx(2)+1);
Sxx_tot   = zeros(nx(1)+1,nx(2)+1);

Vx        = zeros(nx(1),nx(2));%Solid velocity
Vy        = zeros(nx(1),nx(2));
Ux        = Vx;
Uy        = Vy;
time = 0;

Pre_flu_cen0 = (Pre_flu(1:end-1,1:end-1) + Pre_flu(2:end,1:end-1)...
+ Pre_flu(1:end-1,2:end) + Pre_flu(2:end,2:end))/4;
F_old      = -100;
while time < time_out
    time = time + dt;
    if time <= time_out% increase of pore pressure
        Pcoef = 0.9*Pc+8*Pc*time/time_out;
    end
    % Total stresses
    Pre_flu_cen = Pcoef*Pre_flu_cen0; % increase of pore
pressure
    Sxx_tot(2:end-1,2:end-1) = (Sxx_eff - Pre_flu_cen);
    Syy_tot(2:end-1,2:end-1) = (Syy_eff - Pre_flu_cen);
    Txy_tot(2:end-1,2:end-1) = (Txy_eff);
    % Boundary conditions for total stress
    Syy_tot(:,end) = (1- y2Dc(1,end)/H(2)); % Top
    Txy_tot(:,end) = 0; % Top
    Sxx_tot(:,end) = A*(1- y2Dc(1,end)/H(2));% Top

    Syy_tot(:,1) = Syy_tot(:,2); % Bottom
    Txy_tot(:,1) = -Txy_tot(:,2); % Bottom
    Sxx_tot(:,1) = Sxx_tot(:,2); % Bottom

    Syy_tot(1,:) = Syy_tot(2,:); % Right
    Txy_tot(1,:) = -Txy_tot(2,:); % Right
    Sxx_tot(1,:) = Sxx_tot(2,:); % Right

    Syy_tot(end,:) = Syy_tot(end-1,:); % Left
    Txy_tot(end,:) = -Txy_tot(end-1,:); % Left
    Sxx_tot(end,:) = Sxx_tot(end-1,:); % Left
    % VELOCITY UPDATE
    D_Sxx_x = (diff(Sxx_tot(:,1:end-1),1,1) +...

```

```

    diff(Sxx_tot(:,2:end),1,1))/dx(1)/2;
D_Txy_x = (diff(Txy_tot(:,1:end-1),1,1) + ...
    diff(Txy_tot(:,2:end),1,1))/dx(1)/2;
D_Txy_y = (diff(Txy_tot(1:end-1,:),1,2) + ...
    diff(Txy_tot(2:end,:),1,2))/dx(2)/2;
D_Syy_y = (diff(Syy_tot(1:end-1,:),1,2) + ...
    diff(Syy_tot(2:end,:),1,2))/dx(2)/2;

Vx      = Vx*(1-damp) + dt*(D_Sxx_x+D_Txy_y)/ro_i;
Vy      = Vy*(1-damp) + dt*(D_Txy_x+D_Syy_y-1)/ro_i;
% The Boundary Conditions for VELOCITY
Vx( 1,:) = 0;           %left x
Vx(end,:) = 0;         % right x
Vy(:,1)  = 0;         % Down Y
% Strains
dVx_dx   = (diff(Vx(:,1:end-1),1,1) + ...
    diff(Vx(:,2:end),1,1))/dx(1)/2;
dVy_dx   = (diff(Vy(:,1:end-1),1,1) + ...
    diff(Vy(:,2:end),1,1))/dx(1)/2;
dVx_dy   = (diff(Vx(1:end-1,:),1,2) + ...
    diff(Vx(2:end,:),1,2))/dx(2)/2;
dVy_dy   = (diff(Vy(1:end-1,:),1,2) + ...
    diff(Vy(2:end,:),1,2))/dx(2)/2;

dStrain(:) = [dVx_dx(:) dVy_dy(:) dVy_dx(:)+dVx_dy(:)]';
% Penalty stress
Stress_check(1,(:,,:)) = Sxx_eff + dt * Earr/(1-2*nu)/(1+nu)* ...
    ((1-nu)*dVx_dx + nu.*dVy_dy);
Stress_check(2,(:,,:)) = Syy_eff + dt * Earr/(1-2*nu)/(1+nu)* ...
    ((1-nu)*dVy_dy + nu.*dVx_dx);
Stress_check(3,(:,,:)) = Txy_eff + dt * Earr/(1-2*nu)/(1+nu)* ...
    (1/2-nu)* (dVx_dy + dVy_dx);

% Plastic failure search
[F(:)]=YieldFunction_array(Size_S,Stress_check,phi,Cohesion,St);
ij = find(F<0);
% Elastic update
Sxx_eff(ij) = Stress_check(1,ij);
Syy_eff(ij) = Stress_check(2,ij);
Txy_eff(ij) = Stress_check(3,ij);
%
if max(F(:))>=0
    damp=0;
end
% Plastic update
Plasticity;
% Displacement
Ux = Ux + dt*Vx;
Uy=  Uy + dt*Vy;
% Graphyics
if mod(round(time/dt),400)==400-1
    damp
    %Calculation of the strain deviator
    ex= diff(Ux,1,1);
    Ex = (ex(:,2:end)+ex(:,1:end-1))/2;
    ey= diff(Uy,1,2);
    Ey = (ey(2:end,:)+ey(1:end-1,:))/2;
    g1 = diff(Uy,1,1); G1 = (g1(:,2:end)+g1(:,1:end-1))/2;
    g2 = diff(Ux,1,2); G2 = (g2(2:end,:)+g2(1:end-1,:))/2;
    g = (G1+G2)/2;
    SI= sqrt((Ex-Ey).^2/4+g.^2); % Strain deviator

```

```

        subplot(211), contour(x2Dc,y2Dc,SI,7), axis equal,
        axis tight, axis off, shading interp, colorbar
        subplot(212), pcolor(x2Dc,y2Dc,Syy_eff), axis equal,
        axis tight, axis off, shading interp, colorbar
        time
        drawnow
    end
end
% END OF Main.m

```

### Pressure\_Initialization.m

```

% fluid pressure initialization
nn      = prod(nx);
BM      = sparse(nn,nn);
nbcup   = zeros(nn,1);
nbclr   = zeros(nn,1);
nbcD    = zeros(nn,1);
ij2g    = reshape(1:nn,nx);
NNN=reshape(ij2g(2:end-1,2:end-1),1,[])*(1+nn)-nn;

BM(NNN)      = 1/dt + 2*kf/dx(1)^2+2*kf/dx(2)^2;
BM(NNN+nn)   = -kf/dx(1)^2;
BM(NNN-nn)   = -kf/dx(1)^2;
BM(NNN+nn*nx(1)) = -kf/dx(2)^2;
BM(NNN-nn*nx(1)) = -kf/dx(2)^2;
for i = 1:nx(1)
    neqn = ij2g(i,nx(2));
    BM(neqn,neqn) = 1;nbcup(neqn) = 1;
end
for j=1:nx(2)
    neqn = ij2g(1,j); BM(neqn,:) = 0; BM(neqn,neqn) = 1;
    nbclr(neqn) = 1;
    BM(neqn,ij2g(2,j)) = -1;
    neqn = ij2g(nx(1),j); BM(neqn,:) = 0; BM(neqn,neqn) = 1;
    nbclr(neqn) = 1;
    BM(neqn,ij2g(nx(1)-1,j)) = -1;
end
for i=1:nx(1)
    if (x(i)>=(H(1)-dH)/2)&(x(i)<=(H(1)+dH)/2)
        neqn = ij2g(i,1);
        BM(neqn,:) = 0;
        BM(neqn,neqn) = 1; nbcD(neqn) = 1;
    else
        neqn = ij2g(i,1); BM(neqn,:) = 0; BM(neqn,neqn)
= 1; nbcD(neqn) = 2;
        BM(neqn,ij2g(i,2)) = -1;
    end
end
Rhs      = zeros(nn,1);
Rhs(nbcD==1) = 1;
Rhs(nbcD==2) = 0;
Rhs(nbcup==0&nbcD==0&nbclr==0) =
Pre_flu(nbcup==0&nbcD==0&nbclr==0)/dt;
Pre_flu(:) = sparse(BM)\Rhs;
clear BM, clear Rhs, clear NNN
% END OF Pressure_Initialization

```

### Pcrit.m

```

function [Pc,Mode]=Pcrit(A,phi,C,St,rhos,nu)
eta = (1-2*nu)/(1-nu)/2;
d1 = 1-eta+eta/log(2*rhos)/2;
d2 = eta/log(2*rhos)/2;
Sv = -1;
Delta = -(1-A);
po = [C*cos(phi)/(d1*sin(phi)+d2) C*cos(phi)/(d1*sin(phi)-d2)
St/(d1+d2) St/(d1-d2) St*log(2*rhos)/eta];
av = [ -sin(phi)/(d1*sin(phi)+d2) -sin(phi)/(d1*sin(phi)-d2)
-1/(d1+d2) -1/(d1-d2) 0];
ad = [(-1+sin(phi))/(d1*sin(phi)+d2)/2 (1+sin(phi))/(d1*sin(phi)-
d2)/2 0 1/(d1-d2) 0];
Pcarr = (po+av*Sv+ad*Delta)
Pc = min(Pcarr(Pcarr>0)); % Failure mode
Mode = find(Pcarr==Pc); % Failure pattern
% END OF Pcrit.m

```

### YieldFunction\_array.m

```

function [Ft]=YieldFunction_array(Size_S,Stress,phi,cohesion,St)
% This function search for elastic/plastic elements
Ft = -1000*ones(1,Size_S);
Ft1 = -1000*ones(1,Size_S);
Ft2 = -1000*ones(1,Size_S);
Mean_Stress = zeros(1,Size_S);
Mean_Stress(1,:) = (Stress(1,:)+Stress(2,:))/2; %Mean stress
TTau = zeros(1,Size_S); % Stress deviator
TTau(1,:) = (1/4*(Stress(1,:)-Stress(2,:)).^2+Stress(3,:).^2);
Ft1 = TTau - (Mean_Stress*sin(phi)-cohesion*cos(phi)).^2;
Ft2 = TTau - (Mean_Stress - St).^2;
Ft = max(Ft1,Ft2);
% END OF YieldFunction_array.m

```

### YieldFunction\_new.m

```

function [F,dFds,dQds]=...
YieldFunction_new(Size_ij,Stress,phi,psi,cohesion,St)
F = -10*ones(1,Size_ij);
F1 = -10*ones(1,Size_ij);
F2 = -10*ones(1,Size_ij);
Mean_Stress = zeros(1,Size_ij);
Mean_Stress(1,:) = (Stress(1,:)+Stress(2,:))/2;
tau = zeros(1,Size_ij); % Stress deviator
tau(1,:) = (1/4*(Stress(1,:)-
Stress(2,:)).^2+Stress(3,:).^2).^(1/2);
% Partial derivative of yield function
dFds = zeros(3,Size_ij);
% Partial derivative of flow function
dQds = zeros(3,Size_ij);
% Yield function for tensile failure
F1 = tau + Mean_Stress-St;
% Yield function for shear failure
F2 = tau + Mean_Stress*sin(phi)-cohesion*cos(phi);
Mode2 = find(F2 > F1); % shear
Mode1 = find(F2 <= F1); % open

if size(Mode2,1)*size(Mode2,2)>0
F(1,Mode2) = tau(1,Mode2) + ...

```

```

    Mean_Stress(1,Mode2)*sin(phi)-cohesion*cos(phi);
A2=    1/2*(Stress(1,Mode2)-Stress(2,Mode2))./(2*tau(1,Mode2));
B2 = Stress(3,Mode2)./tau(1,Mode2);

dFds(1,Mode2)    = A2+1/2*sin(phi);
dFds(2,Mode2)    = -A2+1/2*sin(phi);
dFds(3,Mode2)    = B2;

dQds(1,Mode2)    = A2+1/2*sin(psi);
dQds(2,Mode2)    = -A2+1/2*sin(psi);
dQds(3,Mode2)    = B2;
end
if size(Model1,1)*size(Model1,2)>0

F(1,Model1)      = tau(1,Model1) + Mean_Stress(1,Model1) - St;
A3 = 1/2*(Stress(1,Model1)-Stress(2,Model1))./(2*tau(1,Model1));
B3 = Stress(3,Model1)./tau(1,Model1);
dFds(1,Model1)   = A3+1/2*sin(pi/2);
dFds(2,Model1)   = -A3+1/2*sin(pi/2);
dFds(3,Model1)   = B3;

angle             = pi/2;
dQds(1,Model1)   = A3+1/2*sin(angle);
dQds(2,Model1)   = -A3+1/2*sin(angle);
dQds(3,Model1)   = B3;
end
% END OF YieldFunction_new.m

```

### Plasticity.m

```

ij          = find(F>=0);
Size_ij     = length(ij);
if (Size_ij>0)

    if size(ij,1)~=Size_ij
        error('size error')
    end
    Stress=zeros(3,Size_ij);
    Stress(1,:)=Sxx_eff(ij);
    Stress(2,:)=Syy_eff(ij);
    Stress(3,:)=Txy_eff(ij);

    Strain          = dStrain(:,ij);
    %Rheology matrix (Mat of coeff before str rate)
    D              = zeros(3,3,Size_ij);
    FF             = zeros(3,Size_ij);
    [F_old ,dFds,dQds] = YieldFunction_new(Size_ij,...
        Stress,phi,psi,Cohesion,St);
    % Elastoplastic Rheology

D(1,1,:)        = G * ( 4 * dFds(3,:) .* G .* dQds(3,:) + 12 .* ...
    dFds(2,:) .* K .* dQds(2,:) + 4 .* dFds(2,:) .* G .* ...
    dQds(2,:) + 3 .* K .* dFds(3,:) .* dQds(3,:)) ./...
    (3 .* dFds(3,:) .* G .* dQds(3,:) + 4 .* dFds(1,:) ...
    .* G .* dQds(1,:) - 2 .* dFds(1,:) .* G .* dQds(2,:))...
+ 3 .* dFds(1,:) .* K .* dQds(1,:) +...
3 .* dFds(1,:) .* K .* dQds(2,:) + ...
3 .* dFds(2,:) .* K .* dQds(1,:) +...

```



```

3 .* dFds(2,:) .* K .* dQds(2,)- ...
2 .* dFds(2,:) .* G .* dQds(1,:) +...
4 .* dFds(2,:) .* G .* dQds(2,));

D(2,1,:) = - G * (-3 * K * dFds(3,:) .* dQds(3,) + ...
12 .* dFds(2,:) .* K .* dQds(1,) + 4 .* dFds(2,)...
.* G .* dQds(1,) + 2 .* dFds(3,) .* G .* dQds(3,)) ./...
(4 .* dFds(1,) .* G .* dQds(1,) - 2 .* dFds(1,) .* ...
G .* dQds(2,) + 3 .* dFds(1,) .* K .* dQds(1,) + ...
3 .* dFds(1,) .* K .* dQds(2,) - 2 .* dFds(2,) .* ...
G .* dQds(1,) + 4 .* dFds(2,) .* G .* dQds(2,) + ...
3 .* dFds(2,) .* K .* dQds(1,) + 3 .* dFds(2,) .* ...
K .* dQds(2,) + 3 .* dFds(3,) .* G .* dQds(3,));

D(3,1,:) = -dFds(3,:) .* G .* (4 .* G .* dQds(1,) - ...
2 .* G .* dQds(2,) + 3 .* K .* dQds(1,) + 3 .* ...
K .* dQds(2,)) ./ (4 .* dFds(1,) .* G .* dQds(1,))...
- 2 .* dFds(1,) .* G .* dQds(2,) + 3 .* dFds(1,) .* ...
K .* dQds(1,) + 3 .* dFds(1,) .* K .* dQds(2,) - ...
2 .* dFds(2,) .* G .* dQds(1,) + 4 .* dFds(2,) .* ...
G .* dQds(2,) + 3 .* dFds(2,) .* K .* dQds(1,) + ...
3 .* dFds(2,) .* K .* dQds(2,) + ...
3 .* dFds(3,) .* G .* dQds(3,));

D(1,2,:) = - G .* (4 .* dFds(1,) .* G .* dQds(2,) + ...
12 .* dFds(1,) .* K .* dQds(2,) + 2 .* dFds(3,) .* ...
G .* dQds(3,) - 3 .* K .* dFds(3,) .* dQds(3,)) ./ ...
(4 .* dFds(1,) .* G .* dQds(1,) - 2 .* dFds(1,) .* ...
G .* dQds(2,) + 3 .* dFds(1,) .* K .* dQds(1,) + ...
3 .* dFds(1,) .* K .* dQds(2,) - 2 .* dFds(2,) .* ...
G .* dQds(1,) + 4 .* dFds(2,) .* G .* dQds(2,) + ...
3 .* dFds(2,) .* K .* dQds(1,) + 3 .* dFds(2,) .* ...
K .* dQds(2,) + 3 .* dFds(3,) .* G .* dQds(3,));

D(2,2,:) = G .* (3 .* K .* dFds(3,) .* dQds(3,) + ...
4 .* dFds(1,) .* G .* dQds(1,) + 12 .* dFds(1,)...
K .* dQds(1,) + 4 .* dFds(3,) .* G .* dQds(3,)) ./ ...
(4 .* dFds(1,) .* G .* dQds(1,) - 2 .* dFds(1,) .* ...
G .* dQds(2,) + 3 .* dFds(1,) .* K .* dQds(1,) + ...
3 .* dFds(1,) .* K .* dQds(2,)) - 2 .* dFds(2,)...
dQds(1,) + 4 .* dFds(2,) .* G .* dQds(2,) + ...
3 .* dFds(2,) .* K .* dQds(1,) + 3 .* dFds(2,)...
K .* dQds(2,) + 3 .* dFds(3,) .* G .* dQds(3,));

D(3,2,:) = -dFds(3,) .* G .* (3 .* K .* dQds(2,) - ...
2 .* G .* dQds(1,) + 4 .* G .* dQds(2,) + 3 .* ...
K .* dQds(1,)) ./ (4 .* dFds(1,) .* G .* dQds(1,)) ...
- 2 .* dFds(1,) .* G .* dQds(2,) + 3 .* dFds(1,)...
.* K .* dQds(1,) + 3 .* dFds(1,) .* K .* dQds(2,)...
- 2 .* dFds(2,) .* G .* dQds(1,) + 4 .* dFds(2,)...
.* G .* dQds(2,) + 3 .* dFds(2,) .* K .* dQds(1,) + ...
3 .* dFds(2,) .* K .* dQds(2,) + ...
3 .* dFds(3,) .* G .* dQds(3,));

D(1,3,:) = -dQds(3,) .* G .* (4 .* dFds(1,) .* G...
- 2 .* dFds(2,) .* G + 3 .* dFds(2,) .* K + ...
3 .* dFds(1,) .* K) ./ (4 .* dFds(1,) .* ...
G .* dQds(1,) - 2 .* dFds(1,) .* G .* dQds(2,))...
+ 3 .* dFds(1,) .* K .* dQds(1,) + 3 .* dFds(1,)...
.* K .* dQds(2,) - 2 .* dFds(2,) .* G .* dQds(1,) + ...

```

```

4 .* dFds(2,:) .* G .* dQds(2,:) + 3 .* dFds(2,:) .*...
K .* dQds(1,:) + 3 .* dFds(2,:) .* K .* dQds(2,:)...
+ 3 .* dFds(3,:) .* G .* dQds(3,:));

D(2,3,:) = -dQds(3,:) .* G .* (-2 .* dFds(1,:) .* G ...
+ 4 .* dFds(2,:) .* G + 3 .* dFds(2,:) .* K + 3 .*...
dFds(1,:) .* K) ./ (4 .* dFds(1,:) .* G .* dQds(1,:)...
- 2 .* dFds(1,:) .* G .* dQds(2,:) + 3 .* dFds(1,:)...
.* K .* dQds(1,:) + 3 .* dFds(1,:) .* K .* dQds(2,:)...
- 2 .* dFds(2,:) .* G .* dQds(1,:) + 4 .* dFds(2,:) .*...
G .* dQds(2,:) + 3 .* dFds(2,:) .* K .* dQds(1,:) +...
3 .* dFds(2,:) .* K .* dQds(2,:))...
+ 3 .* dFds(3,:) .* G .* dQds(3,:));

D(3,3,:) = G .* (4 .* dFds(1,:) .* G .* dQds(1,:))...
- 2 .* dFds(1,:) .* G .* dQds(2,:) - 2 .* dFds(2,:)...
.* G .* dQds(1,:) + 4 .* dFds(2,:) .* G .* dQds(2,:) +...
3 .* dFds(1,:) .* K .* dQds(1,:) + 3 .* dFds(1,:)...
.* K .* dQds(2,:) + 3 .* dFds(2,:) .* K .* dQds(1,:)...
+ 3 .* dFds(2,:) .* K .* dQds(2,:)) ./ (4 .* dFds(1,:)...
.* G .* dQds(1,:) - 2 .* dFds(1,:) .* G .* dQds(2,:) +...
3 .* dFds(1,:) .* K .* dQds(1,:) + 3 .* dFds(1,:) ...
.* K .* dQds(2,:) - 2 .* dFds(2,:) .* G .* dQds(1,:)...
+ 4 .* dFds(2,:) .* G .* dQds(2,:) + 3 .* dFds(2,:)...
.* K .* dQds(1,:) + 3 .* dFds(2,:) .* K .* dQds(2,:))...
+ 3 .* dFds(3,:) .* G .* dQds(3,:));

FF(1,:) = -(-2 .* G .* dQds(2,:) + 4 .* G .* dQds(1,:) ...
+ 3 .* K .* dQds(2,:) + 3 .* K .* dQds(1,:)) ./...
(4 .* dFds(1,:) .* G .* dQds(1,:) - 2 .* dFds(1,:)...
.* G .* dQds(2,:) + 3 .* dFds(1,:) .* K .* dQds(1,:) + ...
3 .* dFds(3,:) .* G .* dQds(3,:) + 3 .* dFds(1,:) .*...
K .* dQds(2,:) + 3 .* dFds(2,:) .* K .* dQds(1,:))...
+ 3 .* dFds(2,:) .* K .* dQds(2,:) - 2 .* dFds(2,:) .*...
G .* dQds(1,:) + 4 .* dFds(2,:) .* G .* dQds(2,:));

FF(2,:) = -(4 .* G .* dQds(2,:) - 2 .* G .* dQds(1,:) +...
3 .* K .* dQds(2,:) + 3 .* K .* dQds(1,:)) ./ (4 .*...
dFds(1,:) .* G .* dQds(1,:) - 2 .* dFds(1,:) .* ...
G .* dQds(2,:) + 3 .* dFds(1,:) .* K .* dQds(1,:) + ...
3 .* dFds(3,:) .* G .* dQds(3,:) + 3 .* dFds(1,:)...
.* K .* dQds(2,:) + 3 .* dFds(2,:) .* K .* dQds(1,:))...
+ 3 .* dFds(2,:) .* K .* dQds(2,:) - 2 .* dFds(2,:)...
.* G .* dQds(1,:) + 4 .* dFds(2,:) .* G .* dQds(2,:));

FF(3,:) = -3 .* G .* dQds(3,:) ./ (4 .* dFds(1,:) .*...
G .* dQds(1,:) - 2 .* dFds(1,:) .* G .* dQds(2,:))...
+ 3 .* dFds(1,:) .* K .* dQds(1,:) + 3 .* dFds(3,:)...
.* G .* dQds(3,:) + 3 .* dFds(1,:) .* K .* dQds(2,:) + ...
3 .* dFds(2,:) .* K .* dQds(1,:) + 3 .* dFds(2,:)...
.* K .* dQds(2,:) - 2 .* dFds(2,:) .* G .* dQds(1,:))...
+ 4 .* dFds(2,:) .* G .* dQds(2,:));

%*****
Stress = dt*shiftdim(sum(reshape(reshape( D, ...
[9, Size_ij]).*repmat(Strain,3,1), [3,3,Size_ij]),1)...
+ Stress + [[FF(1,:).*F_old(1,)];...
[FF(2,:).*F_old(1,)]; [FF(3,:).*F_old(1,)]]);

Sxx_eff(ij) = Stress(1,:);

```

```
Syy_eff(ij) = Stress(2,:);  
Txy_eff(ij) = Stress(3,:);  
end  
% END OF Plasticity.m
```

## **Part II Scientific papers**

# Paper I

1 **Failure patterns caused by localized rise in pore-fluid overpressure and effective strength**  
2 **of rocks**

3

4 A.Y. Rozhko<sup>1</sup>, Y.Y. Podladchikov<sup>1</sup>, and F. Renard<sup>1,2</sup>

5 <sup>1</sup>Physics of Geological Processes, University of Oslo, PO box 1048 Blindern, 0316  
6 Oslo, Norway

7 <sup>2</sup>LGCA-CNRS-OSUG, University of Grenoble, BP 53, 38041 Grenoble, France

8 **Abstract.** In order to better understand the interaction between pore-fluid overpressure  
9 and failure patterns in rocks we consider a porous elasto-plastic medium in which a  
10 laterally localized overpressure line source is imposed at depth below the free surface.  
11 We solve numerically the fluid filtration equation coupled to the gravitational force  
12 balance and poro-elasto-plastic rheology equations. Systematic numerical simulations,  
13 varying initial stress, intrinsic material properties and geometry, show the existence of  
14 five distinct failure patterns caused by either shear banding or tensile fracturing. The  
15 value of the critical pore-fluid overpressure  $p^c$  at the onset of failure is derived from  
16 an analytical solution that is in excellent agreement with numerical simulations. Finally,  
17 we construct a phase-diagram that predicts the domains of the different failure patterns  
18 and  $p^c$  at the onset of failure.

19 **Key words:** pattern formation (4460), fracture and flow (5104), dynamics and  
20 mechanics of faulting (8118), Mechanics, theory and modeling (8020), role of fluids  
21 (8045).

## 22 1. Introduction

23 The effect of the *homogeneous* pore-pressure increase on the strength of crustal rocks  
 24 and failure modes has been studied by many authors e.g. [[Terzaghi, 1923](#); [Skempton,](#)  
 25 [1961](#); [Paterson and Wong, 2005](#)]. Their results show that, provided that the rocks  
 26 contain a connected system of pores, failure is controlled by the Terzaghi's effective  
 27 stress defined as

$$28 \quad \sigma'_{ij} = \sigma_{ij} - p\delta_{ij} \quad (1)$$

29 where  $\sigma_{ij}$  is the total stress;  $p$  is the pore fluid pressure, and  $\delta_{ij}$  is the Kronecker delta  
 30 (by convention, compressive stress is positive).

31 However, many geological systems, such as magmatic dykes, mud volcanoes,  
 32 hydrothermal vents, or fluid in faults, show evidence that pore pressure increase might  
 33 be *localized*, instead of being *homogeneously* distributed [[Jamtveit et al., 2004](#)].  
 34 Localized pore-pressure variations couple pore-fluid diffusion to rock deformation  
 35 through the seepage force generated by pressure gradients [[Rice and Cleary, 1976](#)]. The  
 36 seepage force introduces localized perturbation of the effective stress field and may  
 37 promote various failure patterns. The effect of seepage forces caused by laterally  
 38 homogeneous pore-pressure increase on failure patterns was recently studied  
 39 experimentally by [[Mourgues and Cobbold, 2003](#)]. In the present study, we explore  
 40 both numerically and analytically how an essentially two-dimensional, i.e. localized  
 41 both at depth and laterally, increase in pore-pressure affects failure patterns in porous  
 42 elasto-plastic rocks. In [section 2](#), we discuss the effect of localized pore pressure  
 43 increase on tensile and shear failure. [Section 3](#) is devoted to the characterization of the  
 44 various failure patterns using finite element and finite difference simulations that solve  
 45 the gravitational force balance equation and the fluid filtration equation in a poro-  
 46 elasto-plastic medium. In [section 4](#), we predict the fluid pressure at the onset of failure  
 47 using new analytical solutions. Finally we discuss the geological implications in [section](#)  
 48 [5](#).

## 49 2. Effect of pore pressure on rock failure

50 In nature, rock failure occurs in two different modes: shear bands and tensile fractures.  
 51 Laboratory triaxial experiments show that the Mohr-Coulomb criterion (eq. 2) provides  
 52 an accurate prediction for shear failure [*Paterson and Wong, 2005*]:

$$53 \quad \tau - \sigma'_m \sin(\phi) = C \cos(\phi) \quad (2)$$

54 where  $\tau = \sqrt{(\sigma_{xx} - \sigma_{yy})^2 / 4 + \sigma_{xy}^2}$  is the stress deviator,  $\sigma'_m = \frac{\sigma_{xx} + \sigma_{yy}}{2} - p$  is the mean  
 55 effective stress,  $C$  is the rock cohesion and  $\phi$  is the internal friction angle.

56 On the other hand, Griffith's theory provides a theoretical criterion for tensile failure of  
 57 a fluid-filled crack [*Murrell, 1964*]:

$$58 \quad \tau - \sigma'_m = \sigma_T \quad (3)$$

59 where  $\sigma_T$  is the tensile strength of the rock. This criterion has also been verified  
 60 experimentally [*Jaeger, 1963*].

61 In [Figure 1](#), we show how a homogeneous or localized increase of pore-fluid pressure  
 62 influences rock failure. There, *lm* is the Mohr-Coulomb envelope (eq. 2) and *kl* is the  
 63 tensile cut-off limit (eq. 3). The Mohr circle indicates the initial state of stress, with  
 64 zero pore-fluid overpressure. As the pore-fluid pressure increases homogeneously by an  
 65 amount  $p$ , the radius of the Mohr circle remains constant and the circle is displaced to  
 66 the left until it touches the failure envelope (blue curve). Depending on the location  
 67 where the circle touches the failure envelope, the formation of shear bands or tensile  
 68 fractures takes place. In both cases, when pore-fluid pressure increase is homogeneous,  
 69 the orientation and onset of failure patterns can be predicted [*Paterson and Wong,*

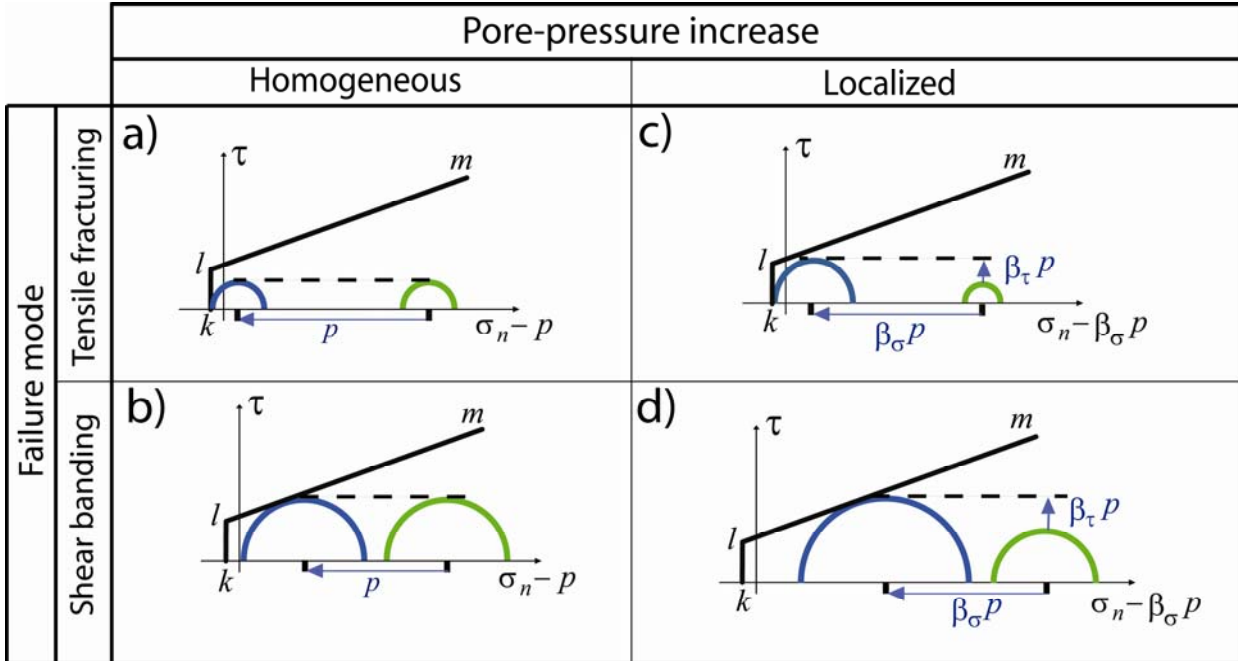
70 [2005](#)]. Shear bands form at an angle of  $\frac{\pi}{4} - \frac{\phi}{2}$  to the direction of maximum

71 compressive stress; tensile fractures develop perpendicularly to the direction of  
 72 maximum tensile stress.

73 We explore a more complex scenario, where the pore-fluid increase is localized into a  
 74 narrow source, so that seepage forces modify locally the stress-state. As shown on  
 75 [Figure 1c-d](#), the radius of the initial Mohr circle does not remain constant, as for the  
 76 homogeneous pore-fluid pressure increase case. For a localized fluid pressure increase  
 77 equal to  $p$ , the radius of the Mohr circle is changed by an amount of  $\beta_\tau p$ , and the



78 center of the circle is displaced to the left by an amount of  $\beta_\sigma p$ . The two  
 79 dimensionless parameters  $\beta_\tau$  and  $\beta_\sigma$  are derived below both by numerical and  
 80 analytical means and given by (eqs. 14-15).

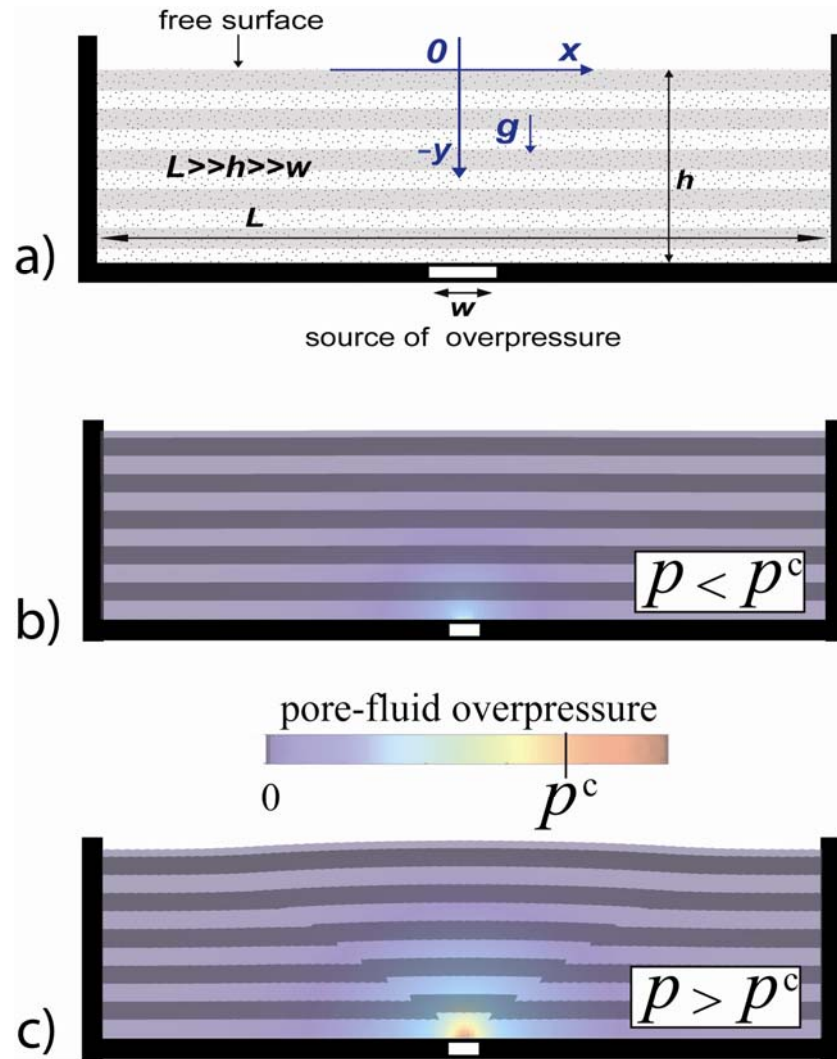


81

82 **Figure 1.** Effect of *homogeneous* (a, b) vs. *localized* (c, d) pore-fluid pressure increase  
 83 on the failure.  $lm$  is the Mohr-Coulomb failure envelope (2);  $kl$  is the tensile cut-off  
 84 boundary (3). The Mohr circles for initial stress conditions are represented in green.  
 85 The Mohr circles after a pore-fluid increase  $p$  are represented in blue (at failure).  
 86 Arrows show the transformation of the Mohr circle after pore-fluid pressure increase.  
 87 The rock fails either in shear mode, or in tension, when the Mohr circle meets the  
 88 failure envelopes  $kl$  or  $lm$ , respectively. Note that for localized pore-fluid pressure  
 89 increase, the radius of the Mohr circle is changed (increase or decrease) by an amount  
 90  $\beta_\tau p$  and the center is displaced to the left by an amount  $\beta_\sigma p$ . The two dimensionless  
 91 parameters  $\beta_\tau$  and  $\beta_\sigma$  are given in equations 14-15.

### 92 3. Numerical model and numerical results

93 We consider a 2D porous medium embedded in a box of length  $L$  and height  $h \ll L$   
 94 (Figure 2a). At the bottom of this box, we define a pore-fluid over-pressure source of  
 95 width  $w \ll h$ . We consider plane-strain deformation in a material with constant and  
 96 homogeneous intrinsic properties. We solve numerically the fluid filtration equation  
 97 and the force balance equation, using a poro-elasto-plastic rheology relationship  
 98 between the stress and the strain rates.



99

100 **Figure 2.** Geometry of the plane-strain model (a) and representative stages of  
 101 deformation before (b) and during failure (c). The color coding represents the pore-fluid  
 102 pressure normalized to the pressure at the onset of failure  $p^c$ . The horizontal layering  
 103 represents passive markers of the deformation.

104

105 At initial conditions the deformation of the material and the pore-fluid overpressure are  
 106 equal to zero everywhere in the system. The initial mechanical state is chosen below the  
 107 failure limits everywhere in the system. The initial vertical stress  $\sigma_v$  (along y axis) is  
 108 equal to the weight of the overburden. The initial horizontal stress  $\sigma_H$  is proportional  
 109 to the vertical stress:

110

$$\begin{aligned} \sigma_v &= -\rho g y \\ \sigma_H &= A\sigma_v \end{aligned}, \quad (4)$$

111 where  $\rho$  is the total density of the rock including pore fluid,  $g$  is the gravitational acceleration,  
 112  $-y$  is the depth and  $A$  is a constant coefficient. The initial shear stress is zero everywhere.  
 113 The top boundary ( $y = 0$ ) has a free surface condition, with zero overpressure ( $p^f = 0$ ). The  
 114 lateral and bottom walls are fixed, with free-slip condition (including the pore-fluid source),  
 115 and impermeable (excluding pore-fluid source). The boundary conditions on lateral walls  
 116 represent far-field fluid pressure and mechanical state undisturbed by the localized fluid  
 117 pressure at the center of the model, which is achieved by using large enough horizontal extent  
 118 of the models,  $L \gg \max(h, w)$ . Perturbations of stress and displacement are negligibly small at  
 119 the lateral boundaries, thus either fixed stress or fixed displacement lateral boundary conditions  
 120 lead to the similar numerical results. At time  $t = 0$ , the fluid pressure is slowly increased  
 121 everywhere on the source segment ( $p^f = p(t)$ ), until failure nucleates and propagates. The  
 122 process of fluid overpressure build up at a small segment of lower boundary is unspecified but  
 123 assumed slow compared to the characteristic time for establishing a steady-state distribution of  
 124 the fluid pressure. This quasi-static slowly driven evolution of the pressure field in a domain  
 125 with constant permeability is governed by the Laplace equation

$$126 \quad \nabla^2 p^f = 0. \quad (5)$$

127 The gravitational force balance equation formulated for the total stress is given by

$$128 \quad \begin{cases} \frac{\partial \sigma_{xx}}{\partial x} + \frac{\partial \sigma_{xy}}{\partial y} = 0 \\ \frac{\partial \sigma_{yy}}{\partial y} + \frac{\partial \sigma_{yx}}{\partial x} + \rho g = 0 \end{cases} \quad (6)$$

129 The initial state of the stress defined in (eq. 4) fulfills this relationship.

130 Using the general approach for poro-elasto-plastic deformation [*Rice and Cleary, 1976;*  
 131 *Vermeer, 1990*], the full strain rate tensor is given by

$$132 \quad \dot{\epsilon}_{ij} = \dot{\epsilon}_{ij}^{pe} + \dot{\epsilon}_{ij}^{pl} \quad (7)$$

133 where the superscripts  $pe$  and  $pl$  denote the poro-elastic and the plastic components,  
 134 respectively. The poro-elastic constitutive relation can be written as:

$$135 \quad \sigma_{ij} = 2G \epsilon_{ij}^{pe} + 2G \epsilon_{kk}^{pe} \frac{\nu}{1-2\nu} \delta_{ij} + \alpha p^f \delta_{ij} \quad (8)$$

136 where  $\alpha$  is the Biot-Willis poro-elastic coupling constant [[Paterson and Wong, 2005](#)],  
 137  $\nu$  is the drained Poisson's ratio, and  $G$  is the shear modulus. The plastic strain rates  
 138 are given by

$$\begin{aligned} \dot{\epsilon}_{ij}^{pl} &= 0 \text{ for } f < 0 \text{ or } (f = 0 \text{ and } \dot{f} < 0) \\ \dot{\epsilon}_{ij}^{pl} &= \lambda \frac{\partial q}{\partial \sigma'_{ij}} \text{ for } f = 0 \text{ and } \dot{f} = 0 \end{aligned} \quad (9)$$

140 Here, we chose the yield function in the form  $f = \max(f_{tension}, f_{shear})$ , where  $f_{tension}$  and  
 141  $f_{shear}$  are yield functions for failure in tension and in shear, respectively, defined as:

$$\begin{aligned} f_{tension} &= \tau - \sigma'_m - \sigma_T \\ f_{shear} &= \tau - \sigma'_m \sin(\phi) - C \cos(\phi) \end{aligned} \quad (10)$$

143 The parameter  $\lambda$  in ([eq. 9](#)) is the non-negative multiplier of the plastic loading  
 144 [[Vermeer, 1990](#)], and  $q$  is the plastic flow function, defined as follows for tensile  
 145 (associated flow rule) and shear failure (non-associated flow rule), respectively:

$$\begin{aligned} q_{tension} &= \tau - \sigma'_m \\ q_{shear} &= \tau - \sigma'_m \sin(\nu) \end{aligned} \quad (11)$$

147 where  $\nu$  is the dilation angle ( $\nu < \phi$ ). Note that the total stress is used in ([eqs. 6,8](#)),  
 148 whereas the Terzaghi's effective stress ([eq. 1](#)) applies in the failure equations ([9-11](#)).  
 149 Substitution of stresses ([eq. 8](#)) into the force balance equation ([6](#)) renders gradient of  
 150 the fluid pressure, commonly referred as *seepage forces*, as a cause of the solid  
 151 deformation.

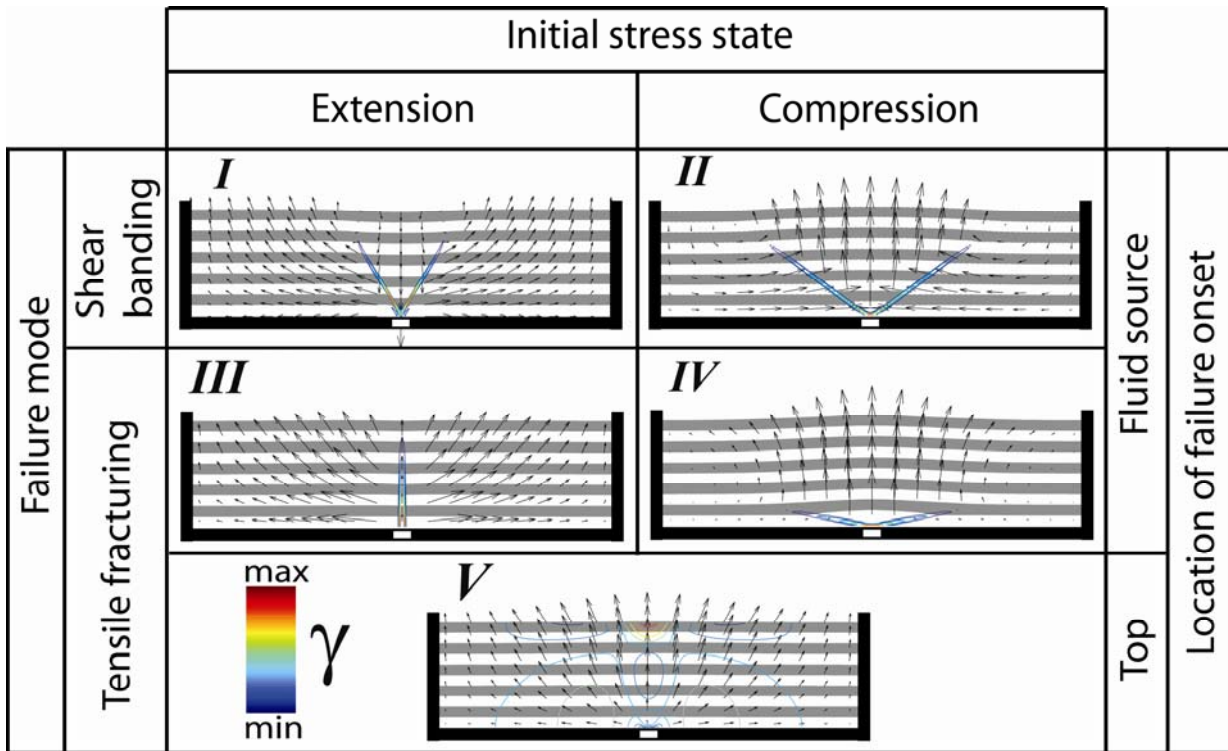
152 Solving this set of equations, we aim to predict the localization and quasi-static  
 153 propagation of plastic deformations into either shear bands or tensile fractures. The  
 154 term tensile fracture is used here to describe the inelastic material response in the  
 155 process zone area that accompanies fracture onset and propagation [[Ingraffea, 1987](#)].

156 In order to check the independence of the simulation results on the numerical method,  
 157 we have developed two codes (finite element and finite difference). Extensive  
 158 numerical comparisons indicate that the results converge to the same values when  
 159 increasing the grid resolution. The poro-elastic response of codes was tested using a  
 160 new analytical solution (see [Auxiliary Materials](#)). The plastic response of the code was  
 161 tested by stretching or squeezing of lateral walls. The numerical results were consistent

162 with both numerical [*Poliakov et al., 1993*] and laboratory experiments of rock  
163 deformation [*Paterson and Wong, 2005*].

164 In the case when the lateral walls are fixed, but the localized pore-fluid overpressure  
165 increases, the simulations show that the rock starts swelling poro-elastically (*Figure*  
166 *2b*). When the pore-fluid pressure exceeds a critical threshold value  $p^c$  at the injection  
167 source, the homogeneous deformation evolves into a pattern where either a tensile  
168 fracture or highly localized shear bands nucleate and propagate in a quasi-static manner  
169 (*Figure 2c*).

170 Solving equations (5-11), the model selects the failure mode (shear or tensile) and the  
171 propagation direction. Systematic numerical simulations show the existence of five  
172 distinct failure patterns when the pore-fluid pressure exceeds  $p^c$  (*Figure 3*, see  
173 *Auxiliary Materials* for animations). Deformation patterns I (normal faulting) and II  
174 (reverse faulting) form by shear failure in compressive ( $\sigma_v < \sigma_H$ ) and in extensional  
175 initial stress states ( $\sigma_v > \sigma_H$ ), respectively. Patterns III (vertical fracturing) and IV  
176 (horizontal fracturing) are caused by tensile failure in compressive and extensional  
177 initial stress states, respectively. The nucleation of failure for patterns I-IV is located at  
178 the fluid overpressure source. It is located at the free surface for pattern V, which is  
179 also called *soil-piping* mode in hydrology [*Jones, 1971*]. After nucleation at the free  
180 surface as tensile fracture in response to swelling caused by the fluid pressure build up,  
181 pattern V develops by downwards propagation of a tensile failure.



182

183 **Figure 3.** Possible failure patterns caused by the localized pore-fluid pressure increase.  
 184 Either shear bands (I, II) or tensile fractures (III, IV, V) can develop. Fracture nucleates  
 185 either on the fluid source at depth (I, II, III, IV) or on the free surface (V). Horizontal  
 186 passive marker layering, arrows, and color coding (contours of strain deviator  $\gamma$ )  
 187 indicate the displacement and intensity of the deformation. (See [Auxiliary Materials](#) for  
 188 animations and for numerical parameters used in simulations).

#### 189 4. Analytical solution and failure pattern phase diagram

190 We have derived an analytical solution for pre-failure stress distribution caused by  
 191 seepage forces sharing the same set of governing parameters as our numerical setup but  
 192 a different geometry of the outer free surface boundary [see [Auxiliary Materials](#)]. We  
 193 report an excellent agreement between numerical and analytical predictions of the  
 194 maximum pre-failure pore-fluid pressure. In order to calculate this critical pore-fluid  
 195 pressure  $p^c$ , we consider the stress and failure conditions at the fluid source (patterns I-  
 196 IV in [Figure 3](#)) and at the free surface (pattern V in [Figure 3](#)).

197 It follows from the analytical solution that the center,  $\sigma_m$ , and the radius,  $\tau$ , of the  
 198 Mohr circle do not vary along the fluid source segment. They are related by the  
 199 following expressions to the initial (and far field or “global”) stresses and to the fluid  
 200 overpressure at the localized source [[Auxiliary Materials](#)]:

$$201 \quad \tau = \left| \frac{\sigma_v - \sigma_H}{2} - \beta_\tau p \right| \quad (12)$$

$$202 \quad \sigma'_m = \sigma_m - p = \frac{\sigma_v + \sigma_H}{2} - \beta_\sigma p \quad (13)$$

203 where two parameters  $\beta_\sigma$  and  $\beta_\tau$  control the shift of Mohr circle and radius change,  
204 respectively (Figure 1):

$$205 \quad \beta_\sigma = 1 - \frac{\alpha}{2} \frac{1-2\nu}{1-\nu} \left( 1 - \frac{1}{2} \frac{1}{\ln\left(\frac{4h}{w}\right)} \right), \quad (14)$$

$$206 \quad \beta_\tau = \frac{\alpha}{4} \frac{1-2\nu}{1-\nu} \frac{1}{\ln\left(\frac{4h}{w}\right)}. \quad (15)$$

207 Using  $\tau$  and, according to the Terzaghi's law (eq. 1),  $\sigma'_m = \sigma_m - p$  in the *local* (i.e.  
208 evaluated at the potential failure point) failure criteria allows predictions of failure  
209 pattern and initiation criteria as a function of the “*global*” and undisturbed by the  
210 localized fluid pressure rise far-field stresses  $\sigma_v$  and  $\sigma_H$ . Equations 12-13 can be  
211 interpreted as a generalized form of the Terzaghi's law expressed in terms of the far-  
212 field stresses for the case of “local” fluid pressure not necessarily equal to the far-field  
213 fluid pressure. According to (eq. 15), during the fluid pressure increase, the radius of  
214 the Mohr-circle decreases when  $\frac{\sigma_v - \sigma_H}{2} - \frac{\eta}{2} \frac{p}{\ln\left(\frac{4h}{w}\right)}$  is positive (patterns I and III) and  
215 increases when it is negative (patterns II and IV). In the case when  $\ln\left(\frac{4h}{w}\right) \ll 1$ , the  
216 radius of the Mohr circle does not vary. If the rock is incompressible ( $\nu = 0.5$ ) or if the  
217 Biot-Willis coupling constant is set to zero, then equations (14-15) recovers the  
218 expected Terzaghi's limit ( $\beta_\sigma = 1$  and  $\beta_\tau = 0$ ) Indeed, the case when the fluid pressure  
219 gradients are not coupled to solid deformation must be in agreement with the classical  
220 effective stress law well supported by experiments with a homogeneous fluid pressure  
221 distribution [Garg and Nur, 1973; Paterson and Wong, 2005].

222 Thus, after evaluating initial stresses at depth  $y = -h$  using (eq. 4) and substitution of  $\tau$   
 223 and  $\sigma'_m$  from (eqs. 12-13) using (eqs. 14-15) into the shear and tensile failure  
 224 conditions (eqs. 2-3), the critical pore-fluid pressure  $p^c$  is calculated. Similarly, using  
 225 the analytical solution and equation (4) at the free surface we obtain  $\sigma_H = 0$  and the  
 226 tensile failure condition:  $2\beta_\tau p^c = \sigma_T$  for failure pattern V.

227 Based on the above calculations, we obtain a generalized expression for failure criteria  
 228 for all failure patterns as a linear combination of initial stresses evaluated at appropriate  
 229 depth:

$$230 \quad k_b(\sigma_H - \sigma_V) = k_\tau + k_\sigma(\sigma_V + \sigma_H) - k_f p^c \quad (16)$$

231 By rearranging, we obtain a unified expression for the critical pore-fluid pressure  $p^c$ :

$$232 \quad p^c = \frac{k_b(\sigma_V - \sigma_H) + k_\tau + k_\sigma(\sigma_V + \sigma_H)}{k_f} \quad (17)$$

233 where  $k_b$ ,  $k_\tau$ ,  $k_\sigma$ , and  $k_f$  are constant coefficients (see Table 1) for the various failure  
 234 patterns shown on Figure 3.

235

	$k_f$	$k_\tau$	$k_\sigma$	$k_b$
I	$2(\beta_\tau + \sin(\phi)\beta_\sigma)$	$2C \cos(\phi)$	$\sin(\phi)$	1
II	$2(\beta_\tau - \sin(\phi)\beta_\sigma)$	$-2C \cos(\phi)$	$-\sin(\phi)$	1
III	$2(\beta_\tau + \beta_\sigma)$	$2\sigma_T$	1	1
IV	$2(\beta_\tau - \beta_\sigma)$	$-2\sigma_T$	-1	1
V	$2\beta_\tau$	$\sigma_T$	0	0

236 **Table 1.** Critical pore-pressure  $p^c = \frac{k_b(\sigma_V - \sigma_H) + k_\tau + k_\sigma(\sigma_V + \sigma_H)}{k_f}$  at the onset of

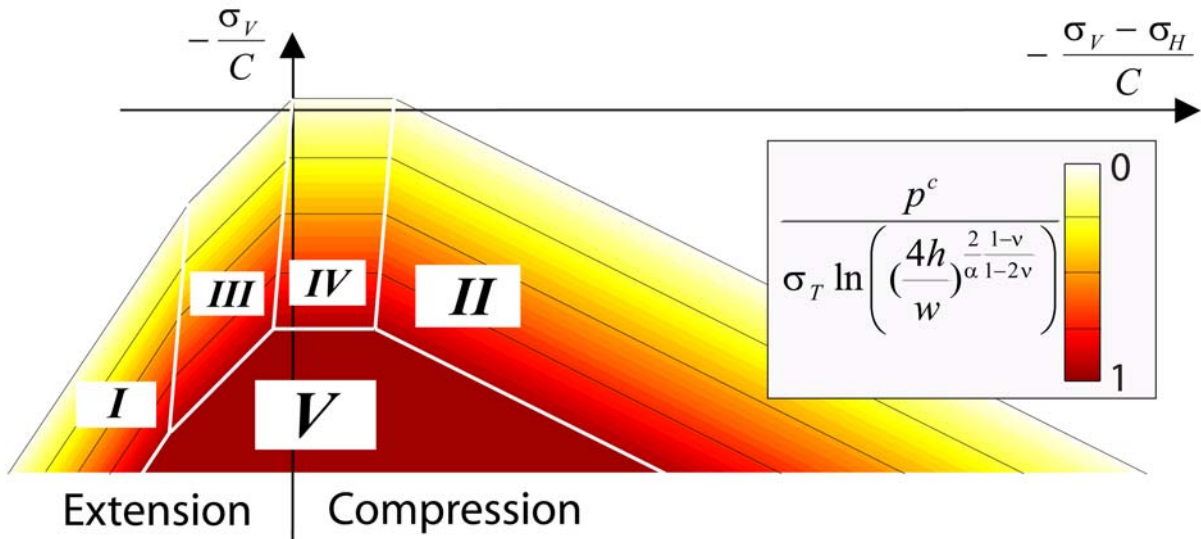
237 failure, corresponding to the various failure patterns (I-V) shown on Figure 3. The  
 238 coefficients also define the domains in the phase diagram of Figure 4.

239

240 Using these coefficients and equation (17), the phase-diagram for the different failure  
 241 patterns can be calculated. The minimum value of  $p^c$  for patterns I-V defines the pore-



242 fluid overpressure at failure nucleation (Figure 4, red colors). If  $p^c \leq 0$ , the rock is at  
 243 failure without fluid overpressure (Figure 4, white color). In Figure 4, the vertical axis  
 244 corresponds to the vertical stress  $\sigma_V$  and the horizontal axis to the stress difference  
 245  $(\sigma_V - \sigma_H)$ , both axes being normalized by  $C$ , the cohesion of the rock. Any initial  
 246 stress state in the model corresponds to a point on the diagram. The contours in the  
 247 colored regions plot the dimensionless pressure  $p^{c*} = \frac{2\beta_r}{\sigma_T} p^c$  at failure onset. If the  
 248 value of the localized pore-fluid pressure is smaller than  $p^{c*}$ , then the system is stable.  
 249 However, if it is equal or larger, then the porous material fails with a predictable  
 250 pattern-onset, that depends on the position in the phase diagram.



251

252 **Figure 4.** Phase diagram of failure-onset patterns. On the vertical axis the non-  
 253 dimensional vertical stress is plotted, while on the horizontal axis the non-dimensional  
 254 stress-difference between vertical and horizontal stresses is plotted. Stresses are given  
 255 at the fluid source at depth. The colored region represents the admissible stress state at  
 256 which the rock is stable, while the outer region represents the unstable combination of  
 257 stresses. The colors plot the non-dimensional critical fluid pressure. The bold white  
 258 lines represent the topology of transitions between the different failure modes.  
 259 Interestingly, failure patterns IV and V may occur both in extensional and in  
 260 compressive initial stress state.

261

262 White thick lines on Figure 4 define the topology of transition boundaries between  
 263 different failure patterns ( $p_i^c = p_j^c$  where  $i$  and  $j$  are patterns I-V in (eq. 17) and  
 264 Table1,  $i \neq j$ ). Their equations can be calculated using equation (17) and the

265 parameters given in [Table 1](#). If a point in the failure diagram lies on one of these  
266 transition lines, the yield functions for the two corresponding domains are both equal to  
267 zero, implying that both failure modes could occur.

## 268 **5. Conclusion**

269 We present an analytical and numerical analysis of the effect of a localized pore-fluid  
270 pressure source on the failure pattern of crustal rocks. The main results are the  
271 following:

- 272 - Depending on the initial conditions, the geometry, and the material properties,  
273 five different patterns of failure can be characterized, either with tensile or shear  
274 mode.
- 275 - The critical fluid pressure at the onset of failure could also be determined for all  
276 failure patterns and an analytical solution for  $p^c$  is given in equation (17) and  
277 [Table 1](#).

278 These results can be used in many geological applications, including the formation of  
279 hydrothermal vent structures triggered by sill intrusion [[Jamtveit et al., 2004](#)], the  
280 aftershocks activities caused by motions of fluids inside faults [[Miller et al., 2004](#)], or  
281 the tremors caused by sediments dehydration in subduction zones [[Shelly et al., 2006](#)].  
282 Finally, our simulations did not allow studying any transient effects in the fluid  
283 pressure during fracture propagation. It has also been shown that fluid lubrication  
284 [[Brodsky and Kanamori, 2001](#)] could have strong effect on the dynamics of rupture  
285 propagation. We are currently neglecting these additional effects, which could be  
286 integrated in an extended version of our model.

287

288 **Acknowledgments:** This work was financed by PGP (Physics of Geological  
289 Processes) a Center of Excellence at the University of Oslo.

290

## 291 **References**

292 Brodsky, E. E. and H. Kanamori (2001), The elastohydrodynamic lubrication of faults,  
293 *Journal of Geophysical Research*, 106(B8), 357-374.

- 294 Ingrafea, A. R. (1987), Theory of crack initiation and propagation in rock, in Fracture  
295 Mechanics of Rock, edited by B. K. Atkinson, pp. 71-110, Academic Press, London.
- 296 Garg, S. K., and A. Nur (1973), Effective stress laws for fluid-saturated porous rocks,  
297 *Journal of Geophysical Research*, 78(26), 5911-5921.
- 298 Jaeger, J. C. (1963), Extension Failures in Rocks Subject to Fluid Pressure, *Journal of*  
299 *Geophysical Research*, 68, 6066-6067.
- 300 Jamveit, B., H. Svensen, J.J. Podladchikov, and S. Planke (2004), Hydrothermal vent  
301 complexes associated with sill intrusions in sedimentary basins, *Geological Society*  
302 *of London, Special Publications*, 234, 233-241.
- 303 Jones, A. (1971), Soil piping and stream channel initiation, *Water Resources Research*,  
304 7, 602–610.
- 305 Miller S. A., C. Collettini, L. Chiaraluce, M. Cocco, M. Barchi, and B. Kaus (2004),  
306 Aftershocks driven by a high pressure CO<sub>2</sub> source at depth, *Nature*, 427, 724-727.
- 307 Mourgues R., and P.R. Cobbold (2003), Some tectonic consequences of fluid  
308 overpressures and seepage forces as demonstrated by sandbox modeling,  
309 *Tectonophysics*, 376, 75-97.
- 310 Murrell, S. A. F. (1964), The theory of propagation of elliptical Griffith cracks under  
311 various conditions of plane strain or plain stress. Parts 2, 3; *British Journal of*  
312 *Applied Physics*, 15, 1211-23.
- 313 Paterson, M. S., and Wong, T.-F. (2005), *Experimental Rock Deformation-The Brittle*  
314 *Field*, 346 pp., Springer, Berlin.
- 315 Poliakov, A.N.B, Y. Podladchikov, and C. Talbot (1993), Initiation of salt diapirs with  
316 frictional overburdens: numerical experiments, *Tectonophysics*, 228, 199-210.
- 317 Rice, J. R., and M. P. Cleary (1976), Some basic stress-diffusion solutions for fluid-  
318 saturated elastic porous media with compressible constituents, *Reviews of*  
319 *Geophysics and Space Physics*, 14, 227-241.
- 320 Shelly, D. R., G. C. Beroza, S. Ide, and S. Nakamura (2006), Low-frequency  
321 earthquakes in Shikoku, Japan and their relationship to episodic tremor and slip,  
322 *Nature*, 442, 188-191, doi:10.1038/nature04931.
- 323 Skempton, A.W. (1961), *Effective stress in soil, concrete and rocks*, in Pore Pressure  
324 and Suction in Soils, pp. 4-16, Butterworths, London.

- 325 Terzaghi, K. (1943), *Theoretical Soil Mechanics*, John Wiley and Sons, 528 pp., New  
326 York.
- 327 Vermeer, P.A. (1990), The orientation of shear bands in biaxial tests, *Géotechnique*,  
328 40(2), 223-236.

## Auxiliary Materials

### Failure patterns caused by localized rise in pore-fluid overpressure and effective strength of rocks

A.Y. Rozhko<sup>1</sup>, Y.Y. Podladchikov<sup>1</sup>, and F. Renard<sup>1,2</sup>

<sup>1</sup> Physics of Geological Processes, University of Oslo, PO box 1048 Blindern, 0316 Oslo, Norway

<sup>2</sup> LGCA-CNRS-OSUG, University of Grenoble, BP 53, 38041 Grenoble, France

In [Section A](#) of this Auxiliary Materials, we demonstrate the analytical solution and derive equations (12-17) of [Section 4](#) in the article. [Section B](#) is devoted to the comparison of the analytical solution to numerical tests. Finally, some animations of the results shown in [Figure 3](#) are presented in [Section C](#).

#### A. Analytical Solution

In this section we calculate the seepage forces caused by coupling pore-fluid diffusion with rock deformation. The procedure for calculating these forces can be divided into six successive steps:

- 1) The definition of the system of equations for mechanical equilibrium;
- 2) the general solution of this system of equations in Cartesian coordinates using the complex potential method for poro-elasticity;
- 3) the introduction of the curvilinear coordinate system associated with the conformal mapping transformation, which allows finding the solution for complex geometry;
- 4) the calculation of the general solution of the equilibrium equations for steady-state poro-elasticity in curvilinear coordinate system;
- 5, 6) and finally, after defining the boundary conditions, the calculation of the particular solution.

#### A1. System of equations for steady-state poro-elastic deformation

Following the common approach of [[Biot, 1941](#); [Rice and Cleary, 1976](#)], the equations for steady-state fluid filtration in a poro-elastic solid are given by:

- The stress balance equations for the total stress tensor  $\sigma_{ij}$ , without volume forces:

$$\frac{\partial \sigma_{xx}}{\partial x} + \frac{\partial \sigma_{xy}}{\partial y} = 0 \quad \text{and} \quad \frac{\partial \sigma_{yy}}{\partial y} + \frac{\partial \sigma_{xy}}{\partial x} = 0 \quad (\text{S1})$$

- The steady-state fluid filtration governed by the Laplace equation for fluid pressure  $p^f$ :

$$\left( \frac{\partial^2}{\partial x^2} + \frac{\partial^2}{\partial y^2} \right) p^f = 0 \quad (\text{S2})$$

- A constitutive relation between the total stress  $\sigma_{ij}$  and the strain  $\varepsilon_{ij}$ :

$$\varepsilon_{ij} = \frac{\sigma_{ij} - \sigma_m \delta_{ij}}{2G} + \frac{\sigma_m - \alpha p^f}{2G} \delta_{ij} \frac{1-2\nu}{1+\nu} \quad (\text{S3})$$

where  $\delta_{ij}$  is the Kronecker delta and the intrinsic material properties are the shear modulus  $G$ , the drained Poisson's ratio  $\nu$ , and the Biot-Willis poro-elastic constant  $\alpha$  [*Paterson and Wong, 2005*].

## A2. Complex Potential Method for steady-state poro-elasticity

Two-dimensional problems in elasticity can be solved using a complex potential method (CPM), developed by *Kolosov [1909]* and *Muskhelishvili [1977]*. This method has been generalized for thermo-elasticity by *Lebedev [1937]* and others. In this method the general solution for the displacements and stresses is represented in terms of two analytical functions (potentials) of a complex variable and another complex function for temperature distribution [*Goodier and Hodge, 1958; Timoshenko and Goodier, 1982*]. This general solution automatically satisfies the force balance equation and generalized Hooke's law for thermo-elasticity, provided that the function of temperature distribution satisfies to the heat conduction equation. The nontrivial part of this method is in satisfying the boundary conditions of the specific problem, which is done by conformal mapping.

The equations for poro-elasticity and thermo-elasticity are identical for steady-state fluid filtration and heat flow problems. Therefore it is possible to use the complex potential method, developed for thermo-elasticity, to solve steady-state poro-elastic problems.

According to the CPM, the general solution of equations (S1-S3) can be written in the form (by convention, compressive stress and strain are positive) [*Goodier and Hodge, 1958; Timoshenko and Goodier, 1982; Muskhelishvili, 1977*]:

$$\sigma_{xx} + \sigma_{yy} = -4\text{Re}[\varphi'(z)] + 2\eta p^f(z, \bar{z}) \quad (\text{S4})$$

$$\sigma_{yy} - \sigma_{xx} + 2i\sigma_{xy} = -2[\bar{z}\varphi''(z) + \psi'(z)] + 2\eta \int \frac{\partial p^f(z, \bar{z})}{\partial z} d\bar{z} \quad (\text{S5})$$

$$2G(u_x + iu_y) = \chi\varphi(z) - z\overline{\varphi'(z)} - \overline{\psi(z)} + \eta \int p^f(z, \bar{z}) dz \quad (\text{S6})$$

Where the plane-strain parameters  $\eta$  and  $\chi$  are defined as:  $\eta = \frac{\alpha}{2} \frac{1-2\nu}{1-\nu}$  and  $\chi = 3-4\nu$ .

The integrals in (eqs. S5-S6) are indefinite (without the integration constant) and the superscript “ ’ ” denotes differentiation, i.e.  $\varphi'(z) = \frac{\partial \varphi(z)}{\partial z}$ .

In equations (S4-S6),  $z = x + iy$  is the complex variable,  $x$  and  $y$  are the usual Cartesian coordinates,  $i = \sqrt{-1}$  is the imaginary unit, and the overbar denotes complex conjugation, i.e.  $\bar{z} = x - iy$ .  $\varphi(z)$  and  $\psi(z)$  are the complex potentials, which are analytic functions of the complex variable  $z$ , and are derived from the biharmonic Airy function [Muskhelishvili, 1977].  $p^f(z, \bar{z})$  is the solution of Laplace equation (S2), given as a function of two complex variables  $z$  and  $\bar{z}$ . By introducing the transformation of coordinates  $x = \frac{z + \bar{z}}{2}$  and  $y = \frac{z - \bar{z}}{2i}$ , the Laplace equation (S2) can be rewritten in the form [Timoshenko and Godier, 1982; Lavrent'ev and Shabat, 1972]:

$$\frac{\partial^2}{\partial z \partial \bar{z}} p^f(z, \bar{z}) = 0. \quad (\text{S7})$$

The fluid filtration pressure creates stresses at the boundaries of the solid. The boundary value problem, with given stresses or displacements in curvilinear boundaries, can be solved by finding the complex potentials  $\varphi(z)$  and  $\psi(z)$  using Muskhelishvili's method.

### A3. Conformal transformation and curvilinear coordinates

Conformal mapping is a transformation of coordinates that allows for solving a problem with a simple geometry (Figure S1a) and transforming its solution to a more complex geometry (Figure S1b). The properties of conformal mapping can be found in [Lavrent'ev and Shabat, 1972].

The transformation of a circular domain into an elliptical one is given in a unique way by the Joukowski transform:

$$z = \frac{w}{4} \left( \zeta + \frac{1}{\zeta} \right) \quad (\text{S8})$$

where  $w$  is the width of pore-fluid pressure source as defined in [Figure 2](#) (and [Figure S1b](#), red line). The complex variable  $\zeta$  is defined through polar coordinates  $\rho$  and  $\vartheta$  as follows ([Figure S1a](#)):

$$\zeta = \rho e^{i\vartheta}. \quad (\text{S9})$$

In [Figure S1a](#),  $1 \leq \rho \leq \rho_*$  and  $0 \leq \vartheta \leq 2\pi$ ; the internal ( $\rho=1$ ) and external ( $\rho=\rho_*$ ) boundaries are shown by the red and brown curves, respectively.

We use the polar coordinates  $\rho$  and  $\vartheta$  in the  $\zeta$ -plane, as a non-dimensional system of coordinates for the  $z$ -plane. The properties of this coordinate system are considered below. Any circle  $\rho = \text{const}$  and radius  $\vartheta = \text{const}$  in the  $\zeta$ -plane ([Figure S1a](#)) are transformed into an ellipse and a hyperbola in the  $z$ -plane, respectively ([Figure S1b](#)). The foci of the ellipse and the hyperbola on the  $z$ -plane coincide ([Figure S1b](#)). As the conformal mapping preserves angles, the two lines  $\vartheta = \text{const}$  and  $\rho = \text{const}$  are perpendicular in the  $z$ -plane. Therefore, the polar coordinates  $\rho$  and  $\vartheta$  can be considered as a curvilinear coordinate system in the  $z$ -plane.

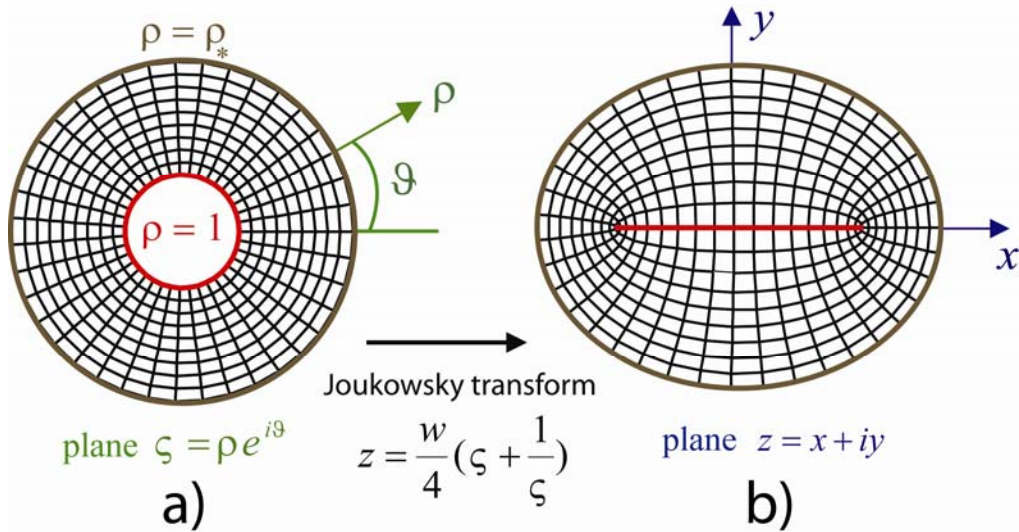


**Figure S1.** Conformal mapping procedure using the Joukowski transform and systems of Cartesian and curvilinear coordinates. Here  $w$  is the length of pore pressure source (red line segment) shown on [Figure 2a](#).



The Cartesian and curvilinear coordinates on the z-plane are related through:

$$\begin{aligned} x &= \frac{w}{4} \rho \left(1 + \frac{1}{\rho^2}\right) \cos(\mathcal{G}) \\ y &= \frac{w}{4} \rho \left(1 - \frac{1}{\rho^2}\right) \sin(\mathcal{G}) \end{aligned} \quad (\text{S10})$$

The Cartesian coordinates of the pore-pressure source (Figure S1b, red line) are given by substitution of the circle  $\rho = 1$  (Figure S1a, red circle) into (eq. S10):

$$\begin{aligned} x &= \frac{w}{2} \cos(\mathcal{G}) \\ y &= 0 \end{aligned} \quad (\text{S11})$$

The external boundaries  $\rho = \rho_*$  are represented as brown curves on Figure S1. If  $\rho_* \gg 1$ , the relations (S10) become:

$$\begin{aligned} x &= \frac{w}{4} \rho_* \cos(\mathcal{G}) + O\left(\frac{1}{\rho_*^2}\right) \\ y &= \frac{w}{4} \rho_* \sin(\mathcal{G}) + O\left(\frac{1}{\rho_*^2}\right) \end{aligned} \quad \text{for } \rho = \rho_* \gg 1 \quad (\text{S12})$$

By neglecting the terms  $O\left(\frac{1}{\rho_*^2}\right)$  and taking  $\rho_* = \frac{4h}{w}$ , the relationship (S12) becomes

$$\begin{aligned} x &= h \cos(\mathcal{G}) \\ y &= h \sin(\mathcal{G}) \end{aligned} \quad (\text{S13})$$

These equations describe the external boundary, which is given by a circle with radius  $h$ , for the case when  $\frac{4h}{w} \gg 1$  (Figure S1b, brown curve). We derive the analytical solution for this case where  $\frac{4h}{w} \gg 1$ .

#### A4. General solution of plane poro-elasticity in curvilinear coordinates

According to Muskhelishvili [1977], the stress and the displacement components in the Cartesian and Curvilinear coordinate systems are related by:

$$\sigma_{xx} + \sigma_{yy} = \sigma_{\rho\rho} + \sigma_{\mathcal{G}\mathcal{G}} \quad (\text{S14})$$

$$\sigma_{yy} - \sigma_{xx} + 2i\sigma_{xy} = \frac{\rho^2}{\zeta^2} \frac{\overline{\omega'(\zeta)}}{\omega'(\zeta)} \left( \sigma_{\mathcal{G}\mathcal{G}} - \sigma_{\rho\rho} + 2i\sigma_{\rho\mathcal{G}} \right) \quad (\text{S15})$$

and

$$u_x + iu_y = \frac{\rho}{\bar{\zeta}} \frac{|\omega'(\zeta)|}{\omega'(\zeta)} (u_\rho + iu_\vartheta) \quad (\text{S16})$$

where

$$\omega(\zeta) = z = \frac{w}{4} \left( \zeta + \frac{1}{\zeta} \right) \quad (\text{S17})$$

Note that, if  $\rho = 1$  in equations (S15-S16), one obtains using (eq. S17):

$$\frac{\rho^2}{\zeta^2} \frac{\overline{\omega'(\zeta)}}{\omega'(\zeta)} = -1 \quad \text{and} \quad \frac{\rho}{\bar{\zeta}} \frac{|\omega'(\zeta)|}{\omega'(\zeta)} = i \frac{\sqrt{\sin^2(\vartheta)}}{\sin(\vartheta)} = \begin{cases} i & \text{for } 0 < \vartheta < \pi \\ -i & \text{for } \pi < \vartheta < 2\pi \end{cases} \quad (\text{S18})$$

The equations for stresses (S4-S5) and displacements (S6) in the curvilinear coordinate system become:

$$\sigma_{\rho\rho} + \sigma_{\vartheta\vartheta} = -4\text{Re}(\Phi(\zeta)) + 2\eta p^f(\zeta, \bar{\zeta}) \quad (\text{S19})$$

$$\sigma_{\vartheta\vartheta} - \sigma_{\rho\rho} + 2i\sigma_{\rho\vartheta} = -\frac{\zeta^2}{\rho^2} \frac{2}{\omega'(\zeta)} \left[ \overline{\omega(\zeta)} \Phi'(\zeta) + \omega'(\zeta) \Psi(\zeta) \right] + \frac{\zeta^2}{\rho^2} \frac{2}{\omega'(\zeta)} \eta \int \frac{\partial p^f(\zeta, \bar{\zeta})}{\partial \zeta} \overline{\omega'(\zeta)} d\bar{\zeta} \quad (\text{S20})$$

$$2G(u_\rho + iu_\vartheta) = \frac{\bar{\zeta}}{\rho} \frac{\overline{\omega'(\zeta)}}{|\omega'(\zeta)|} \left( \chi\varphi(\zeta) - \frac{\omega(\zeta)}{\omega'(\zeta)} \overline{\varphi'(\zeta)} - \overline{\psi(\zeta)} + \eta \int p^f(\zeta, \bar{\zeta}) \omega'(\zeta) d\zeta \right) \quad (\text{S21})$$

where

$$\Phi(\zeta) = \frac{\varphi'(\zeta)}{\omega'(\zeta)} \quad \text{and} \quad \Psi(\zeta) = \frac{\psi'(\zeta)}{\omega'(\zeta)} \quad (\text{S22})$$

Using the properties of conformal mapping ( $\omega'(\zeta) \neq 0$  and  $\omega(\zeta) \neq 0$ ), the Laplace equation (S7) becomes:

$$\frac{\partial^2 p^f(\zeta, \bar{\zeta})}{\partial \zeta \partial \bar{\zeta}} = 0 \quad (\text{S23})$$

## A5. Boundary conditions

The boundary conditions for the fluid are:

$$\begin{aligned} p^f &= p \quad \text{for } \rho = 1 \\ p^f &= 0 \quad \text{for } \rho = \rho_* \end{aligned} \quad (\text{S24})$$

and the boundary conditions for the solid are:

$$\begin{aligned}\sigma_{xy} &= 0 \text{ and } u_y = 0 \text{ for } \rho = 1 \\ \sigma_{\rho g} &= 0 \text{ and } \sigma_{\rho\rho} = 0 \text{ for } \rho = \rho_*\end{aligned}\tag{S25}$$

Note here that if  $\rho = 1$ , and using (eqs. S14-S18), one obtains  $\sigma_{\rho g} = -\sigma_{xy} = 0$  and  $u_\rho = \pm u_y = 0$ .

We define the pore-fluid pressure source inside the continuous medium (Figure S1b, red line) as a line segment with constant fluid pressure. The external boundary (Figure S1b, brown line) has zero pore pressure. We use mixed boundary conditions for the pore pressure source  $\rho = 1$  as in (eq. S25) because the medium is continuous everywhere and  $y = 0$  is a symmetry line. The external boundary  $\rho = \rho_*$  is free from load.

### A6. Solution

We finally present the analytical solution derived using Muskhelishvili's method. We do not show the derivation here, since it is quite lengthy, but we demonstrate that our solution fulfills to the boundary conditions.

The solution of Laplace equation (S23) with the boundary conditions (S24) is given by,

$$p^f(\zeta, \bar{\zeta}) = p - p \frac{\ln(\zeta \bar{\zeta})}{\ln(\rho_*^2)}\tag{S26}$$

This equation can be simplified, using (eq. S8) as follows

$$p^f(\rho) = p - p \frac{\ln(\rho)}{\ln(\rho_*)}\tag{S27}$$

The boundary conditions (S24) are fulfilled by (eq. S27). This equation (S27) gives the solution for pore fluid pressure.

We calculate the complex potentials, which define the solution of problem, as the following:

$$\varphi(\zeta) = \frac{p \eta w}{16} \frac{\zeta^2 + 1}{\zeta \ln(\rho_*)}\tag{S28}$$

$$\psi(\zeta) = \frac{p \eta w}{4 \zeta \ln(\rho_*)}\tag{S29}$$

The explicit expression for the stress components can be found after substitution of (eq. S26), and (eqs. S28-S29) into (eqs. S19-S20) using (eq. S22), and after simplifications:

$$\sigma_{\rho\rho} = -\eta \frac{p}{\ln(\rho_*)} \left( \ln\left(\frac{\rho}{\rho_*}\right) + 1 - \frac{(\rho^2 - 1)(\rho^2 - \cos(2\mathcal{G}))}{1 - 2\rho^2 \cos(2\mathcal{G}) + \rho^4} \right) \quad (\text{S30})$$

$$\sigma_{\mathcal{G}\mathcal{G}} = -\eta \frac{p}{\ln(\rho_*)} \left( \ln\left(\frac{\rho}{\rho_*}\right) + 1 + \frac{(\rho^2 + 1)(\cos(2\mathcal{G}) - 1)}{1 - 2\rho^2 \cos(2\mathcal{G}) + \rho^4} \right) \quad (\text{S31})$$

$$\sigma_{\rho\mathcal{G}} = -\eta \frac{p}{\ln(\rho_*)} \frac{(\rho^2 - 1) \sin(2\mathcal{G})}{1 - 2\rho^2 \cos(2\mathcal{G}) + \rho^4} \quad (\text{S32})$$

The explicit expression for the displacements can be found after substitution of (eqs. S26, S28-S29) into (eq. S21), using (eqs. S16, S22), and after simplifications we obtain:

$$u_x = w \frac{\eta}{32} \frac{p \cos(\mathcal{G})}{G \ln(\rho_*)} \left[ \left( 4 \ln\left(\frac{\rho_*}{\rho}\right) + \chi + 1 \right) \left( \rho - \frac{1}{\rho} \right) + \left( 4 \ln\left(\frac{\rho_*}{\rho}\right) + \chi - 3 \right) \frac{2}{\rho} \right] \quad (\text{S33})$$

$$u_y = w \frac{\eta}{32} \frac{p \sin(\mathcal{G})}{G \ln(\rho_*)} \left( 4 \ln\left(\frac{\rho_*}{\rho}\right) + \chi + 1 \right) \left( \rho - \frac{1}{\rho} \right) \quad (\text{S34})$$

In equations (S33-S34), we present the analytical solution for the displacements along  $x$  and  $y$  axes. This solution is parameterized through curvilinear coordinates  $\rho$  and  $\mathcal{G}$ . The solution for displacements along  $\rho$  and  $\mathcal{G}$  axes is too long to be reproduced here. One can find this displacements using (eqs. S33-S34) along with (eq. S16).

Applying the boundary conditions (S25) to equations (S32, S34) shows that the solution is fulfilled at the pore overpressure source  $\rho = 1$  (Figure S1, red curve). The non-zero stress components at the pore overpressure source are calculated using (eqs. S30-S31) along with (eqs. S14-S15) and (eq. S18):

$$\sigma_{yy} = \sigma_{\rho\rho} = \eta p - \frac{\eta p}{\ln(\rho_*)} \text{ for } \rho = 1 \quad (\text{S35})$$

$$\sigma_{xx} = \sigma_{\mathcal{G}\mathcal{G}} = \eta p \text{ for } \rho = 1 \quad (\text{S36})$$

According to equation (1) of the article and equations (S27) and (S35-S36), the effective stress at the pore overpressure source becomes

$$\sigma'_{yy} = \eta p - \frac{\eta p}{\ln(\rho_*)} - p \text{ for } \rho = 1 \quad (\text{S37})$$

$$\sigma'_{xx} = \eta p - p \text{ for } \rho = 1 \quad (\text{S38})$$

At the external boundary  $\rho = \rho_*$  (Figure S1, brown curve), we obtain  $\sigma_{\rho\rho} = O\left(\frac{1}{\rho_*^2}\right)$

and  $\sigma_{\rho\theta} = O\left(\frac{1}{\rho_*^2}\right)$ , since  $\rho_* \gg 1$ . The boundary conditions (S25) at  $\rho = \rho_*$  are also fulfilled.

The circumferential stress at the free surface is given by:

$$\sigma_{\theta\theta} = -\eta \frac{p}{\ln(\rho_*)} + O\left(\frac{1}{\rho_*^2}\right) \quad (\sigma_{\theta\theta} = \sigma_{xx} \text{ for } \rho = \rho_* \text{ and } \theta = \frac{\pi}{2}) \quad (\text{S39})$$

According to equation (1) of the paper and equations (S27) and (S39), the non-zero component of effective stress at the free surface is given by

$$\sigma'_{xx} = -\eta \frac{p}{\ln(\rho_*)} \quad (\text{S40})$$

## A7. Critical pore pressure

We now propose an analytical study in order to derive equation (17) of the paper for the fluid pressure  $p^c$  at the onset of failure. To do this, we add the initial state of stress given by equations (4) to the stress of state which is exerted by the fluid overpressure increase (obtained in the Section A6). This is possible due to the additivity of linear poroelasticity [Rice and Cleary, 1976]. Both the numerical simulations and the analytical solution show that failure initiation takes place either at the fluid source or at the free surface. Therefore, in order to calculate  $p^c$ , we consider the stress and failure conditions below, first at the fluid source (patterns I-IV in Figure 3), and second at the free surface (pattern V in Figure 3).

Using equations (S37-S38) at  $(\rho_* = \frac{4h}{w})$  and (eq. 4) (at depth  $y = -h$ ) for failure patterns

I-IV, the Terzaghi's effective stress tensor at the fluid source segment becomes:

$$\sigma'_{xx} = \sigma_H - p + \eta p, \quad (\text{S41})$$

$$\sigma'_{yy} = \sigma_v - p + \eta p - \frac{\eta p}{\ln\left(\frac{4h}{w}\right)}, \quad (\text{S42})$$

$$\sigma'_{xy} = 0. \quad (\text{S43})$$

The analytical solution given in equations (S41-S45) indicates that the stress components on the fluid source do not depend on  $x$  (Figure 2a).

Using (eq. S41-S45), the mean Terzaghi's effective stress  $\sigma'_m$  and the stress deviator  $\tau$  can be calculated:

$$\sigma'_m = \frac{\sigma_H + \sigma_v}{2} - p + \eta p - \frac{\eta}{2} \frac{p}{\ln\left(\frac{4h}{w}\right)} \quad (\text{S44})$$

$$\tau = \left| \frac{\sigma_v - \sigma_H}{2} - \frac{\eta}{2} \frac{p}{\ln\left(\frac{4h}{w}\right)} \right|. \quad (\text{S45})$$

Substitution of equations (S44) and (S45) into the failure condition (2) for shear failure or condition (3) for tensile failure defines  $p^c$  for failure patterns 1-IV. Now, referring to the parameters  $\beta_\sigma$  and  $\beta_\tau$  defined in Figure 1 and to the definition of  $\eta$  after equation (S6), one obtains from (eqs. S44, S45):

$$\beta_\sigma = 1 - \frac{\alpha}{2} \frac{1-2\nu}{1-\nu} \left( 1 - \frac{1}{2} \frac{1}{\ln\left(\frac{4h}{w}\right)} \right), \quad (\text{S46})$$

$$\beta_\tau = \frac{\alpha}{4} \frac{1-2\nu}{1-\nu} \frac{1}{\ln\left(\frac{4h}{w}\right)}. \quad (\text{S47})$$

According to (eq. S47), during the fluid pressure increase, the radius of the Mohr-circle decreases when  $\frac{\sigma_v - \sigma_H}{2} - \frac{\eta}{2} \frac{p}{\ln\left(\frac{4h}{w}\right)}$  is positive (Patterns I and III) and increases when it

is negative (Patterns II and IV) in the case, if  $\ln\left(\frac{4h}{w}\right) \ll 1$  the radius of Mohr circle does not change. If the rock is incompressible ( $\nu = 0.5$ ) or the Biot-Willis coupling constant is

set to zero equations (eqs. S46-S46) give  $\beta_\sigma = 1$  and  $\beta_\tau = 0$  therefore the seepage force does not have an additional effect on failure in this case.

For pattern V in Figure 3, the initial stresses (eq. 4) are zero (at depth  $y = 0$ ). Thus after substitution of (eq. S40) into (eq. 3) and simplification we obtain the condition for tensile failure at the free surface as the following,

$$2\beta_\tau p^c = \sigma_T. \quad (\text{S48})$$

By assuming  $\frac{2C}{1+\sin(\varphi)} > \sigma_T$  we obtain that only tensile failure initiation is allowed at the free surface.

### B. Analytical versus numerical approach

The numerical simulations show that if the initial state of stress ( $\sigma_V$  and  $\sigma_H$ ) is taken as in the form of equations (4), then the nucleation of failure is allowed either at the pore-pressure source or at the free surface. We compare  $p^c$  predicted with the analytical solution ((eq. 17) and Table 1) obtained for the geometry shown on Figure S2a, with  $p^c$  calculated with the finite element method for the geometry shown on Figure S2b.

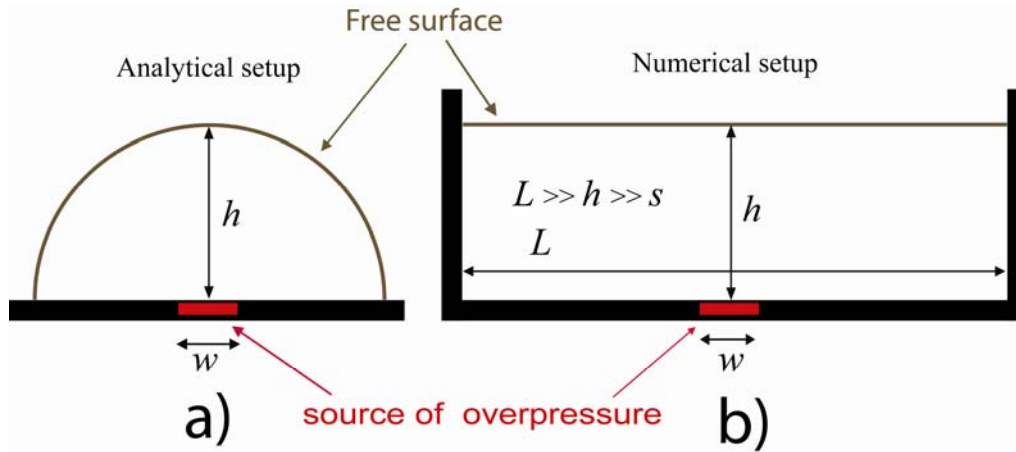


**Figure S2.** Geometry used in the analytical solution (Figure S1) compared to the geometry used in the numerical model (Figure 2a).

We studied  $p^c$  numerically as a function of all parameters of the model. The vertical stress  $\sigma_V$  (Pa or bar) and the depth  $h$  (m) are chosen to be equal to 1 and all the parameters listed below are non-dimensional compared to these values. Plots on Figure S3 compare  $p^c$  predicted with the analytical solution ( $p_{AS}^c$ ) to  $p^c$  calculated with the

numerical simulations ( $p_{NS}^c$ ); the different colors representing the various failure patterns.

The value of  $p^c$  is always within a 20% limit between the two approaches.

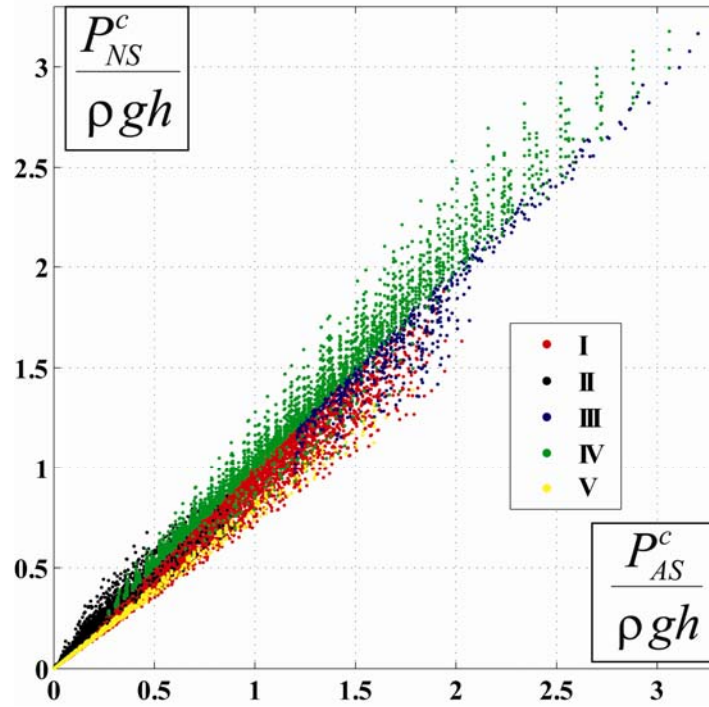


**Figure S3.** Critical pore pressure at the onset of failure predicted using the analytical solution  $p_{AS}^c$  for the geometry shown on [Figure S2a](#) compared to the solution of the numerical simulations  $p_{NS}^c$  for the geometry shown on [Figure S2b](#). Each point corresponds to a single simulation. The different colors correspond to the different failure patterns of [Figure 3](#)

#### List of parameters and values:

Poisson's ratio:  $\nu = \frac{[1:4]}{10}$  (where the notation [1:4] denotes the array [1,2,3,4]).

Non-dimensional width of overpressure source:  $\frac{w}{h} = \frac{2^{-[0:5]}}{5}$ .

Non-dimensional horizontal stress:  $\frac{\sigma_H}{\sigma_V} = \frac{[1:30]}{10}$ .

Non-dimensional cohesion:  $\frac{C}{\sigma_V} = e^{\frac{\ln(1e-4) + (\ln(3) - \ln(1e-4)) \cdot [0:50]}{50}}$ .

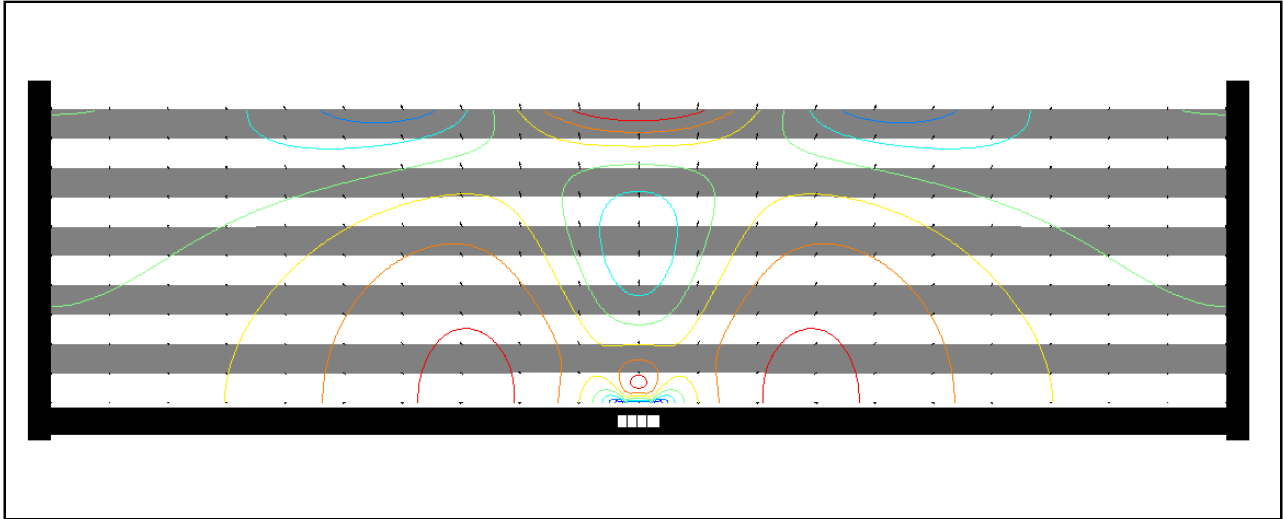
Non-dimensional tensile strength:  $\frac{\sigma_T}{\sigma_V} = \frac{C}{\sigma_V} \left[ \frac{1}{3}, \frac{1}{7}, \frac{1}{30} \right]$ .

Friction angle (in degrees):  $\varphi = 10^\circ [1:3]$ .



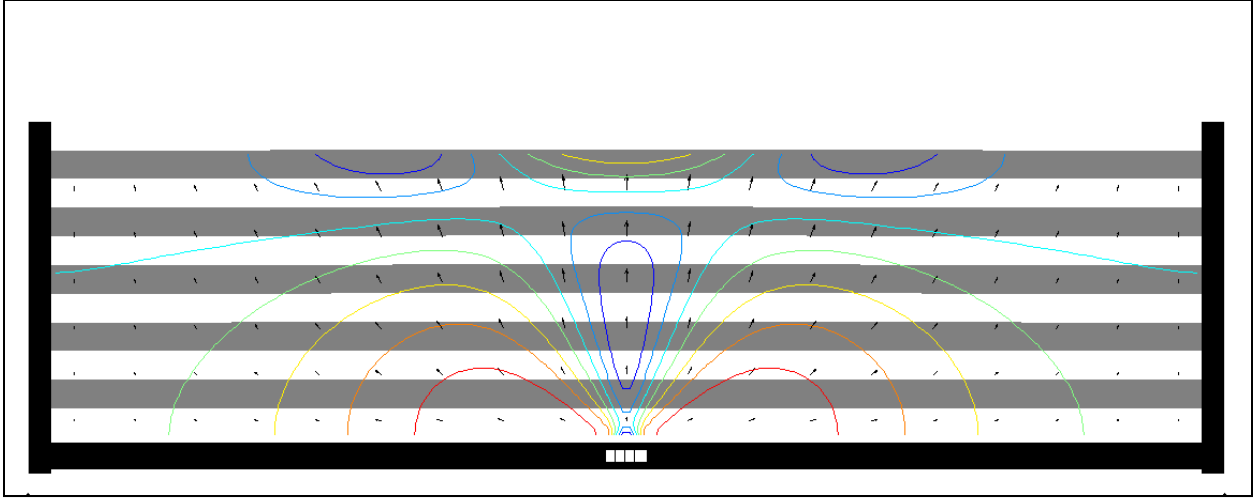
Fixed non-dimensional parameters:  $\frac{L}{h} = 4$ ,  $\frac{G}{\sigma_v} = 10^7$ ,  $\nu = 0^\circ$  and  $\alpha = 1$ .

### C. Animations of the simulations of Figure 3



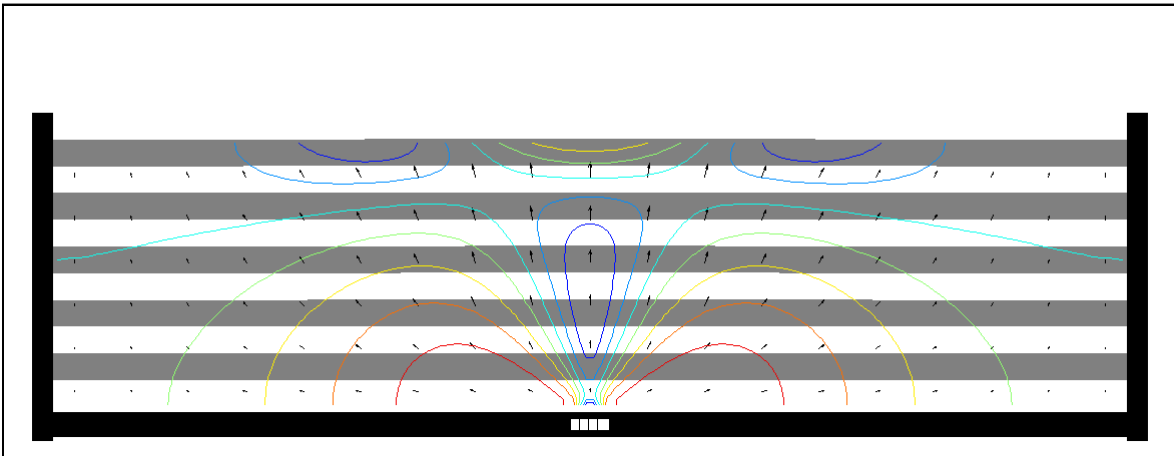
#### Pattern I:

$\frac{\sigma_H}{\sigma_v} = 0.2$ ,  $\varphi = 33^\circ$ ,  $\nu = 0^\circ$ ,  $\frac{C}{\sigma_v} = 0.1$ ,  $\frac{\sigma_T}{\sigma_v} = 1$ ,  $\nu = 0.3$ ,  $\frac{G}{\sigma_v} = 10^7$ ,  $\frac{L}{h} = 4$ ,  $\frac{w}{h} = 10^{-1}$ ,  $\alpha = 1$ . The first frame in the animation corresponds to the elastic solution at failure onset  $p = p^c$ , the last frame corresponds to the case when  $p = 3.5p^c$ . The pore pressure increases linearly with time during the animation.



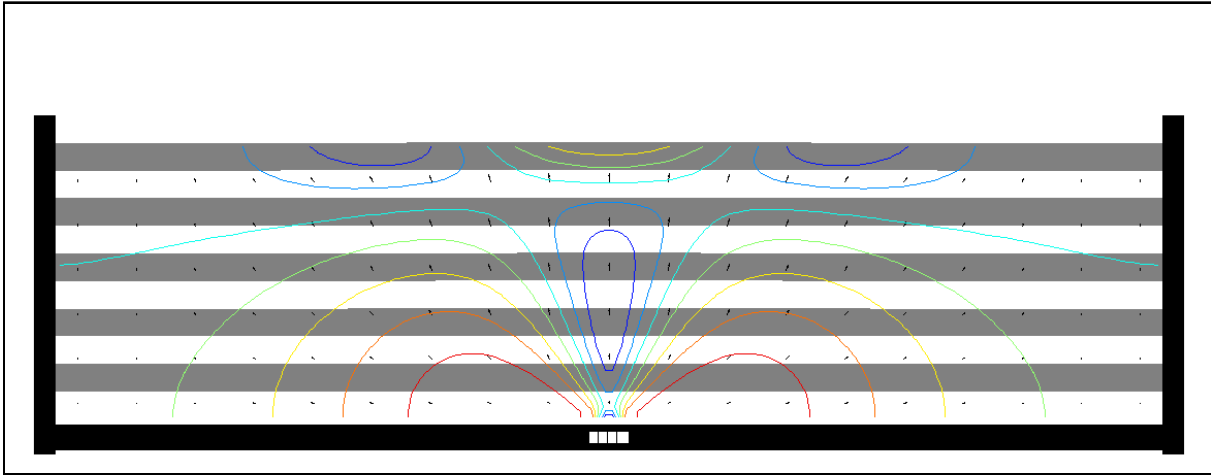
**Pattern II:**

$\frac{\sigma_H}{\sigma_V} = 3$ ,  $\varphi = 33^\circ$ ,  $\nu = 0^\circ$ ,  $\frac{C}{\sigma_V} = 0.1$ ,  $\frac{\sigma_T}{\sigma_V} = 0.1$ ,  $\nu = 0.3$ ,  $\frac{G}{\sigma_V} = 10^7$ ,  $\frac{L}{h} = 4$ ,  $\frac{w}{h} = 10^{-1}$ ,  $\alpha = 1$ . The first frame in the animation corresponds to the elastic solution at failure onset  $p = p^c$ , the last frame corresponds to the case when  $p = 1.8p^c$ . The pore pressure increases linearly with time during the animation.



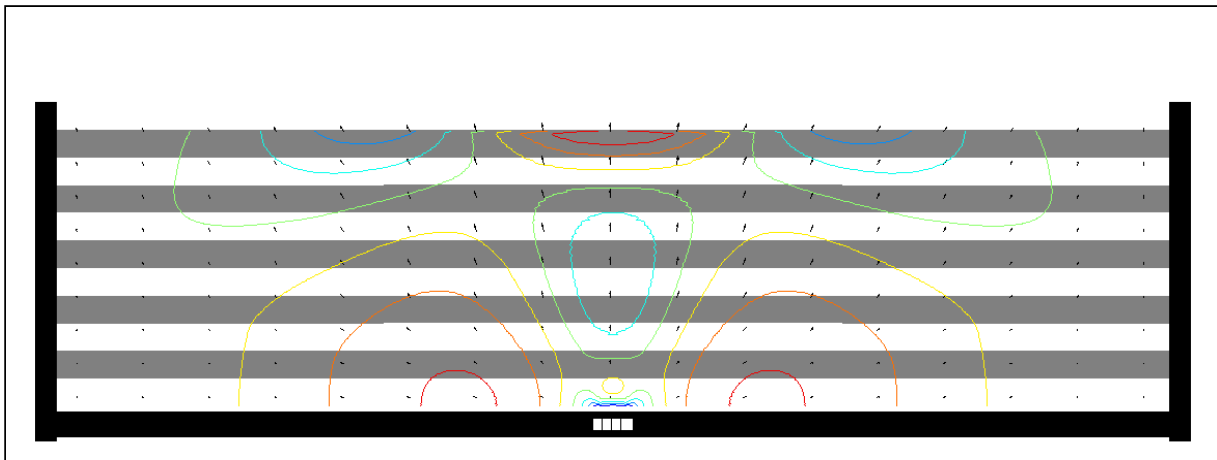
**Pattern III:**

$\frac{\sigma_H}{\sigma_V} = 0.1$ ,  $\varphi = 33^\circ$ ,  $\nu = 0^\circ$ ,  $\frac{C}{\sigma_V} = 0.8$ ,  $\frac{\sigma_T}{\sigma_V} = 0.266$ ,  $\nu = 0.3$ ,  $\frac{G}{\sigma_V} = 10^7$ ,  $\frac{L}{h} = 4$ ,  $\frac{w}{h} = 10^{-1}$ ,  $\alpha = 1$ . The first frame in the animation corresponds to the elastic solution at failure onset  $p = p^c$ , the last frame corresponds to the case when  $p = 4p^c$ . The pore pressure increases linearly with time during the animation.



**Pattern IV:**

$\frac{\sigma_H}{\sigma_V} = 5$ ,  $\varphi = 33^\circ$ ,  $\nu = 0^\circ$ ,  $\frac{C}{\sigma_V} = 4$ ,  $\frac{\sigma_T}{\sigma_V} = 0.266$ ,  $\nu = 0.3$ ,  $\frac{G}{\sigma_V} = 10^7$ ,  $\frac{L}{h} = 4$ ,  $\frac{w}{h} = 10^{-1}$ ,  $\alpha = 1$ . The first frame in the animation corresponds to the elastic solution at failure onset  $p = p^c$ , the last frame corresponds to the case when  $p = 3.2p^c$ . The pore pressure increases linearly with time during the animation.



**Pattern V:**

$\frac{\sigma_H}{\sigma_V} = 0.1$ ,  $\varphi = 33^\circ$ ,  $\nu = 0^\circ$ ,  $\frac{C}{\sigma_V} = 0.8$ ,  $\frac{\sigma_T}{\sigma_V} = 10^{-8}$ ,  $\nu = 0.3$ ,  $\frac{G}{\sigma_V} = 10^7$ ,  $\frac{L}{h} = 4$ ,  $\frac{w}{h} = 10^{-1}$ ,  $\alpha = 1$ . The first frame in the animation corresponds to the elastic solution at failure onset  $p = p^c$ , the last frame corresponds to the case when  $p = 16p^c$ . The pore pressure increases linearly with time during the animation.

**References**

- Biot, M. A. (1941), General theory of three-dimensional consolidation, *Journal of Applied Physics*, 12, 155-164.
- Goodier, J. r. J.N., and Hodge, P.G., (1958), *Elasticity and Plasticity: The Mathematical Theory of Elasticity and The Mathematical Theory of Plasticity*, 152 pp., John Wiley & Sons, New York.
- Lavrent'ev, M. A., and Shabat, B. V. (1972), *Methods of Theory of Complex Variable Functions*, 736 pp., Nauka, Moscow.
- Kolosov, G. V., (1909), *On the Application of the Theory of Functions of a Complex Variable to a Plane problem in the Mathematical Theory of Elasticity*, Ph.D. diss., Dorpat University (in Russian).
- Lebedev, N. N., (1937), Thermal Stresses in the Theory of Elasticity, ONTI, Moscow-Leningrad, 55-56 (in Russian).
- Muskhelishvili, N.I., (1977), *Some Basic Problems in the Mathematical Theory of Elasticity*, 768 pp., Springer, Berlin.
- Paterson, M. S., and Wong, T.-F. (2005), *Experimental Rock Deformation-The Brittle Field*, 346 pp., Springer, Berlin.
- Rice, J. R., and M. P. Cleary (1976), Some basic stress-diffusion solutions for fluid-saturated elastic porous media with compressible constituents, *Reviews of Geophysics and Space Physics*, 14, 227-241.
- Timoshenko, S. P., and Goodier, J.N. (1982), *Theory of Elasticity*, 608 pp., McGraw-Hill, New York.

## **Paper II**

## Role of seepage forces in faulting and earthquake triggering

Alexander Rozhko

Physics of Geological Processes, University of Oslo, PO box 1048 Blindern, 0316  
Oslo, Norway

**Abstract** This article discusses the effects of coupling between deformation and pore-fluid diffusion on faulting and failure processes. I consider an arbitrarily oriented preexisting fault zone of finite length, located at depth, with a given fluid overpressure in it, and surrounded by porous and permeable rocks. The intrinsic elastic and transport properties of these rocks are assumed to be isotropic and homogeneous. The seepage forces caused by steady-state fluid diffusion from the fault zone to the surrounding permeable rocks are calculated analytically using the complex-potentials method for poro-elasticity and conformal mapping. The pore-fluid overpressure required for fault reactivation is calculated analytically in 2D, assuming that the tectonic stress state, the rock intrinsic properties and the geometry of the pre-existing fault are known. I apply the solution to microseismicity triggering caused by hydrocarbon withdrawals from a reservoir. Other applications such as storage of carbon dioxide in porous rocks and geothermic exploitation are also considered. Knowledge of the pore-fluid overpressure needed to reactivate a fault helps to prevent anthropogenic earthquakes.

### 1. Introduction

Fluids exert significant mechanical forces that influence earthquake faulting. The typical effect, which is commonly recognized, is the reduction of the tectonic compressive stress by an amount equal to the pore-fluid pressure. The role of the fault zone as a fluid conduit is also widely recognized [[Rice, 1992](#)] and it is accepted that many fault zones can be characterized by a pore-fluid overpressure  $\Delta p_f$  that can vary in time [[Sibson, 1990](#)]. [Hickman et al. \[1995\]](#) reviewed possible mechanisms that may generate fluid overpressure in faults and shear zones. These sources of overpressure include metamorphic fluids generated by dehydration of minerals during prograde metamorphism, crustal scale circulation of water [[Kerrich et al., 1984](#)], and mantle-derived water and carbon dioxide that may be upwelling along preexisting penetrating faults [[Miller et al., 2004](#)]. Maturation of the organic matter may also control the

fluid pressure through generation of both liquid and gaseous hydrocarbons [*Moore and Vrolijk, 1992*]. Another mechanism that could generate fluid overpressure is industrial injection or extraction of fluid from a fault zone or the fractured zone of a reservoir [*Economides and Nolte, 2000*].

The pore-fluid overpressure  $\Delta p_f$  is the difference between the pore-fluid pressures inside the fault zone  $p_f^i$  and the hydrostatic fluid pressure  $p_f^o$  i.e.,

$$\Delta p_f = p_f^i - p_f^o, \quad (1)$$

and the hydrostatic fluid pressure:

$$p_f^o = \rho_w g h, \quad (2)$$

where  $\rho_w$  is the density of water,  $g$  is the gravitational acceleration and  $h$  is the depth.

The failure of the fault zone is controlled by the effective tectonic stress  $\sigma_{ij}^{T'}$ ,

$$\sigma_{ij}^{T'} = \sigma_{ij}^T - p_f^i \delta_{ij}, \quad (3)$$

where  $\sigma_{ij}^T$  is the tectonic stress on the fault, and  $\delta_{ij}$  is the Kronecker delta ( $\delta_{ij} = \begin{cases} 1 & \text{for } i = j \\ 0 & \text{for } i \neq j \end{cases}$ )

[*Turcotte and Schubert, 2002; Jaeger and Cook, 1979*]. In 2D, the tectonic stress on the fault zone can be characterized by two components: the vertical stress  $\sigma_V^T$  and the horizontal stress  $\sigma_H^T$ :

$$\sigma_V^T = \rho_r g h, \quad (4)$$

$$\sigma_H^T = \rho_r g h + \Delta \sigma_H^T, \quad (5)$$

where  $\rho_r$  is the rock density and  $\Delta \sigma_H^T$  is the tectonic stress difference.

According to the Coulomb criterion [*Jaeger and Cook, 1979; Vermeer and de Borst, 1984*], shear failure of rocks is controlled by the yield function  $f$ , defined as

$$f = \tau - \sigma'_m \sin(\phi) - C \cos(\phi) \leq 0, \quad (6)$$

where  $\tau = \frac{1}{2}\sqrt{(\sigma_{xx} - \sigma_{yy})^2 + 4\sigma_{xy}^2}$  is the stress deviator,  $\sigma'_m = \frac{\sigma_{xx} + \sigma_{yy}}{2} - p_f$  is the mean effective stress,  $\phi$  is the angle of internal friction,  $C$  is the cohesion, and  $\sigma_{ij}$  and  $p_f$  are the local stress tensor and local pore-fluid pressure, respectively.

The rock is stable if  $f < 0$  and fails in shear if  $f = 0$ .

Substitution of the tectonic stress (4-5) into (6) using (1-2) gives a yield condition on the fault zone,

$$f = \frac{1}{2}|\Delta\sigma_H^T| - \left( (\rho_r - \rho_f)gh + \frac{\Delta\sigma_H^T}{2} - \Delta p_f \right) \sin(\phi) - C \cos(\phi) \leq 0. \quad (7)$$

Equation (7) suggests that a positive value of the pore-fluid overpressure ( $\Delta p_f > 0$ ) increases the probability of failure.

Segall [1985] considered the possibility that the Coalinga earthquake in May 1983 was induced by fluid extraction from a reservoir, *i.e.* by a decrease of pore-fluid pressure. Since equation (7) does not support this statement, he suggested that his hypothesis might be explained by the linear theory of poroelasticity [Nikolaevski *et al.*, 1970; Rice and Cleary, 1976; Rudnicki, 2001]. This theory specifies an additional change of stress, called *seepage forces*, caused by the coupling between pore-fluid diffusion and rock deformation. Pore fluid diffusion is induced by a gradient of pore pressure between the fault zone and the surrounding permeable crustal rocks. Fluid pressure variations can trigger earthquakes. This has been observed during gas extraction in the Valhall and Ekofisk oil fields in Norway [Zoback and Zinke, 2002], and during injection of fluid into reservoirs for geothermal energy purposes [Stark, 2003; Majer *et al.*, 2005] or for the subsurface geological storage of CO<sub>2</sub> [Streit and Hillis, 2004].

In the works of Santarelli *et al.* [1998], Segall and Fitzgerald [1998] and Khan and Teufel, [2000], the authors used a one-dimensional linear poro-elastic model to calculate the seepage forces. They used a geometry where an infinitely long production layer (fault zone) located at a finite depth is oriented parallel to the free surface. A consequence of this geometry is that the vertical stress remains constant, which is not the case when the fault has finite length and is oriented at an angle to the free surface. In addition, their results are strongly dependent on the boundary conditions used on the lateral walls (prescribed displacement or prescribed stress).



For example, such models predict that seepage forces are null when the stress is prescribed on the lateral boundaries.

In this paper, I calculate the seepage forces caused by two-dimensional pore-fluid diffusion from a fault zone into the surrounding permeable crustal rock. I relax the assumptions of infinite length and parallel orientation, and consider a preexisting fault zone with finite length and arbitrary orientation (Figure 1).

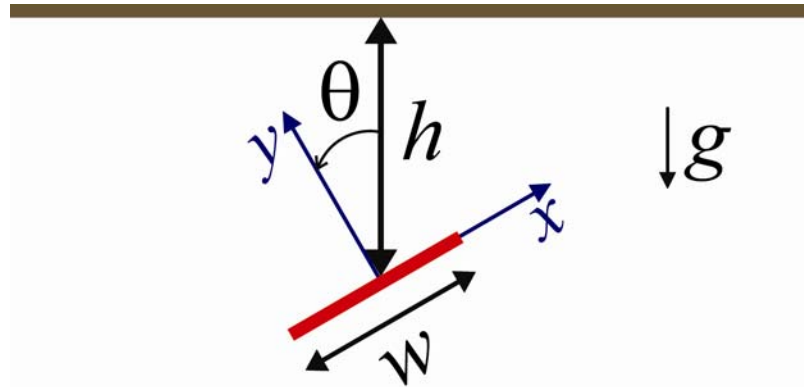


**Figure 1.** Preexisting fault with length  $w$  (red line) located at depth. The distance between the free surface (brown line) and the fault center is  $h$ . The origin of the Cartesian coordinate system coincides with the fault center. The  $y$ -axis is perpendicular to the fault and  $\theta$  is the angle between the vertical and the  $y$ -axis. In this configuration, the fluid overpressure  $\Delta p_f$  is prescribed locally in the fault plane. Diffusive fluid flow from the fault zone into the surrounding permeable rocks induces seepage forces that provide an additional control on fault reactivation.

The article is organized as follows: In the [second section](#), the projection of the tectonic stresses on the fault plane ( $\sigma_{ij}^T$ ) is calculated and the seepage forces  $\sigma_{ij}^S$  caused by fluid diffusion are calculated analytically (Figure 1). These calculations are based on the linear theory of poro-elasticity, the complex potential method and the conformal mapping. In the [third section](#), an analytical solution for the full stress tensor  $\sigma_{ij}$  is proposed, as a superposition of the tectonic and the seepage stresses, *i.e.*

$$\sigma_{ij} = \sigma_{ij}^T + \sigma_{ij}^S. \quad (8)$$

Finally, the full stress tensor is combined with the Coulomb failure criterion (6) to calculate the critical pore-fluid pressure required for failure triggering during extraction or injection of a fluid.

## 2. Seepage forces and analytical solution of the coupling between fluid flow and elastic deformation

The projection of the tectonic stress on the fault plane can be calculated using the coordinate system shown in [Figure 1](#). The origin is chosen at the center of the fault; and the  $y$ -axis is perpendicular to the fault plane. The fault is oriented at angle  $\theta$  to the vertical ([Figure 1](#)). The stress components on the fault plane are [[Turcotte and Schubert, 2002](#)]:

$$\begin{aligned}\sigma_{xx}^T &= \sigma_V^T + \frac{\Delta\sigma_H^T}{2} + \frac{\Delta\sigma_H^T}{2}\cos(2\theta), \\ \sigma_{xy}^T &= -\frac{\Delta\sigma_H^T}{2}\sin(2\theta),\end{aligned}\tag{9}$$

and

$$\sigma_{yy}^T = \sigma_V^T + \frac{\Delta\sigma_H^T}{2} - \frac{\Delta\sigma_H^T}{2}\cos(2\theta).$$

The seepage forces  $\sigma_{ij}^S$  are caused by the coupling between the diffusive pore fluid and the deformation of rock. The procedure for calculating these forces can be divided into six successive steps:

- 1) the definition of the system of equations for mechanical equilibrium;
- 2) the general solution of this system of equations in Cartesian coordinates using the complex potential method for poro-elasticity;
- 3) the calculation of the curvilinear coordinate system associated with the conformal mapping transformation, which allows finding the solution for complex geometry;
- 4) the calculation of the general solution of the equilibrium equations for steady-state poro-elasticity;
- 5) the defining of the boundary conditions; and finally
- 6) the calculation of the particular solution.

These six steps are detailed in the following sub-sections.

### 2.1 The system of equations for steady-state poro-elastic deformation

Following the common approach [Biot, 1941; Nikolaevski et al., 1970; Rice and Cleary, 1976], the three equations defining steady-state fluid filtration into a poro-elastic solid are:

i) The stress balance equation for the total stress tensor  $\sigma_{ij}^S$ , without volume forces:

$$\sum_j \frac{\partial}{\partial x_j} \sigma_{ij}^S = 0. \quad (10)$$

ii) The steady-state fluid filtration governed by the Laplace equation:

$$\sum_j \frac{\partial^2}{\partial x_j^2} P_f = 0, \quad (11)$$

where  $P_f$  is the fluid overpressure distribution ( $P_f = \Delta p_f$  on the fault zone and  $P_f = 0$  on the free surface).

iii) A poro-elastic constitutive relation between the total stress  $\sigma_{ij}^S$  and the strain  $\varepsilon_{ij}$  [Wang, 2000]:

$$\sigma_{ij}^S = 2G\varepsilon_{ij} + 2G\varepsilon_{kk} \frac{\nu}{1-2\nu} \delta_{ij} + \alpha p \delta_{ij}, \quad (12)$$

where  $\delta_{ij} = \begin{cases} 1 & \text{if } i = j \\ 0 & \text{if } i \neq j \end{cases}$  is the Kronecker delta; the strain tensor  $\varepsilon_{ij} = \frac{1}{2} \left( \frac{\partial u_i}{\partial x_j} + \frac{\partial u_j}{\partial x_i} \right)$  is defined

via displacements  $u_i$ ; the shear modulus  $G$ , the Poisson's ratio  $\nu$ , and the Biot-Willis poro-elastic constant  $\alpha$  correspond to the intrinsic material properties. The repeated indices denote summation. In equation (12) the sign convention is that compressive stress is positive. The gravitational acceleration does not appear in equations (10) and (11) because the gravitation effects are included in the preexisting tectonic stress (4-5) and the far-field pore pressure (2). Equation (11) implies that permeability is homogeneous and isotropic in the surrounding rocks outside the fault zone.

## 2.2 Complex potential method for steady-state poro-elasticity

Two-dimensional problems in elasticity can be solved using a complex potential method, developed by Kolosov [1909] and Muskhelishvili [1977], and generalized for thermo-elasticity by Lebedev [1937] and others. In this method, the general solution for the displacements and stresses is represented in terms of two analytic functions (potentials) of a complex variable and the temperature distribution [Goodier and Hodge, 1958; Timoshenko and Goodier, 1982]. This general solution automatically satisfies the force balance equation and the generalized Hooke's

law for thermo-elasticity. For a physically realistic solution, the temperature distribution must then satisfy the heat conduction equation. The nontrivial part of this method is in satisfying the boundary conditions of the specific problem. This is done using a conformal mapping transformation.

Since the equations for poro-elasticity and thermo-elasticity are identical for steady-state fluid filtration and heat flow problems, it is possible to use the complex potential method developed for thermo-elasticity, in order to solve steady-state poro-elastic problems.

According to this method, the general solution of equations (10), (11) and (12) can be written in the form [*Goodier and Hodge, 1958; Timoshenko and Goodier, 1982*]:

$$\sigma_{xx}^S + \sigma_{yy}^S = -4 \operatorname{Re}[\varphi'(z)] + 2\eta P_f(z, \bar{z}) \quad (13)$$

$$\sigma_{yy}^S - \sigma_{xx}^S + 2i\sigma_{xy}^S = -2[\bar{z}\varphi''(z) + \psi'(z)] + 2\eta \int \frac{\partial P_f(z, \bar{z})}{\partial z} d\bar{z} \quad (14)$$

$$2G(u_x + iu_y) = \chi\varphi(z) - \overline{z\varphi'(z)} - \overline{\psi(z)} + \eta \int P_f(z, \bar{z}) dz \quad (15)$$

where stresses are defined positive for compression. The integrals are indefinite without the integration constant and the superscript “ ‘ “ denotes differentiation, *i.e.*  $\varphi'(z) = \frac{\partial \varphi(z)}{\partial z}$ .

In equations (13-15),  $z = x + iy$  is the complex variable, with  $x$  and  $y$  the Cartesian coordinates,  $i = \sqrt{-1}$  is the imaginary unit and the bar denotes complex conjugation, *i.e.*  $\bar{z} = x - iy$ . Two dimensionless plane-strain parameters  $\eta$  and  $\chi$  complete the system:

$$\eta = \frac{\alpha}{2} \frac{1-2\nu}{1-\nu} \text{ and } \chi = 3-4\nu. \quad (16)$$

The complex potentials  $\varphi(z)$  and  $\psi(z)$  are analytic functions of  $z$ . They are derived from the biharmonic Airy function [*Muskhelishvili, 1977*].  $P_f(z, \bar{z})$  is the solution of Laplace equation (11), given as a function of two complex variables  $z$  and  $\bar{z}$ . By introducing the transformation of coordinates  $x = \frac{z + \bar{z}}{2}$  and  $y = \frac{z - \bar{z}}{2i}$ , the Laplace equation (11) can be rewritten in the form [*Timoshenko and Godier, 1982; Lavrent'ev and Shabat, 1972*]:

$$\frac{\partial^2}{\partial z \partial \bar{z}} P_f(z, \bar{z}) = 0. \quad (17)$$

The fluid filtration pressure creates seepage forces, and modifies the stresses at the boundaries of the solid. The boundary value problem, with given stresses or displacements on curvilinear boundaries, can be solved by calculating the complex potentials  $\varphi(z)$  and  $\psi(z)$  using Muskhelishvili's method [Muskhelishvili, 1977]. This method allows solving the steady-state plane strain or plane stress poro-elastic problems for nontrivial geometry and boundary conditions (Figure 2), by using a conformal mapping.

### 2.3 Conformal transformation and curvilinear coordinates

Conformal mapping is a transformation of coordinates that allows solving a problem in simple geometry (Figure 2a) and transforming the solution into a more complex geometry (Figure 2b). The properties of the conformal mapping transformation can be found in [Lavrent'ev and Shabat, 1972].

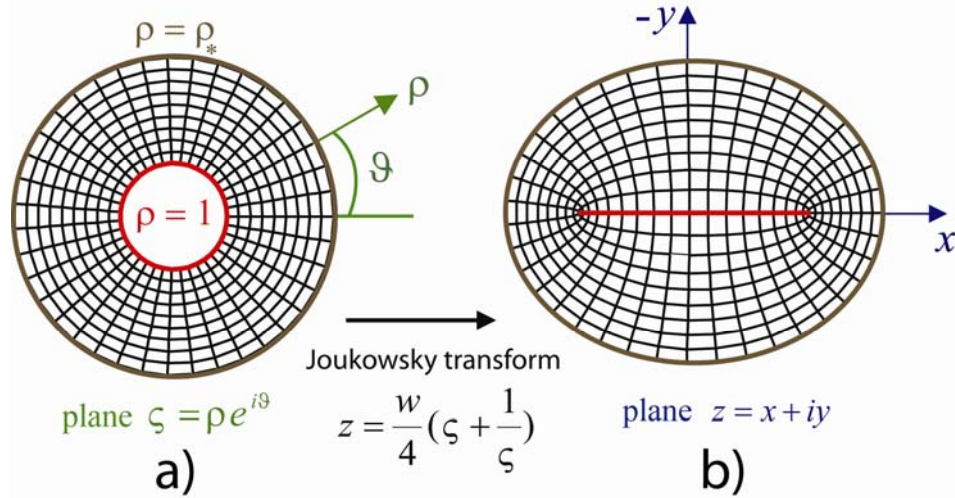


**Figure 2.** Conformal mapping procedure to solve the localized pore pressure increase effect. The circular geometry (a) is transformed into an elliptical geometry (b), representing the fault plane, using the Joukowski transformation. The fault segment (red line, similar to an infinitely thin ellipse) with curvilinear coordinates in the  $z$ -plane is represented as a circle (red) with cylindrical coordinates in the  $\zeta$ -plane.

The transformation of a circular domain into an elliptical one is given in a unique way by the Joukowski transform [Lavrent'ev and Shabat, 1972]:

$$z = \frac{w}{4} \left( \zeta + \frac{1}{\zeta} \right), \quad (18)$$

where  $w$  is the width of the pore-fluid pressure source as defined in Figure 1 (Figure 2b, red line). The complex variable  $\zeta$  is defined through its polar coordinates  $\rho$  and  $\vartheta$  (Figure 2a):

$$\zeta = \rho e^{i\vartheta}. \quad (19)$$

In [Figure 2a](#),  $1 \leq \rho \leq \rho_*$  and  $0 \leq \vartheta \leq 2\pi$ ; the internal ( $\rho = 1$ ) and external ( $\rho = \rho_*$ ) boundaries are shown by the red and brown curves, respectively.

The polar coordinates  $\rho$  and  $\vartheta$  in the  $\zeta$ -plane are used here as a non-dimensional system of coordinates for the  $z$ -plane. This polar coordinate system has the following properties: any circle with radius  $\rho = \text{const}$  and any straight line with an angle  $\vartheta = \text{const}$  on the  $\zeta$ -plane ([Figure 2a](#)) are transformed into an ellipse and a hyperbola in the  $z$ -plane, respectively ([Figure 2b](#)). The foci of the ellipse and the hyperbola on the  $z$ -plane coincide ([Figure 2b](#)). As the conformal mapping transformation preserves angles, the two lines  $\vartheta = \text{const}$  and  $\rho = \text{const}$ , initially perpendicular in the  $\zeta$ -plane, are also perpendicular in the  $z$ -plane. Therefore, the polar coordinates  $\rho$  and  $\vartheta$  can be considered as a curvilinear coordinate system in the  $z$ -plane.

The Cartesian and curvilinear coordinates on the  $z$ -plane are related through

$$\begin{aligned} x &= \frac{w}{4} \rho \left(1 + \frac{1}{\rho^2}\right) \cos(\vartheta) \\ \text{and} \\ y &= \frac{w}{4} \rho \left(1 - \frac{1}{\rho^2}\right) \sin(\vartheta). \end{aligned} \quad (20)$$

The Cartesian coordinates of the pore-pressure source ([Figure 2b](#), red line) are given by the transformation of the circle  $\rho = 1$  ([Figure 2a](#), red circle) into a line segment (*i. e.* an infinitely thin ellipse) through equation (20)

$$x = \frac{w}{2} \cos(\vartheta) \text{ and } y = 0. \quad (21)$$

The external boundary  $\rho = \rho_*$  is represented by a brown curve on [Figure 2a&b](#). If  $\rho_*^2 \gg 1$ , the relationships (20) become

$$\left. \begin{aligned} x &= \frac{w}{4} \rho_* \cos(\vartheta) + O\left(\frac{1}{\rho_*^2}\right) \\ y &= \frac{w}{4} \rho_* \sin(\vartheta) + O\left(\frac{1}{\rho_*^2}\right) \end{aligned} \right\} \text{ for } \rho = \rho_* \gg 1. \quad (22)$$

By neglecting the terms  $O\left(\frac{1}{\rho_*^2}\right)$  and taking  $\rho_* = \frac{4h}{w}$ , the relationship (22) can be simplified as

$$x = h \cos(\vartheta) \text{ and } y = h \sin(\vartheta). \quad (23)$$

These equations describe the external boundary, which is given by a circle with radius  $h$ . I derive the analytical solution for the case when  $(\frac{4h}{w})^2 \gg 1$  (Figure 2b, brown curve).

This case is met in some blind faults, for example at Puente Hills in California [Dolan *et al.*, 2003], or for the Tottori earthquake [Semmane *et al.*, 2005]. The geometry when  $(\frac{4h}{w})^2 \gg 1$  is met also in hydrocarbon industrial applications, where oil is extracted from a reservoir whose permeability has been enhanced artificially by hydraulic fracturing [Economides and Nolte, 2000]. In such reservoirs, cracks are produced by pumping a fluid at high pressure, inducing subsequent hydraulic fracturing. In order to keep the newly formed cracks open after decreasing the fluid pressure, sand is injected into them. It can be assumed that these fractures (filled with sand) represent fluid conduits in which the fracture mechanics is controlled by pore fluid diffusion. Thus the general mechanical description of these fractures and the fault zones are applicable.

#### 2.4 General solution of plane poro-elasticity in curvilinear coordinates

According to Muskhelishvili [1977], the stress and the displacement components in Cartesian and curvilinear coordinate systems are related by:

$$\sigma_{xx}^S + \sigma_{yy}^S = \sigma_{\rho\rho}^S + \sigma_{\vartheta\vartheta}^S, \quad (24)$$

$$\sigma_{yy}^S - \sigma_{xx}^S + 2i\sigma_{xy}^S = \frac{\rho^2}{\zeta^2} \frac{\overline{\omega'(\zeta)}}{\omega'(\zeta)} \left( \sigma_{\vartheta\vartheta}^S - \sigma_{\rho\rho}^S + 2i\sigma_{\rho\vartheta}^S \right), \quad (25)$$

and

$$u_x + iu_y = \frac{\rho}{\zeta} \frac{|\omega'(\zeta)|}{\omega'(\zeta)} (u_\rho + iu_\vartheta); \quad (26)$$

where

$$\omega(\zeta) = z = \frac{w}{4} \left( \zeta + \frac{1}{\zeta} \right). \quad (27)$$

Note that, if  $\rho = 1$  in equations (25) and (26), one obtains using (27):

$$\frac{\rho^2}{\zeta^2} \frac{\overline{\omega'(\zeta)}}{\omega'(\zeta)} = -1 \quad \text{and} \quad \frac{\rho}{\zeta} \frac{|\omega'(\zeta)|}{\omega'(\zeta)} = i \frac{\sqrt{\sin^2(\vartheta)}}{\sin(\vartheta)} = \begin{cases} i & \text{for } 0 < \vartheta < \pi \\ -i & \text{for } \pi < \vartheta < 2\pi \end{cases}. \quad (28)$$

The equations for stresses (13), (14) and displacements (15) in the curvilinear coordinate system become:

$$\sigma_{\rho\rho}^S + \sigma_{\theta\theta}^S = -4\operatorname{Re}(\Phi(\zeta)) + 2\eta P_f(\zeta, \bar{\zeta}), \quad (29)$$

$$\sigma_{\theta\theta}^S - \sigma_{\rho\rho}^S + 2i\sigma_{\rho\theta}^S = -\frac{\zeta^2}{\rho^2} \frac{2}{\omega'(\zeta)} \left[ \overline{\omega(\zeta)} \Phi'(\zeta) + \omega'(\zeta) \Psi(\zeta) \right] + \frac{\zeta^2}{\rho^2} \frac{2}{\omega'(\zeta)} \eta \int \frac{\partial P_f(\zeta, \bar{\zeta})}{\partial \zeta} \overline{\omega'(\zeta)} d\bar{\zeta},$$

and (30)

$$2G(u_\rho + iu_\theta) = \frac{\bar{\zeta}}{\rho} \frac{\overline{\omega'(\zeta)}}{|\omega'(\zeta)|} \left( \chi \varphi(\zeta) - \frac{\omega(\zeta)}{\omega'(\zeta)} \overline{\varphi'(\zeta)} - \overline{\psi(\zeta)} + \eta \int P_f(\zeta, \bar{\zeta}) \omega'(\zeta) d\zeta \right); \quad (31)$$

where

$$\Phi(\zeta) = \frac{\varphi'(\zeta)}{\omega'(\zeta)} \quad \text{and} \quad \Psi(\zeta) = \frac{\psi'(\zeta)}{\omega'(\zeta)}. \quad (32)$$

Using the properties of the conformal mapping transformation ( $\omega'(\zeta) \neq 0$  and  $\omega(\zeta) \neq 0$ ), the Laplace equation (17) becomes

$$\frac{\partial^2 P_f(\zeta, \bar{\zeta})}{\partial \zeta \partial \bar{\zeta}} = 0. \quad (33)$$

## 2.5 Boundary conditions

The boundary conditions for the fluid overpressure are:

$$\begin{aligned} & P_f = \Delta p_f \quad \text{for } \rho = 1 \\ \text{and} \quad & P_f = 0 \quad \text{for } \rho = \rho_*; \end{aligned} \quad (34)$$

and for the solid:

$$\begin{aligned} & \sigma_{xy}^S = 0 \quad \text{and} \quad u_y = 0 \quad \text{for } \rho = 1 \\ \text{and} \quad & \sigma_{\rho\theta}^S = 0 \quad \text{and} \quad \sigma_{\rho\rho}^S = 0 \quad \text{for } \rho = \rho_*. \end{aligned} \quad (35)$$

Note here that when  $\rho = 1$ , using (24-28), one obtains  $\sigma_{\rho\theta}^S = -\sigma_{xy}^S = 0$  and  $u_\rho = \pm u_y = 0$ . The boundary conditions on the fault zone ( $\rho = 1$ ) correspond to the elastic stage before slip onset and to a stage when the pore-fluid pressure is not high enough to open a tensile fracture. Thus the medium is continuous on the fault zone, and  $y = 0$  is a symmetry line. Therefore the boundary conditions on the fault zone ( $\rho = 1$ ) correspond to the boundary conditions on the



symmetry line (Figure 2b, red line). The external boundary ( $\rho = \rho_*$ ) corresponds to the free surface, which is free from the load (Figure 2b, brown line).

## 2.6 Analytical solution

Finally, the analytical solution derived using Muskhelishvili's method can be calculated. The full derivation is not presented here, since it is quite lengthy, but it can be demonstrated that the solution fulfills the boundary conditions.

The solution of the Laplace equation (33) with the boundary conditions (34) is given by

$$P_f(\zeta, \bar{\zeta}) = \Delta p_f \frac{\ln\left(\frac{\rho_*^2}{\zeta\bar{\zeta}}\right)}{\ln(\rho_*^2)}. \quad (36)$$

This equation can be simplified, using (18):

$$P_f(\rho) = \Delta p_f \frac{\ln\left(\frac{\rho_*}{\rho}\right)}{\ln(\rho_*)}. \quad (37)$$

The boundary conditions (34) are fulfilled by (37). The spatial distribution of the pore fluid overpressure around the fault zone is shown on Figure 3c (left).

The complex potentials, which define the solution of the problem, can be calculated:

$$\varphi(\zeta) = -\Delta p_f \eta w \frac{\zeta^2 + 1}{16\zeta} \left( 1 - \frac{1}{2\ln(\rho_*)} \right), \quad (38)$$

$$\psi(\zeta) = \frac{\Delta p_f \eta w}{8\zeta \ln(\rho_*)}. \quad (39)$$

The explicit expression for the components of the stress tensor can be found after substitution of (33), (38-39) into (28-29) using (31), and after simplifications:

$$\sigma_{\rho\rho}^s = -\eta \frac{\Delta p_f}{\ln(\rho_*)} \left( \ln\left(\frac{\rho}{\rho_*}\right) + 1 - \frac{(\rho^2 - 1)(\rho^2 - \cos(2\nu))}{1 - 2\rho^2 \cos(2\nu) + \rho^4} \right), \quad (40)$$

$$\sigma_{\nu\nu}^s = -\eta \frac{\Delta p_f}{\ln(\rho_*)} \left( \ln\left(\frac{\rho}{\rho_*}\right) + 1 + \frac{(\rho^2 + 1)(\cos(2\nu) - 1)}{1 - 2\rho^2 \cos(2\nu) + \rho^4} \right), \quad (41)$$

$$\sigma_{\rho\nu}^s = -\eta \frac{\Delta p_f}{\ln(\rho_*)} \frac{(\rho^2 - 1) \sin(2\nu)}{1 - 2\rho^2 \cos(2\nu) + \rho^4}. \quad (42)$$

Figure 3a shows the components of the seepage stress tensor in curvilinear coordinates.

The explicit expression for the displacements can be calculated after substitution of (36-37) and (39) into (30), using (25) and (31), and after simplifications:

$$u_x = -w \frac{\eta}{32} \frac{\Delta p_f \cos(\nu)}{G \ln(\rho_*)} \left[ \left( 2(\chi - 1) \ln(\rho_*) - \chi - 1 + 4 \ln(\rho) \right) \left( \rho + \frac{1}{\rho} \right) + \frac{8}{\rho} \right], \quad (43)$$

and

$$u_y = -w \frac{\eta}{32} \frac{\Delta p_f \sin(\nu)}{G \ln(\rho_*)} \left( 2(\chi - 1) \ln(\rho_*) - \chi - 1 + 4 \ln(\rho) \right) \left( \rho - \frac{1}{\rho} \right). \quad (44)$$

Figure 3c (center and left) shows the displacements in Cartesian coordinates. In equations (43-44), the analytical solution for the displacement in a Cartesian coordinate system is calculated. The solution in the curvilinear system is straightforward, but too long to be reproduced here. In order to get the relationships for the stress components in the Cartesian coordinate system, one should use (24-26) along with (40-42) (Figure 3b). The displacement in the curvilinear coordinate system can be found using (43-44) along with (26).

Applying the boundary conditions (35) to equations (42) and (43), one can show that the solution is fulfilled at the pore overpressure source  $\rho = 1$  (Figure 2, red curve). The non-zero stress components at the pore overpressure source are calculated using (40-41) along with (24-25) and (28):

$$\sigma_{yy}^S = \sigma_{\rho\rho}^S = \eta \Delta p_f - \frac{\eta \Delta p_f}{\ln(\rho_*)} \text{ for } \rho = 1 \quad (45)$$

and

$$\sigma_{xx}^S = \sigma_{\nu\nu}^S = \eta \Delta p_f \text{ for } \rho = 1 \quad (46)$$

At the external boundary  $\rho = \rho_*$  (Figure 2, brown curve),  $\sigma_{\rho\rho}^S = O\left(\frac{1}{\rho_*^2}\right)$  and  $\sigma_{\rho\nu}^S = O\left(\frac{1}{\rho_*^2}\right)$ ,

since  $\rho_* \gg 1$ . The boundary conditions (35) at  $\rho = \rho_*$  are also fulfilled.

The non-zero stress component at the free surface is given by:

$$\sigma_{\nu\nu}^S = -\eta \frac{\Delta p_f}{\ln(\rho_*)} + O\left(\frac{1}{\rho_*^2}\right) \quad \left( \sigma_{\nu\nu}^S = \sigma_{xx}^S \text{ for } \rho = \rho_* \text{ and } \vartheta = \frac{\pi}{2} \right). \quad (47)$$

The boundary conditions can be seen also in Figure 3.

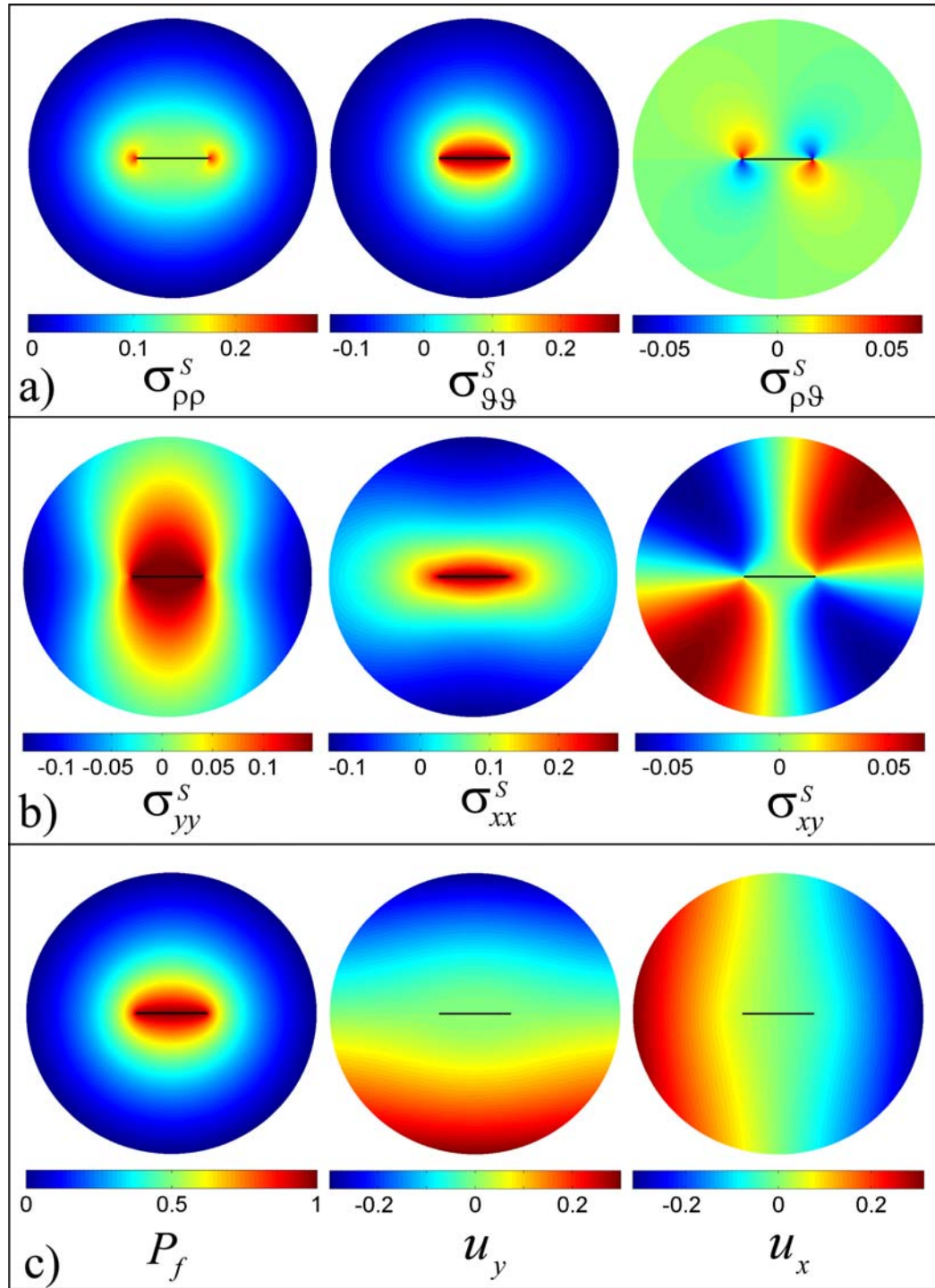


**Figure 3.** Effect of the coupling between pore-fluid diffusion and rock deformation. **a)** Curvilinear components of the seepage stress tensor; **b)** Cartesian components of the seepage stress tensor; **c)** fluid filtration overpressure and displacements along the  $y$  and  $x$  axes. The following parameters, representative of crustal rocks, were used in equations (37, 40-44) for creating these plots:  $\Delta p_f = 1$ ,  $G = 1$ ,  $\nu = 0.3$ ,  $\alpha = 1$  and  $\frac{h}{w} = 2$ .

Finally, this analytical solution (equations 40-44) has been checked against a finite element numerical method, specially developed for this purpose and the results are coinciding within of error  $O\left(\frac{1}{\rho_*^2}\right)$ .

### 3. Stress field on the fault and discussions

In this section, the critical pore-fluid pressure required for failure initiation is calculated. Using equation (9) for the tectonic stress on the fault zone along with equations (45-46) for the seepage forces, equation (8) for the full stress, and equations (1-2) for the fluid pressure on the fault zone  $p_f^i$  the following expressions for the stress deviator  $\tau$  and for the mean effective stress  $\sigma'_m$  can be calculated:

$$\tau = \frac{1}{2} \sqrt{\left(\Delta\sigma_H^T\right)^2 + \left(\frac{\eta\Delta p_f}{\ln\left(\frac{4h}{w}\right)}\right)^2 + 2\Delta\sigma_H^T \frac{\eta\Delta p_f}{\ln\left(\frac{4h}{w}\right)} \cos(2\theta)} \quad (48)$$

and

$$\sigma'_m = g h(\rho_r - \rho_w) + \frac{\Delta\sigma_H^T}{2} + \Delta p_f \left( \eta - 1 - \frac{\eta}{2 \ln\left(\frac{4h}{w}\right)} \right). \quad (49)$$

The way seepage forces influence the failure is shown on Figure 4. There  $ln$  is the Coulomb envelope given by equation (6) and  $lk$  is the tensile cut-off. The vertical and horizontal axes are the stress deviator and the mean effective stress, respectively. The dashed blue Mohr circle shows the stress state with zero pore-fluid overpressure. As the pore-fluid overpressure increases, the Mohr circle is translated to the left (green). Conversely, when the pore-fluid overpressure decreases, the Mohr circle is displaced to the right (red). In compliance with equation (48) the radius of the Mohr circle can increase (Figure 4a) or decrease (Figure 4b) during pore overpressure increase. The radius  $\tau$  of the Mohr circle increases (decreases) if the

parameter  $\left(\frac{\eta\Delta p_f}{\ln\left(\frac{4h}{w}\right)}\right)^2 + 2\Delta\sigma_H^T \frac{\eta\Delta p_f}{\ln\left(\frac{4h}{w}\right)} \cos(2\theta)$  is positive (negative). Note that, in the general

case, the change of the Mohr circle radius is not linearly proportional to the variation of pore fluid overpressure.

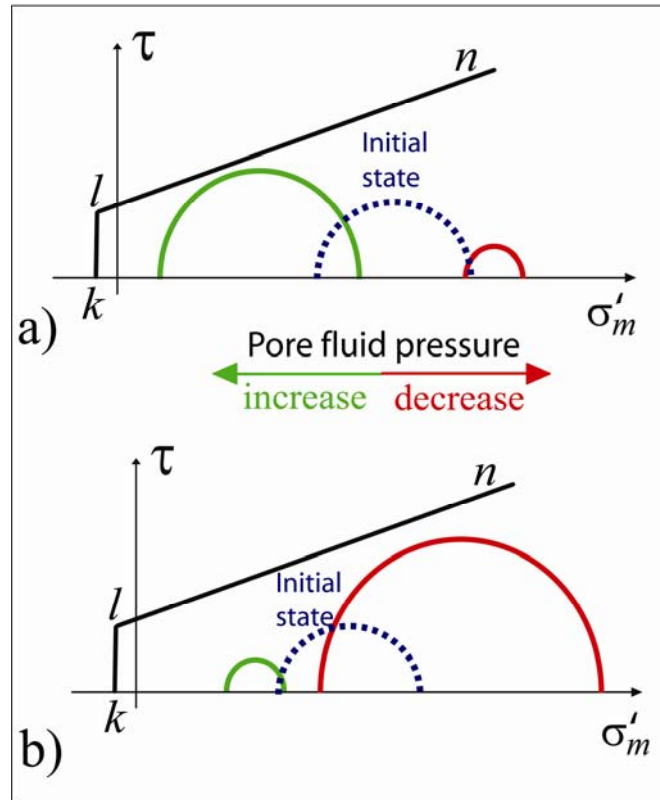


**Figure 4.** Effect of seepage forces on failure. Here  $ln$  is the Coulomb envelope,  $lk$  is the tensile cut-off,  $\tau$  is the stress deviator, and  $\sigma'_m$  is the mean effective stress. The dashed blue Mohr circle shows the stress-state with zero pore-fluid overpressure. The green Mohr circles represent the stress state when the pore-fluid overpressure has increased. The red Mohr circle shows the stress state with decreased pore-fluid overpressure. The radius of the Mohr circle can increase **a)** or decrease **b)** during pore overpressure increase, conversely to what happen when the seepage forces are not considered.

According to equations (48-49) and definition of  $\eta$  in (6), the seepage forces do not affect ( $\eta=0$ ) the failure on the fault if the surrounding rock is incompressible ( $\nu=\frac{1}{2}$ ) or if the coupling Biot-Willis constant is zero.

Failure occurs when the Mohr circle touches the failure envelope. According to **Figure 4b**, the Mohr circle can also touch the failure envelope even in the case of pore pressure decrease, which could explain earthquake triggering during oil/gas extraction from a reservoir. Using expressions for the stress deviator  $\tau$  and for the mean effective stress  $\sigma'_m$  (eqs. 48-49) I aim to

solve the failure criteria (6) in order to predict the pore fluid overpressure at failure onset. By making the substitutions defined in Table 1 for reasons of simplicity I obtain the failure condition (6) in the form:

$$\sqrt{m_1^2 + T^2 + Tm_2} = m_4 - Tm_3, \quad (50)$$

where the parameter  $T$  has to be calculated, as this is the only parameter depending on  $\Delta p_f$ .

After squaring and simplification equation (50), one obtains:

$$T^2 - T \frac{m_2 + 2m_4m_3}{m_3^2 - 1} - \frac{m_1^2 - m_4^2}{m_3^2 - 1} = 0. \quad (51)$$

The roots of this quadratic equation are the following:

$$T_{1,2} = \frac{1}{2} \frac{m_2 + 2m_4m_3}{m_3^2 - 1} \pm \frac{1}{2} \sqrt{\left( \frac{m_2 + 2m_4m_3}{m_3^2 - 1} \right)^2 + 4 \frac{m_1^2 - m_4^2}{m_3^2 - 1}}. \quad (52)$$

$m_1 = \Delta\sigma_H^T$	$m_2 = 2\Delta\sigma_H^T \cos(2\theta)$
$m_3 = \left( 2\left(\frac{1}{\eta} - 1\right) \ln\left(\frac{4h}{w}\right) + 1 \right) \sin(\phi)$	$m_4 = 2C \cos(\phi) + \left( 2g h(\rho_r - \rho_w) + \Delta\sigma_H^T \right) \sin(\phi)$
$T = \eta\Delta p_f / \ln\left(\frac{4h}{w}\right)$	

**Table 1.** Substitution of parameters in equations 50-52.

Using Table 1 one can see that  $\left( \frac{m_2 + 2m_4m_3}{m_3^2 - 1} \right)^2 + 4 \frac{m_1^2 - m_4^2}{m_3^2 - 1} \geq 0$ , thus  $T_1$  and  $T_2$  are both real roots of equation (51), however the equation (50) has only one root. Assuming that the fault geometry, tectonic stress and intrinsic rock properties are known, using Table 1, one can find which root satisfies the failure criteria (50):  $T_1$  or  $T_2$ . Then, the value of the critical pore-fluid overpressure at the onset of failure is calculated as

$$\Delta p_f = \frac{T}{\eta} \ln\left(\frac{4h}{w}\right). \quad (53)$$

Knowledge of this critical pore-fluid overpressure can prevent anthropogenic earthquakes that might occur during industrial exploitation of reservoirs.

#### 4. Conclusion

I have demonstrated that seepage forces caused by the coupling between fluid diffusion and the deformation of crustal rocks provide an additional control on fault reactivation. The model in the present study is based on linear poro-elasticity, with a fault of finite length. This model predicts the onset of hydraulic failure caused by depletion or increasing of pore-pressure in a fault zone. The critical pore-fluid pressure required for triggering slip on a preexisting fault is calculated. This model can be applied in several industrial problems (equations 52-53 and Table 1). For example: earthquake triggering by fluid extraction has been observed during the industrial exploitation of oil fields worldwide and during extraction of hydrothermal energy; this may also occur, during geological sequestration of carbon dioxides. In addition, because of the similarity between steady-state poro-elasticity and thermo-elasticity, this model can also be applied for solving thermo-elastic problems with a (quasi) steady-state thermal flux.

**Acknowledgments:** This work was financed by PGP (Physics of Geological Processes) a Center of Excellence at the University of Oslo. I would like to thank Galen Gisler and Francois Renard for helpful suggestions and Yuri Podladchikov for his continued support and encouragement.

#### References

- Biot, M. A., 1941. General theory of three-dimensional consolidation. *Journal of Applied Physics* 12, 155-164.
- Dolan, J.F., Christofferson, S. A., Shaw, J. H., 2003. Recognition of paleoearthquakes on the Puente Hills blind thrust fault, California. *Science* 300(5616), 115-118.
- Economides, M. J., Nolte, K. G., 2000. *Reservoir Stimulation*, 3rd Edition, John Wiley & Sons, New York. 856 pp.
- Goodier, J.N., Hodge, P.G., 1958. *Elasticity and Plasticity: The Mathematical Theory of Elasticity and The Mathematical Theory of Plasticity*, John Wiley & Sons, New York. 152 pp.
- Hickman, S., Sibson, R., Bruhn, R., 1995. Introduction to special section: Mechanical involvement of fluids in faulting. *Journal of Geophysical Research*, 100(B7), 12831-12840.

- Khan, M., Teufel, L.W., 2000. The effect of geological and geomechanical parameters on reservoir stress path and its importance in studying permeability anisotropy. *SPE Reserv. Evalu. Eng.* 3, 394–400.
- Kolosov, G. V. (1909). On the Application of the Theory of Functions of a Complex Variable to a Plane problem in the Mathematical Theory of Elasticity, Ph.D. diss., Dorpat University (in Russian).
- Lavrent'ev, M. A., Shabat, B. V., 1972. *Methods of Theory of Complex Variable Functions*. Nauka, Moscow. 736 pp..
- Lebedev, N. N., 1937. *Thermal Stresses in the Theory of Elasticity* [in Russian], ONTI, Moscow-Leningrad.
- Majer, E., Baria, R., Fehler, M., 2005. Cooperative research on induced seismicity associated with enhanced geothermal systems. *Geothermal Resources Council Transactions*, 29, GRC 2005 Annual Meeting, Sept. 25–28.
- Miller, S.A., Collettini, C., Chiaraluce, L., Cocco, M., Barchi, M., and Kaus, B.J.P., 2004. Aftershocks driven by a high-pressure  $CO_2$  source at depth. *Nature*, 427, 724-727.
- Muskhelishvili, N.I., 1977. *Some Basic Problems in the Mathematical Theory of Elasticity*. Springer, Berlin. 768 pp.
- Nikolaevski V.N., Basniev K.S., Gorbunov A.T., Zotov G.A., 1970. *Mechanics of Saturated Porous Media*. Nedra ,Moscow. 336 pp.
- Rice, J. R., 1992. Fault stress states, pore pressure distributions, and the weakness of the San Andreas fault, in *Faults Mechanics and Transport Properties of Rocks*, edited by B. Evans and T.-F. Wong, Academic, San Diego, California. 475-503.
- Rice, J. R., Cleary, M. P., 1976. Some basic stress-diffusion solutions for fluid-saturated elastic porous media with compressible constituents, *Reviews of Geophysics and Space Physics*, 14, 227-241.
- Rudnicki, J.W., 2001. Coupled deformation-diffusion effects in the mechanics of faulting and failure of geomaterials. *Applied Mechanics Review*, 54(6), 483-502.
- Santarelli, F.J., Tronvoll, J.T., Svennekjaer, M., Skeie, H., Henriksen, R., Bratli, R.K., 1998. Reservoir stress path: the depletion and the rebound. Society of Petroleum Engineers, SPE/ISRM No. 47350.



- Segall, P., 1985. Stress and subsidence resulting from subsurface fluid withdrawal in the epicentral region of the 1983 Coalinga earthquake. *Journal of Geophysical Research*. 90, 6801-6816.
- Segall, P., Fitzgerald, S., 1998. A note on induced stress changes in hydrocarbon and geothermal reservoirs. *Tectonophysics*, 289, 117-128.
- Semmane F, Campillo M, Cotton, F., 2005. The 2000 Tottori earthquake: A shallow earthquake with no surface rupture and slip properties controlled by depth, *Journal of Geophysical research*, 110 (B3): Art. No. B03306.
- Sibson, R. H., 1990. Conditions for fault-valve behaviour. R. J. Knipe and E. H. Rutter eds. In *Deformation Mechanisms, Rheology and Tectonics*, Geological Society London Special Publication 54, 15-28.
- Stark, M., 2003. Seismic evidence for a long-lived enhanced geothermal system (EGS) in the Northern Geysers Reservoir. *Geotherm. Resources Counc. Trans.*, 24, 24-27.
- Streit, E.E., Hillis, R. R., 2004. Estimating fault stability and sustainable fluid pressures for underground storage of CO<sub>2</sub> in porous rock. *Energy*, 29, 1445-1456.
- Timoshenko, S. P., Goodier, J.N., 1982. *Theory of Elasticity*. McGraw-Hill, New York. 608 pp.
- Turcotte, D. L., Schubert, G. 2002. *Geodynamics*. Cambridge University Press, Cambridge. 456 pp.
- Vermeer, P.A., de Borst, R., 1984. Non-associated plasticity for soils, concrete and rock. *Heron*, 29(3), 3-62.
- Wang, H.F., 2000. *Theory of Linear Poroelasticity with Applications to Geomechanics and Hydrology*. Princeton University Press, Princeton and Oxford. 276 pp.
- Zoback, M. D., Zinke, J. C., 2002. Production-induced Normal Faulting in the Valhall and Ekofisk Oil Fields. *Pure and Applied Geophysics*, 159, 403-420.

## **Paper III**

## Role of fluid diffusion on failure and effective stress of porous solids

A.Y. Rozhko and Y.Y. Podladchikov

Physics of Geological Processes (PGP), University of Oslo, P.O. Box 1048 Blindern, N-0316 Oslo, Norway

**Abstract.** In 1920 Griffith proposed a criterion for the propagation of a crack into a homogeneous elastic solid. However, many natural and industrial materials are porous and may contain fluid, which pressure modifies the state of stress. Here we demonstrate that when the pore-fluid pressure is not homogeneous, i.e. localized in and around a preexisting crack, the failure is controlled by a *modified effective stress law* that we calculate explicitly, extending the Griffith's theory and coupling it to the linear theory of poroelasticity.

There is a considerable volume of experimental work which indicates that the brittle failure of a fluid saturated porous medium is controlled by the Terzaghi's (conventional) effective stress rule [Terzaghi, 1943]:

$$\sigma_{ij}' = \sigma_{ij} + kp_f \delta_{ij}, \text{ with } k = 1 \quad (1)$$

Here  $\sigma_{ij}$  is the stress tensor;  $p_f$  is the fluid pressure;  $\delta_{ij} = \begin{cases} 1 & \text{if } i = j \\ 0 & \text{if } i \neq j \end{cases}$  is the

Kronecker delta. In equation (1) the sign convention is that compressive stress is negative. Most of the experiments have been performed using an external fluid-pressure source connected continuously to the pore system of the solid, with the aim of maintaining a constant pore-fluid pressure [Paterson and Wong, 2005]. In order to minimize experimental complications from incomplete saturation, the porous solid sample typically underwent a special preparation before deformation: air drying in vacuum oven and pre-saturation. A typical experimental problem is to attain a pore-fluid pressure equilibrium value throughout the sample when its permeability is low. Experimental values of  $k$  that differ from 1 have been reported in various types of porous rock and joints (for example, Boitnott and Scholtz [1990], Gandi and Carlson [1996], Patterson and Wong, [2005]). Typically the deviations from conventional effective stress rule ( $k \neq 1$ ) are attributed to experimental variability. For example,

Jaeger [1963] performed tensile failure tests on a fine-grained Tasmanian dolerite, and found that  $k = 0.95$ . He interpreted this discrepancy as an experimental artifact.

In the present study, we discuss how the inhomogeneity (non-equilibrium) of pore-fluid pressure may control brittle failure. We assume that the pore-fluid pressure perturbation is localized inside the permeable material. Many physical processes could generate a pore-fluid pressure perturbation inside a porous solid: incomplete saturation, hydration/dehydration reactions, or other internal fluid consumption or generation such as mechanical pumping and extraction.

We consider a 2D elliptical crack of length  $2a$  and negligible width ( $2b=0$ ) embedded into a permeable elastic body of radius  $c$ , as shown on Figure 1. Plane-strain deformation is assumed. The crack is filled with fluid at constant pressure  $p_c$ . The fluid pressure on the outer boundary of the body is  $p_\infty$ . Since the fluid pressure is not homogeneous in the body  $p_c \neq p_\infty$ , this leads to an additional stress field component due to the coupling between diffusive fluid and solid deformation.

To calculate the brittle tensile strength of this system, we use Griffith's theory [1920] and couple it to the linear theory of poroelasticity [Biot, 1941; Rice and Cleary, 1976; Wang, 2000]. The Griffith's theory states that the crack can propagate only if the sum of three energy terms is zero or negative:

1. the surface energy of the newly formed crack surface;
2. the change in the elastic strain energy of the body;
3. the change in the potential energy of the loading forces.

We apply the linear theory of poroelasticity, and assume both homogeneous and isotropic intrinsic properties of the porous material surrounding the crack. For simplicity reason, a steady-state fluid flow between the crack and the external surface of the body is considered. This flow is controlled by Laplace equation

$$\sum_j \frac{\partial^2 p_f}{\partial x_j^2} = 0 \quad (2)$$

where  $p_f$  is the fluid pressure distribution, with given values on the boundaries. The force balance equations for the total stress tensor  $\sigma_{ij}$ , without volume forces is governed by

$$\sum_j \frac{\partial \sigma_{ij}}{\partial x_j} = 0. \quad (3)$$

A constitutive relation between the total stress  $\sigma_{ij}$  and the strain  $\varepsilon_{ij}$  is given by

$$\sigma_{ij} = 2\mu\varepsilon_{ij} + 2\mu\varepsilon_{kk} \frac{\nu}{1-2\nu} \delta_{ij} - \alpha p, \quad (4)$$

where the repeated indices denote summation,  $\mu$  is the solid shear modulus,  $\nu$  ( $0 \leq \nu \leq \frac{1}{2}$ ) is the Poisson's ratio, and  $\alpha$  ( $0 \leq \alpha \leq 1$ ) is a coupling Biot-Willis poroelastic constant [[Wang, 2000](#); [Patterson and Wong, 2005](#)].

Finally, the relation between the strain  $\varepsilon_{ij}$  and the displacements  $u_i$  is

$$\varepsilon_{ij} = \frac{1}{2} \left( \frac{\partial u_i}{\partial x_j} + \frac{\partial u_j}{\partial x_i} \right). \quad (6)$$

The boundary conditions on the crack circumference for the fluid pressure and for the normal  $\sigma_{\rho\rho}$  and tangential  $\sigma_{\rho\vartheta}$  stresses are

$$\left. \begin{array}{l} p_f = p_c \\ \sigma_{\rho\rho} = -p_c \\ \sigma_{\rho\vartheta} = 0 \end{array} \right\} \text{on the crack,} \quad (7)$$

where  $\rho$  and  $\vartheta$  are curvilinear coordinates associated with the conformal mapping procedure (see [Auxiliary materials](#) for details).

The boundary conditions on the external boundary of the body are

$$\left. \begin{array}{l} p_f = p_\infty \\ \sigma_{\rho\rho} = \sigma_\infty \\ \sigma_{\rho\vartheta} = 0 \end{array} \right\} \begin{array}{l} \text{on the external} \\ \text{boundary} \end{array}. \quad (8)$$

We derived a closed form analytical solution for the equation system (2-6) and boundary conditions (7-8) ([Figure 1](#)) using the Muskhelishvili's complex potentials method [[Muskhelishvili, 1977](#); [Timoshenko and Godier, 1982](#)] and a conformal mapping procedure (see the complete demonstration in the [Auxiliary materials](#)).

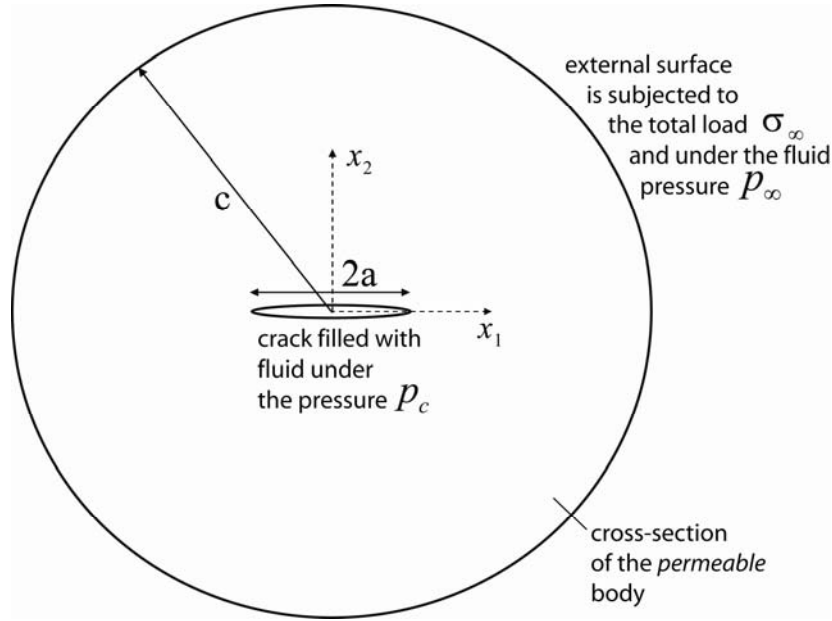


**Figure 1.** Model setup: An elliptical Griffith crack of length  $2a$  and width  $2b$  (not shown) contains a fluid under pressure  $p_c$  and is embedded into a permeable body of size  $2c$  ( $(\frac{2c}{a})^2 \gg 1$ ). A total load  $\sigma_\infty$  is applied perpendicularly to the external surface of the body. The fluid pressure on the external surface of the body is  $p_\infty$ .

Stresses and displacements near the tip of the slit-crack are of particular importance. Using the analytical solution [Auxiliary materials], we obtain the dominant terms of the stress along the extended crack line:

$$\sigma_{11}(x_1, 0) = (\sigma_\infty + Wp_\infty + (1-W)p_c) \sqrt{\frac{a}{2(x_1 - a)}}$$

For  $x_1 \geq a$ ,

$$\sigma_{22}(x_1, 0) = (\sigma_\infty + Wp_\infty + (1-W)p_c) \sqrt{\frac{a}{2(x_1 - a)}}, \quad (9)$$

$$\sigma_{12}(x_1, 0) = 0$$

and the dominant terms of the displacements along the crack sides:

$$u_1(x_1, 0^\pm) = a \frac{\chi + 1}{8\mu} \left( 2 \left( \frac{\chi - 1}{\chi + 1} - \eta \right) p_c + \frac{\eta(p_c - p_\infty)}{\ln \rho_*} \right)$$

For  $x_1 \leq a$ ,

$$u_2(x_1, 0^\pm) = \pm a \frac{\chi + 1}{4\mu} (\sigma_\infty + Wp_\infty + (1-W)p_c) \sqrt{-2(x_1 - a)/a} \quad (10)$$

where the sign “ $\pm$ ” denotes the displacements on the upper “+” and lower “-” edges of the crack tip.

In equations (9) and (10) the parameters  $\eta$  and  $\chi$  are given by

$$\begin{aligned} \text{Plane strain: } \chi &= 3 - 4\nu \text{ and } \eta = \frac{\alpha}{2} \frac{1 - 2\nu}{1 - \nu}, \\ \text{Plane stress: } \chi &= \frac{3 - \nu}{1 + \nu} \text{ and } \eta = \frac{\alpha}{2} (1 - \nu) \end{aligned} \quad (11)$$

and  $W$  is a “weight” parameter calculated as:

$$W = \eta \left( 1 - \frac{1}{\ln \frac{2c}{a}} \right). \quad (12)$$

The Griffith energy criterion can be represented equivalently via the path-independent  $J$ -integral [[Rice, 1968](#); [Hellan, 1984](#)]:

$$2\gamma \leq J, \quad (13)$$

where  $2\gamma$  is the specific surface energy, assigned to one side of the fracture surface; and the path-independent  $J$ -integral is defined as:

$$J = \int_{\Gamma} [U dx_2 - \vec{T} \cdot \frac{\partial \vec{u}}{\partial x_1} ds] \quad (14)$$

Here  $U$  is the strain energy density function, defined as [[Atkinson and Craster, 1991](#); [Wang, 2000](#)]:

$$U = \frac{1}{2} \sigma_{ij} \varepsilon_{ij} + p_f \zeta, \quad (15)$$

where  $\zeta$  is the variation of fluid content per unit reference volume.

In equation (14) the integral is taken along any path  $\Gamma$  (counter-clockwise) around the crack tip;  $T_i$  is the vector of traction on  $\Gamma$ , i.e.  $T_i = \sigma_{ij} n_j$ ,  $n_j$  is the normal to the curve  $\Gamma$ ;  $s$  is the arc length along  $\Gamma$ . Since a path of integration can be arbitrary chosen in the poroelastic regime, we take the curve  $\Gamma$  from the lower side ( $x_1 = a$ ,  $x_2 = 0^-$ ), past ( $x_1 = a + \Delta a$ ,  $x_2 = 0$ ), to the upper side at ( $x_1 = a$ ,  $x_2 = 0^+$ ). Since here  $dx_2 = 0$ , equation (14) becomes [[Rice, 1968](#); [Hellan, 1984](#)]:

$$J = \lim_{\Delta a \rightarrow 0} \frac{1}{2\Delta a} \int_a^{a+\Delta a} \sigma_{2i}(x_1, 0, a) [u_i(x_1, 0^+, a + \Delta a) - u_i(x_1, 0^-, a + \Delta a)] dx_1 \quad (16)$$

where  $\sigma_{2i}(x_1, 0, a)$  is the stress field given by equations (9). In the limit  $\Delta a = 0$ , there is a translation of the displacement fields at the crack front such that  $u_i(x_1, 0^\pm, a + \Delta a)$  will be the displacement components according to (10) when  $-(x_1 - a)$  is replaced by  $\Delta a - (x_1 - a)$  [[Hellan, 1984](#)]. This leads to

$$\begin{aligned}
J &= a \frac{\chi+1}{4\mu} (\sigma_\infty + Wp_\infty + (1-W)p_c)^2 \lim_{\Delta a \rightarrow 0} \frac{1}{2\Delta a} \int_0^{\Delta a} 2 \sqrt{\frac{\Delta a - (x_1 - a)}{(x_1 - a)}} dx_1 \\
&= \pi a \frac{\chi+1}{8\mu} (\sigma_\infty + Wp_\infty + (1-W)p_c)^2
\end{aligned} \tag{17}$$

Using (13,17), the failure criteria is obtained in the form

$$\sigma_\infty + Wp_\infty + (1-W)p_c \geq 4 \sqrt{\frac{\gamma\mu}{\pi a(\chi+1)}}. \tag{18}$$

Considering plain-strain and using (11) and (12), we receive the expression for the “weight” parameter:

$$W = \frac{\alpha}{2} \frac{1-2\nu}{1-\nu} \left(1 - \frac{1}{\ln \frac{2c}{a}}\right). \tag{19}$$

Here  $0 \leq W \leq \frac{1}{2}$ ; the case  $W = \frac{1}{2}$  being an extremum that occurs when  $\nu = 0$ ,  $\alpha = 1$  and  $\frac{2c}{a} \rightarrow \infty$ , which is never realized practically for real materials.

In the case when the fluid pressure on the crack equals the macroscopic pore pressure ( $p_c = p_\infty$ ) one gets from (18) the failure criteria:

$$\sigma_\infty + p_\infty \geq 4 \sqrt{\frac{\gamma\mu}{\pi a(\chi+1)}} \tag{20}$$

Equation (20) coincides with result derived by Murrell [1964] for the case when the fluid pressure is homogeneous ( $p_c = p_\infty$ ).

Thus, equation (18) suggests that the failure is controlled both by the microscopic fluid pressure  $p_c$  and the macroscopic fluid pressure  $p_\infty$ . The microscopic fluid pressure has a larger impact on failure because  $1-W \geq \frac{1}{2}$ . In the case of incomplete saturation, the fluid pressure in the crack is null, i.e.  $p_c = 0$ , and equation (20) becomes:

$$\sigma_\infty + Wp_\infty \geq 4 \sqrt{\frac{\gamma\mu}{\pi a(\chi+1)}}. \tag{21}$$

The assumption that the ellipsoidal crack width is null ( $2b = 0$ ) implies that the radius of the curvature at the crack tip is zero ( $= b^2 / a$ ). According to equation (9), the maximum stress at the crack tip ( $x_1 = a$ ) is infinite. However, for a real crack the



radius of the curvature cannot be smaller than atomic or molecular dimension [e.g., Orowan, 1949] and the crack surfaces must be slightly separated to prevent surface forces from closing the crack [Elliot, 1947; Murrel, 1964]. Thus, another approach to the tensile failure problem is to calculate the maximum tensile stress at the tip of an elliptical crack with finite width  $b$  [Griffith, 1924; Murrel, 1964]. The analytical solution [Auxiliary materials] gives the following expression for the maximum tensile stress at the crack tip

$$\sigma_{g,g}^{\max} = 2(\sigma_{\infty} + Wp_{\infty} + (1-W)p_c) \frac{a}{b} - p_c - \frac{(p_c - p_{\infty})\eta}{\ln(\rho_*)}. \quad (22)$$

If the crack length is much larger than the crack width  $a \gg b$ , equation (22) can be simplified as

$$\sigma_{g,g}^{\max} \approx 2(\sigma_{\infty} + Wp_{\infty} + (1-W)p_c) \frac{a}{b}. \quad (23)$$

According to the local failure criterion, failure occurs if  $\sigma_{g,g}^{\max} \geq \sigma_T$  where  $\sigma_T$  is the ultimate tensile strength equal to the stress needed to break atomic bonds of an ideal brittle material. A typical value for  $\sigma_T$  is about one tenth of the solid Young's modulus ( $E/10$ ). By substitution of the maximum tensile stress (23) into the local failure criterion we obtain the failure criterion:

$$\sigma_{\infty} + Wp_{\infty} + (1-W)p_c \geq \frac{2b}{a} \sigma_T. \quad (24)$$

We examined two failure mechanisms: the *Griffith's energy criterion* (18) and the *local failure criterion* (24). Calculations show the same expression for the *effective stress*.

**Conclusions.** Using both Griffith's energy criterion and local failure criterion we demonstrated that the failure of a fluid-saturated porous solid is controlled both by the microscopic pressure in the crack and by the macroscopic pressure (equations 18 and 19 or 19 and 24). This can explain several experimental deviations from the *conventional effective stress law*. The results of this work have direct implications in the systems in which the pore-fluid pressure is not homogeneous due to incomplete saturation or due to the internal or external fluid pressure perturbations.

**Acknowledgments:** This work was financed by PGP (Physics of Geological Processes), a Center of Excellence at the University of Oslo.

## References

- Atkinson, C., Craster R.V., 1991. Plane strain fracture in Poroelastic Media. Proceedings: Mathematical and Physical Sciences, 434(1892), 605-633.
- Boitnott, G. N., Scholz C.H., 1990. Direct measurement of the effective pressure law: deformation of joints, subjected to pore and confining pressures. Journal of Geophysical Research, 95, 19279-19298.
- Biot, M. A., 1941. General theory of three-dimensional consolidation. Journal of Applied Physics 12, 155-164.
- Elliott, H. A., 1947. An analysis of the conditions for rupture due to Griffith cracks. Proc. Phys. Soc. London, 59, 208-223.
- Gangi, A. F., Carlson, R. L., 1996. An asperity-deformation model for effective pressure. Tectonophysics, 256, 241-252.
- Griffith, A. A., 1920. The Phenomena of Rupture and Flow in Solids, Phil. Trans. Roy. Soc., London, A, 221, 163-198.
- Griffith, A. A., 1924. The Theory of Rupture, Proceedings of the First International Congress for Applied Mechanics, 55-63.
- Jaeger, J. C., 1963, Extension failures in rocks subjected to the fluid pressure. Journal of geophysical research, 68, 6066-6067.
- Jaeger, J. C., and N. G. W. Cook (1979), *Fundamentals of Rock Mechanics*, 593 pp., Chapman and Hall, London.
- Hellan, K., 1984. Introduction to fracture mechanics. McGraw-Hill, Inc., New York. 302 pp.
- Murrell, S. A. F. (1964), The theory of propagation of elliptical Griffith cracks under various conditions of plane strain or plain stress, British Journal of Applied Physics, 15, 1195-1223.
- Muskhelishvili, N. I., 1977. Some Basic Problems in the Mathematical Theory of Elasticity. Springer, Berlin. 768 pp.
- Orowan, E., 1949. Fracture and strength of solids. Reports on Progress Physics, 12, 185-232.
- Paterson, M. S., and Wong, T.-F., 2005. Experimental rock deformation-the brittle field. Springer, Berlin. 346 pp.

- Rice, J., 1968. Mathematical analysis in the mechanics of fracture. In Liebowitz, H., editor, *Fracture - An advanced treatise*, volume 2, pages 191–311. Pergamon Press, Oxford.
- Rice, J. R., Cleary, M. P., 1976. Some basic stress-diffusion solutions for fluid-saturated elastic porous media with compressible constituents, *Reviews of Geophysics and Space Physics*, 14, 227-241.
- Terzaghi, K., 1943. *Theoretical Soil Mechanics*, John Wiley and Sons, New York. 528 pp.
- Timoshenko, S. P., Goodier, J.N., 1982. *Theory of Elasticity*. McGraw-Hill, New York. 608 pp.
- Wang, H.F., 2000. *Theory of Linear Poroelasticity with Applications to Geomechanics and Hydrology*. Princeton University Press, Princeton and Oxford. 276 pp.

## Auxiliary Materials

### Role of fluid diffusion on failure and effective stress of porous solids

A.Y. Rozhko and Y.Y. Podladchikov

Physics of Geological Processes (PGP), University of Oslo, P.O. Box 1048 Blindern, N-0316 Oslo, Norway

In this auxiliary material we obtain the analytical solution for the problem presented on [Figure 1](#) of the paper. The procedure of derivation of the analytical solution is divided into six successive steps described in the following subsections:

- 1) the definition of the system of equations for mechanical equilibrium;
- 2) the general solution of this system of equations in Cartesian coordinates using the complex potential method for poro-elasticity;
- 3) the introduction of the curvilinear coordinate system associated with the conformal mapping, which allows finding the solution for the complex crack geometry;
- 4) the calculation of the general solution of the equilibrium equations for steady-state poro-elasticity in curvilinear coordinate system;
- 5, 6) finally, after defining the boundary conditions, the calculation of the particular solution.

#### A 1 System of equations for steady-state poro-elastic deformation

Following the common approach [[Biot, 1941](#); [Rice and Cleary, 1976](#); [Wang, 2000](#)], the equations for steady-state fluid filtration in a poro-elastic solid are given by:

- The stress balance equations for the total stress tensor  $\sigma_{ij}$ , without volume forces:

$$\sum_j \frac{\partial \sigma_{ij}}{\partial x_j} = 0 \quad (\text{A1})$$

- The steady-state fluid filtration governed by the Laplace equation for fluid pressure distribution  $p_f$ :

$$\sum_j \frac{\partial^2 p_f}{\partial x_j^2} = 0 \quad (\text{A2})$$

- A constitutive elastic relationship between the total stress  $\sigma_{ij}$  and the strain  $\varepsilon_{ij}$ :

$$\sigma_{ij} = 2\mu\varepsilon_{ij} + 2\mu\varepsilon_{kk} \frac{\nu}{1-2\nu} \delta_{ij} - \alpha p_f \quad (\text{A3})$$

where  $\delta_{ij}$  is the Kronecker delta and the intrinsic material properties are the shear modulus  $G$ , the drained Poisson's ratio  $\nu$ , and the Biot-Willis poroelastic constant  $\alpha$  [Paterson and Wong, 2005].

## A 2 Complex Potential Method for steady-state poro-elasticity

Two-dimensional problems in elasticity can be solved using a complex potential method (CPM), developed by Kolosov [1909] and Muskhelishvili [1977]. This method has been generalized for thermo-elasticity by Lebedev [1937]. In this method, the general solution for the displacements and stresses is represented in terms of three functions: two complex potentials and the temperature distribution [Goodier and Hodge, 1958; Timoshenko and Goodier, 1982]. This general solution automatically satisfies the force balance equation and generalized Hooke's law for thermo-elasticity, provided that the function describing the temperature distribution satisfies also the heat conduction equation. The nontrivial part of this method is in satisfying the boundary conditions of the specific problem, which is done by conformal mapping.

The equations for poro-elasticity and thermo-elasticity are identical for steady-state fluid filtration and heat flow problems. Therefore, it is possible to use the complex potential method, developed for thermo-elasticity to solve steady-state poro-elastic problems.

According to the CPM, the general solution of equations (A1-A3) can be written in the form (by convention, compressive stress and strain are positive) [Goodier and Hodge, 1958; Timoshenko and Goodier, 1982; Muskhelishvili, 1977]:

$$\sigma_{11} + \sigma_{22} = 4 \operatorname{Re}[\varphi'(z)] - 2\eta p_f(z, \bar{z}) \quad (\text{A4})$$

$$\sigma_{22} - \sigma_{11} + 2i\sigma_{12} = 2[\bar{z}\varphi''(z) + \psi'(z)] - 2\eta \int \frac{\partial p_f(z, \bar{z})}{\partial z} d\bar{z} \quad (\text{A5})$$

$$2\mu(u_1 + iu_2) = \chi\varphi(z) - z\overline{\varphi'(z)} - \overline{\psi(z)} + \eta \int p_f(z, \bar{z}) dz \quad (\text{A6})$$

Where the parameters  $\eta$  and  $\chi$  are defined as:

$$\begin{aligned}
\text{Plane strain: } \chi &= 3-4\nu \text{ and } \eta = \frac{\alpha}{2} \frac{1-2\nu}{1-\nu} \\
\text{Plane stress: } \chi &= \frac{3-\nu}{1+\nu} \text{ and } \eta = \frac{\alpha}{2} (1-\nu)
\end{aligned}
\tag{A7}$$

The integrals in Equations A5-A6 are indefinite (without the integration constant) and the superscript “ ’ ” denotes differentiation, i.e.  $\varphi'(z) = \frac{\partial \varphi(z)}{\partial z}$ .

In equations (A4-A6),  $z = x_1 + ix_2$  is the complex variable,  $x_1$  and  $x_2$  are the usual Cartesian coordinates,  $i = \sqrt{-1}$  is the imaginary unit, and the bar denotes complex conjugation, i.e.  $\bar{z} = x_1 - ix_2$ .  $\varphi(z)$  and  $\psi(z)$  are the complex potentials, which are analytic functions of the complex variable  $z$ , and are derived from the biharmonic Airy function [Muskhelishvili, 1977].  $p^f(z, \bar{z})$  is the solution of Laplace equation (A2), given as a function of two complex variables  $z$  and  $\bar{z}$ . By introducing the transformation of coordinates  $x_1 = \frac{z + \bar{z}}{2}$  and  $x_2 = \frac{z - \bar{z}}{2i}$ , the Laplace equation (A2) can be rewritten in the form [Timoshenko and Godier, 1982; Lavrent'ev and Shabat, 1972]:

$$\frac{\partial^2}{\partial z \partial \bar{z}} p_f(z, \bar{z}) = 0.
\tag{A8}$$

The fluid filtration pressure creates stresses at the boundaries of the solid. The boundary value problem with given stresses or displacements in curvilinear boundaries can be solved by finding the complex potentials  $\varphi(z)$  and  $\psi(z)$  using Muskhelishvili's method.

### A 3 Conformal transformation and curvilinear coordinates

Conformal mapping is a transformation of coordinates that allow solving a problem with a simple geometry (Figure A1a) and transforming its solution for a more complex geometry (Figure A1b). The properties of conformal mapping can be found in [Lavrent'ev and Shabat, 1972].

The transformation of a circular domain into an elliptical one is given in a unique way by the generalized Joukowski transform:

$$z = R\left(\zeta + \frac{m}{\zeta}\right)
\tag{A9}$$

here  $R > 0$  is a constant and has a dimension of length;  $m$  ( $0 \leq m \leq 1$ ) is a non-dimensional constant. The complex variable  $\zeta$  is defined in a non-dimensional polar coordinates  $\rho$  and  $\vartheta$  as follows (Figure A1a):

$$\zeta = \rho e^{i\vartheta}. \quad (\text{A10})$$

where  $1 \leq \rho \leq \rho_*$  and  $0 \leq \vartheta \leq 2\pi$ ; the internal ( $\rho = 1$ ) and external ( $\rho = \rho_*$ ) boundaries are shown by the red and brown curves, respectively on Figure A1a.

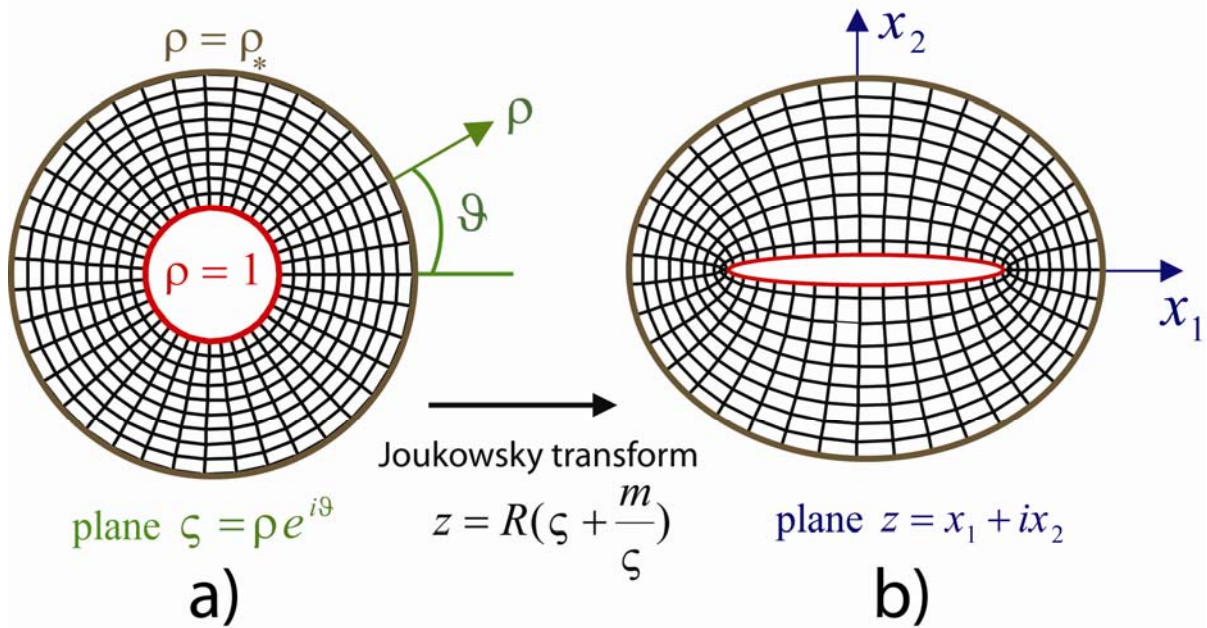


**Figure A1.** Conformal mapping procedure and systems of Cartesian and curvilinear coordinates.

We use the polar coordinates  $\rho$  and  $\vartheta$  in the  $\zeta$ -plane, as a non-dimensional system of coordinates for the  $z$ -plane. The properties of this coordinate system are considered below. Any circle  $\rho = \text{const}$  and radius  $\vartheta = \text{const}$  in the  $\zeta$ -plane (Figure A1a) are transformed into an ellipse and a hyperbola in the  $z$ -plane, respectively (Figure A1b). The foci of the ellipse and the hyperbola on the  $z$ -plane coincide (Figure A1b). As the conformal mapping preserves angles, the two lines  $\vartheta = \text{const}$  and  $\rho = \text{const}$  are perpendicular in the  $z$ -plane. Therefore, the polar coordinates  $\rho$  and  $\vartheta$  can be considered as a curvilinear coordinate system in the  $z$ -plane. The Cartesian and curvilinear coordinates on the  $z$ -plane are related through:

$$\begin{aligned}
x_1 &= R\rho\left(1 + \frac{m}{\rho^2}\right)\cos(\mathcal{G}) \\
x_2 &= R\rho\left(1 - \frac{m}{\rho^2}\right)\sin(\mathcal{G})
\end{aligned} \tag{A11}$$

If  $\rho = 1$  equations (A10) become:

$$\begin{aligned}
x_1 &= R(1+m)\cos(\mathcal{G}) \\
x_2 &= R(1-m)\sin(\mathcal{G})
\end{aligned} \tag{A12}$$

One can see that the equations (A11) are parametric equations for ellipse with semiaxis:  $R(1+m)$  and  $R(1-m)$ .

The external boundaries  $\rho = \rho_*$  are represented as brown curves on Figure A1. If  $\rho_*^2 \gg 1$ , the relations (A10) become:

$$\begin{aligned}
x_1 &= R\rho_* \cos(\mathcal{G}) + O\left(\frac{1}{\rho_*^2}\right) \\
x_2 &= R\rho_* \sin(\mathcal{G}) + O\left(\frac{1}{\rho_*^2}\right)
\end{aligned} \quad \text{for } \rho_*^2 \gg 1 \tag{A13}$$

Neglecting the terms of order  $O\left(\frac{1}{\rho_*^2}\right)$  the equations (A12) become parametric for circle with the radius  $R\rho_*$ .

Then, if the crack has a width equal to zero ( $m=1$ ) and a length equal to  $2a$ , one can find from (A12, A13) that  $R = \frac{a}{2}$  and  $\rho_* = \frac{2c}{a}$ , where  $c$  is defined on Figure 1. We derive below

the analytical solution for the case when  $\left(\frac{2c}{a}\right)^2 \gg 1$ , so that the external boundary may be considered as circular.

#### A 4 General solution of plane poro-elasticity in curvilinear coordinates

According to Muskhelishvili [1977], the stress and the displacement components in the Cartesian and Curvilinear coordinate systems are related by:

$$\sigma_{11} + \sigma_{22} = \sigma_{\rho\rho} + \sigma_{\mathcal{G}\mathcal{G}}, \tag{A14}$$



$$\sigma_{22} - \sigma_{11} + 2i\sigma_{12} = \frac{\rho^2}{\zeta^2} \frac{\overline{\omega'(\zeta)}}{\omega'(\zeta)} \left( \sigma_{g,g} - \sigma_{\rho,\rho} + 2i\sigma_{\rho,g} \right), \quad (\text{A15})$$

and

$$u_1 + iu_2 = \frac{\rho}{\bar{\zeta}} \frac{|\omega'(\zeta)|}{\omega'(\zeta)} (u_\rho + iu_g); \quad (\text{A16})$$

where

$$\omega(\zeta) = z = R\left(\zeta + \frac{m}{\zeta}\right). \quad (\text{A17})$$

The equations for stresses (A4-A5) and displacements (A6) in the curvilinear coordinate system become:

$$\sigma_{\rho\rho} + \sigma_{g,g} = 4\text{Re}(\Phi(\zeta)) - 2\eta p_f(\zeta, \bar{\zeta}), \quad (\text{A18})$$

$$\sigma_{g,g} - \sigma_{\rho\rho} + 2i\sigma_{\rho,g} = \frac{\zeta^2}{\rho^2} \frac{2}{\omega'(\zeta)} \left[ \overline{\omega(\zeta)} \Phi'(\zeta) + \omega'(\zeta) \Psi(\zeta) \right] - \frac{\zeta^2}{\rho^2} \frac{2}{\omega'(\zeta)} \eta \int \frac{\partial p_f(\zeta, \bar{\zeta})}{\partial \zeta} \overline{\omega'(\zeta)} d\bar{\zeta},$$

and (A19)

$$2\mu(u_\rho + iu_g) = \frac{\bar{\zeta}}{\rho} \frac{\overline{\omega'(\zeta)}}{|\omega'(\zeta)|} \left( \chi\varphi(\zeta) - \frac{\omega(\zeta)}{\omega'(\zeta)} \overline{\varphi'(\zeta)} - \overline{\psi(\zeta)} + \eta \int p_f(\zeta, \bar{\zeta}) \omega'(\zeta) d\zeta \right), \quad (\text{A20})$$

where

$$\Phi(\zeta) = \frac{\varphi'(\zeta)}{\omega'(\zeta)} \quad \text{and} \quad \Psi(\zeta) = \frac{\psi'(\zeta)}{\omega'(\zeta)}. \quad (\text{A21})$$

Using the properties of conformal mapping ( $\omega'(\zeta) \neq 0$  and  $\omega(\zeta) \neq 0$ ), the Laplace equation (A8) becomes:

$$\frac{\partial^2}{\partial \zeta \partial \bar{\zeta}} p_f(\zeta, \bar{\zeta}) = 0. \quad (\text{A22})$$

## A 5 Boundary conditions

The boundary conditions for the fluid are:

$$\begin{aligned} p_f &= p_c \quad \text{for } \rho = 1 \\ p_f &= p_\infty \quad \text{for } \rho = \rho_* \end{aligned} \quad (\text{A24})$$

and the boundary conditions for the solid are:

$$\begin{aligned}\sigma_{\rho\rho} &= -p_c \quad \& \quad \sigma_{\rho\theta} = 0 \quad \text{for } \rho = 1 \\ \sigma_{\rho\rho} &= \sigma_\infty \quad \& \quad \sigma_{\rho\theta} = 0 \quad \text{for } \rho = \rho_*\end{aligned}\tag{A25}$$

## A 6 Solution

We finally present the analytical solution derived by using Muskhelishvili's method. We do not show the derivation here, since it is quite lengthy, but we demonstrate that our solution fulfills the boundary conditions.

The solution of Laplace equation (A23) with the boundary conditions (A24) is given by

$$p_f(\zeta, \bar{\zeta}) = p_c - (p_c - p_\infty) \frac{\ln(\zeta \bar{\zeta})}{\ln(\rho_*^2)}.\tag{A26}$$

This equation can be simplified, using (eq. A10) as follows

$$p_f(\rho) = p_c - (p_c - p_\infty) \frac{\ln(\rho)}{\ln(\rho_*)}.\tag{A27}$$

The boundary conditions (A24) are fulfilled by (eq. A27). Equation (A27) gives the solution for pore fluid pressure.

We calculate the complex potentials, which define the solution of problem as following:

$$\varphi(\zeta) = R \frac{\eta p_c \zeta^2 + m}{2\zeta \ln(\rho_*)} + R \frac{\eta(p_c - p_\infty)}{4\zeta} \left( 2(m - \zeta^2) + \frac{\zeta^2 - 3m}{\ln(\rho_*)} \right) + R \frac{\sigma_\infty(\zeta^2 - m) - 2mp_c}{2\zeta},$$

and (A28)

$$\psi(\zeta) = R\zeta \frac{\sigma_\infty + p_c}{m - \zeta^2} (1 + m^2) + R \frac{\eta(p_c - p_\infty)}{m - \zeta^2} \left( m \frac{m\zeta^2 + 1}{\zeta \ln(\rho_*)} - \zeta(1 + m^2) \right).\tag{A29}$$

In order to find the stress state and displacements one should substitute the solution for complex potentials (A28-A29) along with fluid pressure distribution (A26) into (A18-A20). Since the analytical solution for stress tensor components and displacements is too lengthy we will present only the solution for the stress field on the crack ( $\rho = 1$ ) and on the external boundary ( $\rho = \rho_*$ ).

The normal, circumferential, and tangential stresses on the cavity are given, respectively, by:

$$\left. \begin{aligned} \sigma_{\rho\rho}(\rho=1) &= -p_c \\ \sigma_{\theta\theta}(\rho=1) &= 2 \frac{(1-m^2)(\sigma_\infty + Wp_\infty + (1-W)p_c)}{1-2m \cos(2\theta) + m^2} - p_c - \frac{(p_c - p_\infty)\eta}{\ln(\rho_*)} \\ \sigma_{\rho\theta}(\rho=1) &= 0 \end{aligned} \right\}, \quad (\text{A30})$$

where  $W$  is the “weight” parameter:

$$W = \eta \left(1 - \frac{1}{\frac{2c}{a}}\right). \quad (\text{A31})$$

The normal, circumferential, and tangential stresses on the external boundary, respectively, are:

$$\left. \begin{aligned} \sigma_{\rho\rho}(\rho = \rho_*) &= \sigma_\infty + O\left(\frac{1}{\rho_*^2}\right) \\ \sigma_{\theta\theta}(\rho = \rho_*) &= \sigma_\infty + (p_c - p_\infty) \frac{\eta}{\ln(\rho_*)} + O\left(\frac{1}{\rho_*^2}\right) \\ \sigma_{\rho\theta}(\rho = \rho_*) &= O\left(\frac{1}{\rho_*^2}\right) \end{aligned} \right\}. \quad (\text{A32})$$

Neglecting the terms  $O\left(\frac{1}{\rho_*^2}\right)$ , since it is reasonable to assume that the crack length is much smaller than the size of the body, the boundary conditions (A25) for the solid fulfill the equations (A31- A32).

The stresses near the tip of the slit-crack ( $m=1$ ) along the extended crack line and the displacements along the crack sides are of particular importance. Using the analytical solution (A26, A28, A29) and (A18-A19), we obtain the dominant terms of the stress along the extended crack line ( $\rho \rightarrow 1, \theta = 0$ ):

$$\left. \begin{aligned} \sigma_{\rho\rho}(\rho \rightarrow 1, \theta = 0) &= (\sigma_\infty + Wp_\infty + (1-W)p_c) \frac{1}{(\rho-1)} + O(1) \\ \sigma_{\theta\theta}(\rho \rightarrow 1, \theta = 0) &= (\sigma_\infty + Wp_\infty + (1-W)p_c) \frac{1}{(\rho-1)} + O(1) \\ \sigma_{\rho\theta}(\rho \rightarrow 1, \theta = 0) &= 0 \end{aligned} \right\} \quad (\text{A33})$$

Using the expressions (A11) for  $m=1$  and  $R = \frac{a}{2}$ , we obtain the relationship between  $x_1$  and

$\rho$  for the case when  $\rho \rightarrow 1$  and  $\theta = 0$ :

$$(\rho - 1)^2 = 2\left(\frac{x_1}{a} - 1\right). \quad (\text{A34})$$

Using (A33, A34) along with (A14, A15) and neglecting the small terms, we obtain the expression for the stress components in the Cartesian coordinate system:

$$\left. \begin{aligned} \sigma_{11}(x_1, 0) &= (\sigma_\infty + Wp_\infty + (1-W)p_c) \sqrt{\frac{a}{2(x_1 - a)}} \\ \text{For } x_1 \geq a, \quad \sigma_{22}(x_1, 0) &= (\sigma_\infty + Wp_\infty + (1-W)p_c) \sqrt{\frac{a}{2(x_1 - a)}}, \\ \sigma_{12}(x_1, 0) &= 0 \end{aligned} \right\}, \quad (\text{A35})$$

Using the analytical solutions (A26, A28, A29) and (A20), we obtain the dominant terms of the displacements along the crack sides ( $\rho = 1, \mathcal{G} \rightarrow 0$ ):

$$\left. \begin{aligned} u_\rho(\rho = 1, \mathcal{G} \rightarrow 0) &= R \frac{\chi + 1}{2\mu} (\sigma_\infty + Wp_\infty + (1-W)p_c) \mathcal{G} + O(\mathcal{G}^3) \\ u_g(\rho = 1, \mathcal{G} \rightarrow 0) &= R \frac{\chi + 1}{4\mu} \left( 2\left(\frac{\chi - 1}{\chi + 1} - \eta\right)p_c + \frac{\eta(p_c - p_\infty)}{\ln \rho_*} \right) + O(\mathcal{G}^2) \end{aligned} \right\}. \quad (\text{A36})$$

Using the expressions (A11) for  $m = 1$  and  $R = \frac{a}{2}$  we receive the relation between  $x_1$  and  $\mathcal{G}$  for the case when  $\rho = 1$  and  $\mathcal{G} \rightarrow 0$  as the following:

$$\mathcal{G}^2 = 2\left(1 - \frac{x_1}{a}\right). \quad (\text{A37})$$

Using (A36, A37) along with (A16) and neglecting the small terms, we get the expression for the displacements in the Cartesian coordinate system as the following:

$$\left. \begin{aligned} u_1(x_1, 0^\pm) &= a \frac{\chi + 1}{8\mu} \left( 2\left(\frac{\chi - 1}{\chi + 1} - \eta\right)p_c + \frac{\eta(p_c - p_\infty)}{\ln \rho_*} \right) \\ \text{For } x_1 \leq a, \quad u_2(x_1, 0^\pm) &= \pm a \frac{\chi + 1}{4\mu} (\sigma_\infty + Wp_\infty + (1-W)p_c) \sqrt{-2(x_1 - a)/a} \end{aligned} \right\}, \quad (\text{A38})$$

where the sign “ $\pm$ ” denotes the displacements on the upper “+” and lower “-” edges of the crack tip.

## References

- Biot, M. A., 1941. General theory of three-dimensional consolidation. *Journal of Applied Physics* 12, 155-164.
- Goodier, J.N., Hodge, P.G., 1958. *Elasticity and Plasticity: The Mathematical Theory of Elasticity and The Mathematical Theory of Plasticity*, John Wiley & Sons, New York. 152 pp.
- Kolosov, G. V., 1909. *On the Application of the Theory of Functions of a Complex Variable to a Plane problem in the Mathematical Theory of Elasticity*, Ph.D. diss., Dorpat University.
- Lavrent'ev, M. A., Shabat, B. V., 1972. *Methods of Theory of Complex Variable Functions*. Nauka, Moscow. 736 pp..
- Lebedev, N. N., 1937. *Thermal Stresses in the Theory of Elasticity*, ONTI, Moscow-Leningrad.
- Muskhelishvili, N. I., 1977. *Some Basic Problems in the Mathematical Theory of Elasticity*. Springer, Berlin. 768 pp.
- Paterson, M. S., and Wong, T.-F., 2005. *Experimental rock deformation-the brittle field*. Springer, Berlin. 346 pp..
- Rice, J. R., Cleary, M. P., 1976. Some basic stress-diffusion solutions for fluid-saturated elastic porous media with compressible constituents, *Reviews of Geophysics and Space Physics*, 14, 227-241.
- Timoshenko, S. P., Goodier, J.N., 1982. *Theory of Elasticity*. McGraw-Hill, New York. 608 pp.
- Wang, H.F., 2000. *Theory of Linear Poroelasticity with Applications to Geomechanics and Hydrology*. Princeton University Press, Princeton and Oxford. 276 pp.

## **Paper IV**

# Hydraulic fracturing of elliptical boreholes and stress measurements in a highly permeable poroelastic reservoirs

Alexander Y. Rozhko

Physics of Geological Processes (PGP), University of Oslo, P.O. Box 1048 Blindern, N-0316 Oslo, Norway

## Abstract

A criterion for initiation of hydraulic fractures from a plain-strain elliptical cavity is proposed. The elliptical cavity is considered to be in a non-hydrostatic far-field stress state. The fluid is allowed to diffuse through the cavity's wall. The diffusive pore-fluid creates an additional stresses around the cavity due-to coupling of pore-pressure gradients to the rock deformation, which are calculated analytically. I consider two applications of the analytical solution: Hydraulic fracturing of boreholes with the elliptical cross-section and *in situ* stress measurements in highly permeable formations. I demonstrate that small deviations of the borehole's cross-section from the circular have an additional effect on the *breakout pressure* and show that the *fluid leakage* has a strong influence on the fracture *closure pressure*.

## 1. Introduction

The technology of hydraulic fracturing is widely used in industry to stimulate hydrocarbon reservoirs, to enhance permeability in geothermal fields, or, more fundamentally, to measure the state of stress in the Earth's crust [[Economides and Nolte, 2000](#)].

In order to predict hydraulic fracturing fluid pressure, it is typically assumed in calculations that the borehole has a circular cross-section [[Economides and Nolte, 2000](#)]. However, the standard log measurements show that the borehole's cross-section often deviates from circular. [Figure 1 \[online data at Schlumberger web site\]](#) shows a log profile of the large and small axes of borehole, measured by means of six-arm caliper.

In this paper I consider an elliptical cavity (borehole) in a permeable poroelastic medium under non-hydrostatic far-field stress state. The elliptical cavity is filled with

a constant fluid pressure  $p_c$  inside the cavity. Far-field pore fluid pressure  $p_\infty$  is different from the fluid pressure in the cavity ( $p_c \neq p_\infty$ ), therefore the fluid can infiltrate from the cavity into surrounding permeable rock. The diffusive fluid couples to the rock deformation, creating an additional stress field via seepage forces which has additional effects on the initiation of fracture. I considered the steady-state fluid flux from the cavity into surrounding permeable reservoir with homogeneous and isotropic intrinsic properties. Solution in the literature exist only for circular geometry [Haimson and Fairhurst, 1967; Economides and Nolte, 2000]. Since the circle is a particular case of ellipse, the cited-geometry solution is a particular case of the more general solution presented here.

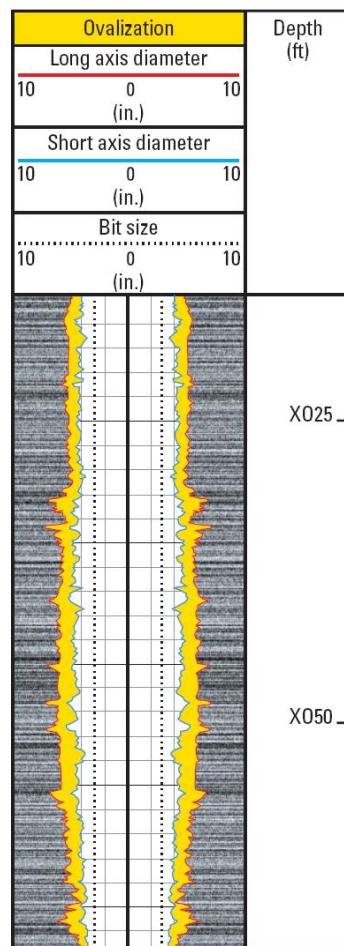


**Figure 1.** Caliper log profile: red and blue curves show long and short axes of borehole; the dashed line is the bit size and the black line is the center of borehole [from Schlumberger web site].

Another important application of presented solution is the *in situ* stress measurements in highly permeable reservoirs. Since, nowadays, it is typically assumed that the



fracture closure pressure correspond to the minimum *in situ* stress, I demonstrate that it is not true in the highly permeable formations, and calculate explicitly the fracture closure pressure, taking into account the poroelastic coupling.

This article is constructed as follows: in [Section 2](#) I describe the problem and its boundary conditions; in [Section 3](#) I present the system of equations which govern the process of fluid filtration in a poroelastic medium and a complex potential method which I use to find the solution of the specific problem; in [Section 4](#) I present a specific solution to the boundary value problem; I discuss results in [Section 5](#) and conclude in [Section 6](#).

## 2. Problem description

Let us consider a vertical borehole drilled in a porous and permeable rock formation that is characterized by a non-hydrostatic horizontal *in situ* stress field, see [Figure 2](#),

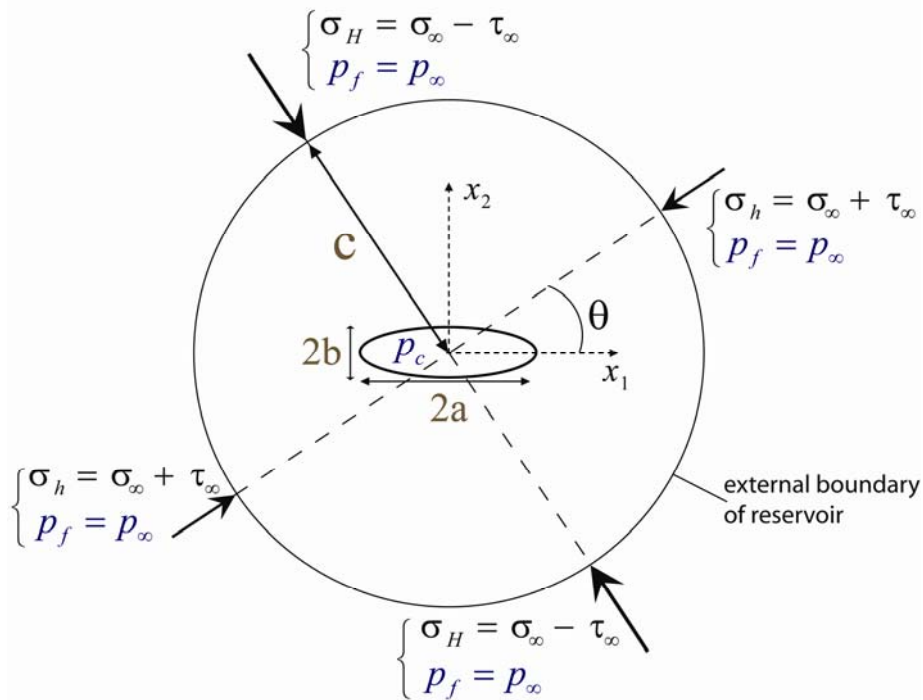


**Figure 2.** Elliptical cavity (borehole), subjected to non-hydrostatic far-field loads  $\sigma_h \geq \sigma_H$ . Here  $\sigma_H$  and  $\sigma_h$  are the far-field major and minor total loads ( $\sigma_\infty \leq 0$  is the far-field mean stress and  $\tau_\infty \geq 0$  is the far-field stress deviator);  $p_c$  is the fluid pressure inside the cavity and  $p_\infty$  is the fluid pressure on the external boundary;  $a$  and  $b$  are the long and short semi-axes of elliptical cavity;  $2c$  is the size of reservoir;  $\theta$  is the angle between the long axis of the cavity and the minor compressive stress;  $x_1$  is the Cartesian coordinate elongated along the major axis.

where the far-field total loads  $\sigma_\infty$  and  $\tau_\infty$  are, respectively, the mean stress and stress deviator;  $p_f = p_\infty$  is the far field pore-fluid pressure;  $p_f = p_c$  is the fluid pressure inside the cavity (borehole);  $\theta$  is the angle between long axis and the minor compressive stress  $\sigma_h = \sigma_\infty + \tau_\infty$ . Coordinate axes  $x_1$  and  $x_2$  coincide, respectively, with the long and short axes of the borehole. The borehole axes are  $a$  and  $b$  with  $a \geq b$ ;  $2c$  is the reservoir size. This problem can be analyzed by assuming plane strain conditions [Detournay and Cheng, 1988].

To simplify the physical consideration of the problem, the loading is decomposed into two modes (Figure 3): (I) a far-field isotropic stress including effects of pore-fluid filtration; and (II) a far-field stress deviator with zero fluid pressure ( $p_f = 0$ ) everywhere.

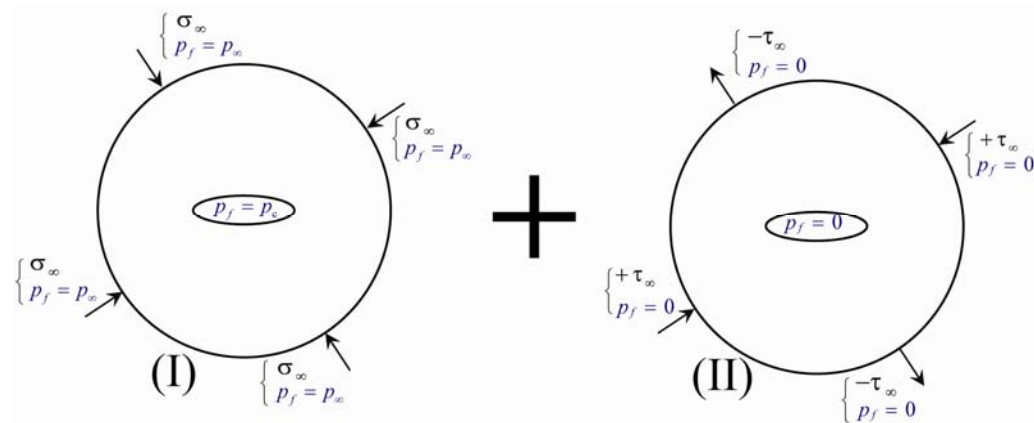


**Figure 3.** Decomposition of the problem shown on Figure 2 on two loading modes. Mode I has hydrostatic far-field compressive stress  $\sigma_\infty$  on the external boundary of reservoir;  $p_c$  is the fluid pressure inside borehole and  $p_\infty$  is the fluid pressure on external boundary. In mode II, the fluid pressure is zero everywhere with pure tension loading  $\tau_\infty$  on the external boundary.

Denoting by the superscript ( $i$ ), the stress induced by loading mode  $i$ , the boundary conditions for each of the loading modes are formulated next.

For loading mode I, the stresses on the cavity wall are:

$$\left. \begin{array}{l} \sigma_{\rho\rho}^I = -p_c \\ \sigma_{\rho\theta}^I = 0 \\ p_f^I = p_c \end{array} \right\} \text{for } \rho = 1; \quad (1)$$

while on the external boundary of reservoir they are:

$$\left. \begin{aligned} \sigma_{\rho\rho}^I &= \sigma_\infty \\ \sigma_{\rho\vartheta}^I &= 0 \\ p_f^I &= p_\infty \end{aligned} \right\} \text{for } \rho = \rho_*. \quad (2)$$

Here  $\rho$  and  $\vartheta$  are curvilinear coordinates, associated with conformal mapping, introduced in [Sub-section 3.3](#) and defined in [Figure 4](#). The meaning of  $\rho=1$  and  $\rho = \rho_*$  is also explained in [Sub-section 3.3](#).

For loading mode II, the stresses on the cavity wall are:

$$\left. \begin{aligned} \sigma_{\rho\rho}^{II} &= 0 \\ \sigma_{\rho\vartheta}^{II} &= 0 \\ p_f^{II} &= 0 \end{aligned} \right\} \text{for } \rho = 1 \quad (3)$$

while on the external boundary of reservoir they are:

$$\left. \begin{aligned} \sigma_{\rho\rho}^{II} &= \tau_\infty \cos(2\theta - 2\vartheta) \\ \sigma_{\rho\vartheta}^{II} &= \tau_\infty \sin(2\theta - 2\vartheta) \\ p_f^{II} &= 0 \end{aligned} \right\} \text{for } \rho = \rho_*. \quad (4)$$

where  $\theta$  is the angle between long axis of borehole  $2a$  and the minimal far-field compressive stress  $\sigma_h = \sigma_\infty + \tau_\infty$ .

Solutions for the induced stress, pore-fluid pressure and displacements are derived in the [section 4](#) for each of fundamental loading modes. First I introduce the system of equations, governing the poroelasticity and describe the general solution, using the method of complex potentials and conformal mapping in [section 3](#).

### 3. Analytical method

This section contain the following subsections:

- 1) the definition of the system of equations for mechanical equilibrium;
- 2) the general solution of this system of equations in Cartesian coordinates using the complex potential method for poro-elasticity;
- 3) the introduction of the curvilinear coordinate system associated with the conformal mapping, which allows finding the solution for the complex geometry; and
- 4) the calculation of the general solution of the equilibrium equations for steady-state poro-elasticity in curvilinear coordinate system.

#### 3.1 System of equations for steady-state (quasi-static) poro-elastic deformation

Following the common approach [*Biot, 1941; Rice and Cleary, 1976; Wang, 2000*], the equations for steady-state fluid filtration in a poro-elastic solid are given by:

- the stress balance equations for the total stress tensor  $\sigma_{ij}$ , without volume forces:

$$\sum_j \frac{\partial \sigma_{ij}}{\partial x_j} = 0; \quad (5)$$

- the steady-state fluid filtration governed by the Laplace equation for fluid pressure distribution  $p_f$ :

$$\sum_j \frac{\partial^2 p_f}{\partial x_j^2} = 0; \quad (6)$$

and a constitutive elastic relationship between the total stress  $\sigma_{ij}$  and the strain  $\varepsilon_{ij}$ :

$$\sigma_{ij} = 2\mu\varepsilon_{ij} + 2\mu\varepsilon_{kk} \frac{\nu}{1-2\nu} \delta_{ij} - \alpha p_f \delta_{ij}; \quad (7)$$

where  $\delta_{ij} = \begin{cases} 1 & \text{if } i = j \\ 0 & \text{if } i \neq j \end{cases}$  is the Kronecker delta and the intrinsic material properties are

the shear modulus  $G$ , the drained Poisson's ratio  $\nu$ , and the Biot-Willis poroelastic constant  $\alpha$  [*Wang, 2000; Paterson and Wong, 2005*]. Substitution of stresses (eq. 7) into the force balance equation (5) renders gradient of the fluid pressure, commonly referred as *seepage forces*, as an additional cause of the solid deformation.

### 3.2 Complex Potential Method for steady-state poro-elasticity

Two-dimensional problems in elasticity can be solved using a complex potential method (CPM), developed by *Kolosov [1909]* and *Muskhelishvili [1977]*. This method has been generalized for thermo-elasticity by *Lebedev [1937]*. In this method, the general solution for the displacements and stresses is represented in terms of three functions: two complex potentials and the temperature distribution [*Goodier and Hodge, 1958; Timoshenko and Goodier, 1982*]. This general solution automatically satisfies the force balance equation and generalized Hooke's law for thermo-elasticity, provided that the function describing the temperature distribution also satisfies the heat conduction equation. The nontrivial part of this method is in satisfying the boundary conditions of the specific problem, which is done by conformal mapping.

The equations for poro-elasticity and thermo-elasticity are identical for steady-state fluid filtration and heat conduction problems. Therefore it is possible to use the

complex potential method, developed for thermo-elasticity, to solve steady-state poro-elastic problems.

According to the CPM, the general solution of equations (5-7) can be written in the form (by convention, compressive stress and strain are positive) [Goodier and Hodge, 1958; Timoshenko and Goodier, 1982; Muskhelishvili, 1977]:

$$\sigma_{11} + \sigma_{22} = 4 \operatorname{Re}[\varphi'(z)] - 2\eta p_f(z, \bar{z}); \quad (8)$$

$$\sigma_{22} - \sigma_{11} + 2i\sigma_{12} = 2[\bar{z}\varphi''(z) + \psi'(z)] - 2\eta \int \frac{\partial p_f(z, \bar{z})}{\partial z} d\bar{z}; \quad (9)$$

and

$$2\mu(u_1 + iu_2) = \chi\varphi(z) - \overline{z\varphi'(z)} - \overline{\psi(z)} + \eta \int p_f(z, \bar{z}) dz. \quad (10)$$

Where the parameters  $\eta$  and  $\chi$  are defined as:

$$\begin{aligned} \text{Plane strain: } \chi &= 3 - 4\nu \text{ and } \eta = \frac{\alpha}{2} \frac{1 - 2\nu}{1 - \nu} \\ \text{Plane stress: } \chi &= \frac{3 - \nu}{1 + \nu} \text{ and } \eta = \frac{\alpha}{2} (1 - \nu) \end{aligned} \quad (11)$$

The integrals in Equations 9-10 are indefinite (without the integration constant) and the superscript “ ’ ” denotes differentiation, i.e.  $\varphi'(z) = \frac{\partial \varphi(z)}{\partial z}$ .

In equations (8-10),  $z = x_1 + ix_2$  is a complex variable,  $x_1$  and  $x_2$  are the usual Cartesian coordinates,  $i = \sqrt{-1}$  is the imaginary unit, and the bar denotes complex conjugation, i.e.  $\bar{z} = x_1 - ix_2$ .  $\varphi(z)$  and  $\psi(z)$  are the complex potentials, which are analytic functions of the complex variable  $z$ , and are derived from the biharmonic Airy function [Kolosov, 1909; Muskhelishvili, 1977]; and  $p^f(z, \bar{z})$  is the solution of Laplace equation (6), given as a function of two complex variables  $z$  and  $\bar{z}$ . By introducing the transformation of coordinates  $x_1 = \frac{z + \bar{z}}{2}$  and  $x_2 = \frac{z - \bar{z}}{2i}$ , the Laplace equation (6) can be rewritten in the form [Timoshenko and Godier, 1982; Lavrent'ev and Shabat, 1972]:

$$\frac{\partial^2}{\partial z \partial \bar{z}} p_f(z, \bar{z}) = 0. \quad (12)$$

The fluid filtration pressure creates stresses at the boundaries of the solid. The boundary value problem, with given stresses or displacements in curvilinear

boundaries, can be solved by finding the complex potentials  $\varphi(z)$  and  $\psi(z)$  using Muskhelishvili's method.

### 3.3 Conformal transformation and curvilinear coordinates

Conformal mapping is a transformation of coordinates that allows solving a problem with a simple geometry (Figure 4a) and transforming its solution for a more complex geometry (Figure 4b). The properties of conformal mapping can be found in [Lavrent'ev and Shabat, 1972].

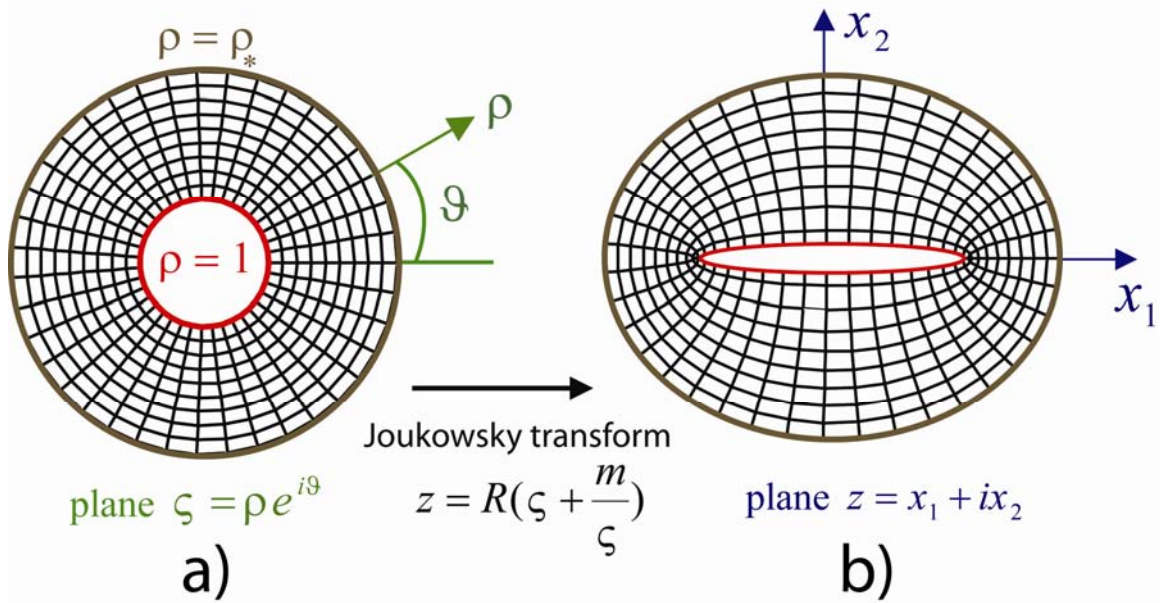


**Figure 4.** Conformal mapping procedure using the Joukowski transform and systems of Cartesian and curvilinear coordinates. The polar coordinates  $\rho$  and  $\vartheta$  of  $\zeta$  - plane are curvilinear coordinates for the  $z$  - plane. The relationship between Cartesian and curvilinear coordinates is given by Joukowski transformation:  $x_1 + ix_2 = R(\rho e^{i\vartheta} + \frac{m}{\rho e^{i\vartheta}})$ . Parameters  $R$  are defined in Subsection 3.3.

The transformation of a circular domain into an elliptical one is given in a unique way by the generalized Joukowski transform:

$$z = R\left(\zeta + \frac{m}{\zeta}\right), \quad (13)$$

where  $R > 0$  is a constant and has a dimension of length;  $m$  ( $0 \leq m \leq 1$ ) is a non-dimensional constant. The complex variable  $\zeta$  is defined in a non-dimensional polar coordinates  $\rho$  and  $\vartheta$  as follows (Figure 4a):

$$\zeta = \rho e^{i\vartheta}, \quad (14)$$

where  $1 \leq \rho \leq \rho_*$  and  $0 \leq \vartheta \leq 2\pi$ ; the internal ( $\rho = 1$ ) and external ( $\rho = \rho_*$ ) boundaries are shown by the red and brown curves, respectively on, [Figure 4a](#).

I use polar coordinates  $\rho$  and  $\vartheta$  in the  $\zeta$ -plane, as a non-dimensional system of coordinates for the  $z$ -plane. The properties of this coordinate system are considered below. Any circle  $\rho = \text{const}$  and radius  $\vartheta = \text{const}$  in the  $\zeta$ -plane ([Figure 4a](#)) are transformed into an ellipse and a hyperbola in the  $z$ -plane, respectively ([Figure 4b](#)). The foci of the ellipse and the hyperbola in the  $z$ -plane coincide ([Figure 4b](#)). As the conformal mapping preserves angles, the two lines  $\vartheta = \text{const}$  and  $\rho = \text{const}$  are perpendicular in the  $z$ -plane. Therefore, the polar coordinates  $\rho$  and  $\vartheta$  can be considered as a curvilinear coordinate system in the  $z$ -plane.

The Cartesian and curvilinear coordinates on the  $z$ -plane are related through:

$$\left. \begin{aligned} x_1 &= R\rho\left(1 + \frac{m}{\rho^2}\right)\cos(\vartheta) \\ x_2 &= R\rho\left(1 - \frac{m}{\rho^2}\right)\sin(\vartheta) \end{aligned} \right\}. \quad (15)$$

If  $\rho = 1$  equations (15) become:

$$\left. \begin{aligned} x_1 &= R(1+m)\cos(\vartheta) \\ x_2 &= R(1-m)\sin(\vartheta) \end{aligned} \right\}. \quad (16)$$

Equations (16) are parametric equations for an ellipse with semiaxis:  $a = R(1+m)$  and  $b = R(1-m)$ . If  $m$  is small, the ellipse's shape approaches circular.

The external boundaries  $\rho = \rho_*$  are represented as brown curves on [Figure 4](#).

If  $\rho_*^2 \gg 1$ , the relations (15) become:

$$\left. \begin{aligned} x_1 &= R\rho_* \cos(\vartheta) + O\left(\frac{1}{\rho_*^2}\right) \\ x_2 &= R\rho_* \sin(\vartheta) + O\left(\frac{1}{\rho_*^2}\right) \end{aligned} \right\} \text{ for } \rho_*^2 \gg 1. \quad (17)$$

Neglecting the terms of order  $O\left(\frac{1}{\rho_*^2}\right)$  one can see that the equations (17) because parametric equations for a circle with the radius  $c = R\rho_*$ .

Thus the relation between  $R, m, \rho_*$  and  $a, b, c$  is the following:

$$\left. \begin{aligned} R &= \frac{a+b}{2}, \quad m = \frac{a-b}{a+b} \\ \text{and } \rho_* &= \frac{2c}{a+b} \end{aligned} \right\}. \quad (18)$$

According to equations (17 and 18), the external boundary in conformal mapping is circular if  $\rho_*^2 = \left(\frac{2c}{a+b}\right)^2 \gg 1$ .

### 3.4 General solution of plane poro-elasticity in curvilinear coordinates

According to Muskhelishvili [1977], the stress and the displacement components in the Cartesian and Curvilinear coordinate systems are related by:

$$\sigma_{11} + \sigma_{22} = \sigma_{\rho\rho} + \sigma_{g g}, \quad (19)$$

$$\sigma_{22} - \sigma_{11} + 2i\sigma_{12} = \frac{\rho^2}{\zeta^2} \frac{\overline{\omega'(\zeta)}}{\omega'(\zeta)} (\sigma_{g g} - \sigma_{\rho\rho} + 2i\sigma_{\rho g}), \quad (20)$$

and

$$u_1 + iu_2 = \frac{\rho}{\zeta} \frac{|\omega'(\zeta)|}{\omega'(\zeta)} (u_\rho + iu_g); \quad (21)$$

where

$$\omega(\zeta) = z = R\left(\zeta + \frac{m}{\zeta}\right). \quad (22)$$

The equations for stresses (8-9) and displacements (10) in the curvilinear coordinate system become:

$$\sigma_{\rho\rho} + \sigma_{g g} = 4\text{Re}(\Phi(\zeta)) - 2\eta p_f(\zeta, \bar{\zeta}), \quad (23)$$

$$\sigma_{g g} - \sigma_{\rho\rho} + 2i\sigma_{\rho g} = \frac{\zeta^2}{\rho^2} \frac{2}{\omega'(\zeta)} \left[ \overline{\omega(\zeta)} \Phi'(\zeta) + \omega'(\zeta) \Psi(\zeta) \right] - \frac{\zeta^2}{\rho^2} \frac{2}{\omega'(\zeta)} \eta \int \frac{\partial p_f(\zeta, \bar{\zeta})}{\partial \zeta} \overline{\omega'(\zeta)} d\bar{\zeta},$$

and

$$2\mu(u_\rho + iu_g) = \frac{\bar{\zeta}}{\rho} \frac{\overline{\omega'(\zeta)}}{|\omega'(\zeta)|} \left( \chi\varphi(\zeta) - \frac{\omega(\zeta)}{\omega'(\zeta)} \overline{\varphi'(\zeta)} - \overline{\psi(\zeta)} + \eta \int p_f(\zeta, \bar{\zeta}) \omega'(\zeta) d\zeta \right); \quad (25)$$

where

$$\Phi(\zeta) = \frac{\varphi'(\zeta)}{\omega'(\zeta)} \quad \text{and} \quad \Psi(\zeta) = \frac{\psi'(\zeta)}{\omega'(\zeta)} \quad (26)$$

Using the properties of conformal mapping ( $\omega'(\zeta) \neq 0$  and  $\omega(\zeta) \neq 0$ ), the Laplace equation (12) becomes:



$$\frac{\partial^2}{\partial \zeta \partial \bar{\zeta}} p_f(\zeta, \bar{\zeta}) = 0. \quad (27)$$

#### 4. Analytical solution

I finally present the analytical solution for each loading modes defined in [Figure 3](#) and via boundary conditions in equations (1, 2) and (3, 4).

##### 4.1 Loading mode I

The analytical solution for loading mode I is derived using Muskhelishvili's method. I do not show the derivation here, since it is quite lengthy, but I demonstrate that this solution fulfills the boundary conditions.

The solution of Laplace equation (27) with the boundary conditions (1, 2) is given by

$$p_f^I(\zeta, \bar{\zeta}) = p_c - (p_c - p_\infty) \frac{\ln(\zeta \bar{\zeta})}{\ln(\rho_*^2)}. \quad (28)$$

This equation can be simplified, using (eq. 14):

$$p_f^I(\rho) = p_c - (p_c - p_\infty) \frac{\ln(\rho)}{\ln(\rho_*)}. \quad (29)$$

The boundary conditions (1, 2) are fulfilled by (eq. 28). Equation (28) gives the solution for pore fluid pressure.

Next, I calculate the complex potentials, which define the solution of problem as follows:

$$\varphi^I(\zeta) = R \frac{\eta p_c \zeta^2 + m}{2\zeta \ln(\rho_*)} + R \frac{\eta(p_c - p_\infty)}{4\zeta} \left( 2(m - \zeta^2) + \frac{\zeta^2 - 3m}{\ln(\rho_*)} \right) + R \frac{\sigma_\infty(\zeta^2 - m) - 2mp_c}{2\zeta}, \quad (30)$$

and

$$\psi^I(\zeta) = R \zeta \frac{\sigma_\infty + p_c}{m - \zeta^2} (1 + m^2) + R \frac{\eta(p_c - p_\infty)}{m - \zeta^2} \left( m \frac{m\zeta^2 + 1}{\zeta \ln(\rho_*)} - \zeta(1 + m^2) \right). \quad (31)$$

In order to find the stress state and displacements one should substitute the solution for complex potentials (30-31) along with fluid pressure distribution (27) into (23-25). Since the analytical solution for the stress tensor components and displacements is lengthy I will present only the solution for the stress field on the cavity ( $\rho = 1$ ) and on the external boundary ( $\rho = \rho_*$ ).

The normal, circumferential, and tangential stresses on the cavity are given, respectively, by:

$$\left. \begin{aligned} \sigma_{\rho\rho}^I(\rho=1) &= -p_c \\ \sigma_{\vartheta\vartheta}^I(\rho=1) &= 2 \frac{1-m^2}{1+m^2} \frac{\sigma_\infty + Wp_\infty + (1-W)p_c}{1 - \frac{2m}{1+m^2} \cos(2\vartheta)} - p_c - \frac{(p_c - p_\infty)\eta}{\ln(\rho_*)} \\ \sigma_{\rho\vartheta}^I(\rho=1) &= 0 \end{aligned} \right\} \quad (32)$$

Where  $W$  is the “weight” parameter calculated as:

$$W = \eta \left(1 - \frac{1}{\ln \rho_*}\right). \quad (33)$$

The normal, circumferential, and tangential stresses on the external boundary, respectively, are:

$$\left. \begin{aligned} \sigma_{\rho\rho}^I(\rho = \rho_*) &= \sigma_\infty + O\left(\frac{1}{\rho_*^2}\right) \\ \sigma_{\vartheta\vartheta}^I(\rho = \rho_*) &= \sigma_\infty + (p_c - p_\infty) \frac{\eta}{\ln(\rho_*)} + O\left(\frac{1}{\rho_*^2}\right) \\ \sigma_{\rho\vartheta}^I(\rho = \rho_*) &= O\left(\frac{1}{\rho_*^2}\right) \end{aligned} \right\} \quad (34)$$

Neglecting the terms of order  $O\left(\frac{1}{\rho_*^2}\right)$ , since it is reasonable to assume that the cavity’s axes are much smaller than the size of the reservoir, the boundary conditions (1, 2) for the solid fulfill the equations (29, 32 and 33).

## 4.2 Loading mode II

In loading mode II, the solution of Laplace equation (27) with the boundary conditions (3, 4) is given by

$$p_f^{\text{II}}(\zeta, \bar{\zeta}) = 0. \quad (35)$$

The solution for complex potentials is obtained by the combination of Muskhelishvili’s solution on the axial extension of the plate, containing an elliptical cavity [*Muskhelishvili, 1977*]. This solution is written as follows:

$$\varphi^{\text{II}}(\zeta) = R \frac{\tau_\infty}{\zeta} e^{2i\theta}, \quad (36)$$

and

$$\psi^{\text{II}}(\zeta) = -R\tau_\infty e^{-2i\theta} \zeta + \frac{R\tau_\infty e^{2i\theta} (1 + \zeta^2 m)}{\zeta(\zeta^2 - m)}. \quad (37)$$

Using (35-37) along with (23-25) I obtain stresses on the borehole’s wall as follows

$$\left. \begin{aligned} \sigma_{\rho\rho}''(\rho=1) &= 0 \\ \sigma_{\theta\theta}''(\rho=1) &= \frac{4\tau_{\infty}}{1+m^2} \frac{m \cos(2\theta) - \cos(2\theta - 2\mathcal{G})}{1 - \frac{2m}{1+m^2} \cos(2\mathcal{G})} \\ \sigma_{\rho\theta}''(\rho=1) &= 0 \end{aligned} \right\}, \quad (38)$$

and stresses on the external boundary of reservoir as follows:

$$\left. \begin{aligned} \sigma_{\rho\rho}''(\rho=\rho_*) &= \tau_{\infty} \cos(2\theta - 2\mathcal{G}) + O\left(\frac{1}{\rho_*^2}\right) \\ \sigma_{\theta\theta}''(\rho=\rho_*) &= -\tau_{\infty} \cos(2\theta - 2\mathcal{G}) + O\left(\frac{1}{\rho_*^2}\right) \\ \sigma_{\rho\theta}''(\rho=\rho_*) &= \tau_{\infty} \sin(2\theta - 2\mathcal{G}) + O\left(\frac{1}{\rho_*^2}\right) \end{aligned} \right\}. \quad (39)$$

This solution corresponds to pure tension loading of a plate containing an elliptical cavity, since the mean stress is zero and the stress deviator has the constant value, i.e.

$$\left. \frac{\sigma_{\rho\rho}'' + \sigma_{\theta\theta}''}{2} \right|_{\rho=\rho_*} = 0,$$

and

$$\left. \sqrt{(\sigma_{\rho\rho}'' - \sigma_{\theta\theta}'')^2 / 4 + (\sigma_{\rho\theta}'')^2} \right|_{\rho=\rho_*} = \tau_{\infty}. \quad (40)$$

## 5. Discussion

Finally, combining solutions for the two loading modes (eqs. 32, and 38) I obtain the following expression for the circumferential load on the borehole's wall:

$$\begin{aligned} \sigma_{\theta\theta} = (\sigma_{\theta\theta}^I + \sigma_{\theta\theta}^{II}) \Big|_{\rho=1} = \\ \frac{4\tau_{\infty}}{1+m^2} \frac{m \cos(2\theta) - \cos(2\theta - 2\mathcal{G})}{1 - \frac{2m}{1+m^2} \cos(2\mathcal{G})} + \frac{2 \frac{1-m^2}{1+m^2} (\sigma_{\infty} + Wp_{\infty} + (1-W)p_c)}{1 - \frac{2m}{1+m^2} \cos(2\mathcal{G})} - p_c - \frac{(p_c - p_{\infty})\eta}{\ln(\rho_*)} \end{aligned} \quad (41)$$

The fracture initiation at cavity's wall takes place when the maximum value of Terzaghi's effective stress ( $\sigma_{\theta\theta}^{\max} + p_c$ ) is equal to tensile strength  $T_0$ , of the rock [Paterson and Wong, 2005], i.e.

$$\sigma_{\theta\theta}^{\max} + p_c = T_0. \quad (42)$$

First, in order to find the maximum value of the circumferential stress at the borehole's wall I rewrite the equation (41) in the form

$$\sigma_{\theta\theta} = -P + \frac{S + T \cos(2\theta) - K \cos(2\theta - 2\mathcal{G})}{1 - M \cos(2\mathcal{G})}, \quad (43)$$

where parameters  $P$ ,  $S$ ,  $T$ ,  $K$  and  $M$  are introduced in [Table 1](#) for reasons of simplicity.

$P = p_c + \frac{(p_c - p_\infty)\eta}{\ln(\rho_*)}$	$S = 2 \frac{1-m^2}{1+m^2} (\sigma_\infty + Wp_\infty + (1-W)p_c)$
$T = \frac{4\tau_\infty}{1+m^2} m$	$M = \frac{2m}{1+m^2} = \frac{a^2 - b^2}{a^2 + b^2}$ , with $m = \frac{a-b}{a+b}$
$K = \frac{4\tau_\infty}{1+m^2}$	$W = \eta(1 - \frac{1}{\ln \rho_*})$ , with $\rho_* = \frac{2c}{a+b}$ $\eta = \frac{\alpha}{2} \frac{1-2\nu}{1-\nu}$

**Table 1.** Substitution of parameters, for reasons of simplicity

After solving the equation  $\frac{\partial \sigma_{\theta\theta}}{\partial \mathcal{G}} = 0$  with respect to  $\mathcal{G}$  and the substitution of the solution for  $\mathcal{G}$  in equation (43), the equation for maximum and minimum values of the circumferential stress at the cavity's wall becomes

$$\sigma_{\theta\theta}^{\max/\min} = -P + \frac{S + (T - KM) \cos(2\theta)}{1 - M^2} \pm \frac{\sqrt{[(MT - K) \cos(2\theta) + MS]^2 + [K \sin(2\theta)]^2 (1 - M^2)}}{1 - M^2} \quad (44)$$

The superscripts “max” and “min” ( $\pm$ ) correspond respectively to the maximum and minimum values of the circumferential stress at borehole's wall. The expression inside the square root is always positive, because  $0 \leq M^2 \leq 1$  according to [Table 1](#), therefore all values of  $\sigma_{\theta\theta}^{\max}$  and  $\sigma_{\theta\theta}^{\min}$  are real.

To calculate the breakdown fluid pressure at fracture initiation one should note that the parameters  $S$  and  $P$  which appear in equation (44) depend on the cavity's fluid pressure  $p_c$ , according to [Table 1](#). In order to calculate the breakdown fluid pressure  $p_c$ , therefore, one should solve the quadratic equation given by [eqs. 42, 44 and Table 1](#) and choose an appropriate root. I will not present the solution of this quadratic

equation here, since this solution is lengthy and easily calculated. I will rather consider two cases of practical interest.

### 5.1 Hydraulic fracturing of nearly circular boreholes

Now, I consider the case when  $m$  is small ( $a \approx b$ ) and  $\rho_* = \infty$  i.e. when the logarithmic term ( $\frac{1}{\ln(\rho_*)}$ ) in parameters  $P$  and  $W$  is omitted. This case is relevant

for elliptical boreholes. Taking the Taylor expansion of (eq. 44) and keeping only linear terms of  $m = \frac{a-b}{a+b}$  I obtain:

$$\sigma_{gg}^{\max/\min} = 2\sigma_\infty + 2\eta(p_\infty - p_c) + p_c \pm 4\tau_\infty - 4\cos(2\theta)(\tau_\infty \pm (\sigma_\infty + \eta(p_\infty - p_c) + p_c)) \frac{a-b}{a+b} \quad (45)$$

Equation (45) in the case when  $a=b$  coincides with the well-known solution obtained by [Detournay and Cheng, \[1988\]](#), (see also [\[Economides and Nolte, 2000\]](#)). Note that I use a sign convention where the compressive stress is negative while the cited authors use an opposite sign convection. The solution of [Detournay and Cheng \[1988\]](#), is the special case of more general solution given by equation (44).

After substituting of the maximum  $\sigma_H$  and minimum  $\sigma_h$  values of the far-field compressive stresses ( $\tau_\infty \geq 0$ )

$$\begin{aligned} \sigma_H &= \sigma_\infty - \tau_\infty, \\ \sigma_h &= \sigma_\infty + \tau_\infty, \end{aligned} \quad (46)$$

the equation (45) can be rewritten in the form:

$$\sigma_{gg}^{\max} = 3\sigma_h - \sigma_H + 2\eta(p_\infty - p_c) + p_c - 4\cos(2\theta)(\sigma_h + \eta(p_\infty - p_c) + p_c) \frac{a-b}{a+b}. \quad (47)$$

Now, solving the failure equation (42) I obtain the following expression for the hydraulic fracturing pressure in the limit, when  $a+b \gg a-b$ :

$$p_c = \frac{-2\sigma_\infty - 4\tau_\infty + T_0 - 2\eta p_\infty}{2(1-\eta)} + \frac{a-b}{a+b} \cos(2\theta) \frac{T_0 - 2\tau_\infty}{1-\eta}, \quad (48)$$

or using (eq. 46) I obtain

$$p_c = \frac{-3\sigma_h + \sigma_H + T_0 - 2\eta p_\infty}{2(1-\eta)} + \frac{a-b}{a+b} \cos(2\theta) \frac{T_0 + \sigma_H - \sigma_h}{1-\eta}. \quad (49)$$

The first term in equation (49) coincides with the well known solution obtained by [Haimson and Fairhurst in 1969](#) (see also [Economides and Nolte, 2000](#)). The second

term gives the correction to the hydraulic fracturing pressure in the case when  $\frac{a-b}{a+b}$  is small.

## 5.2 In situ stress measurements in the highly permeable reservoirs

Now, I consider a cavity with a high aspect ratio i.e.  $a \gg b$  and assume that the logarithmic term  $(\frac{1}{\ln(\rho_*)})$  is negligibly small. Then the equation (44) using Table 1

can be rewritten in the form:

$$\begin{aligned} \sigma_{gg}^{\max/\min} = & -p_c + 2 \frac{\sigma_\infty + \eta p_\infty + (1-\eta)p_c - \tau_\infty \cos(2\theta)}{1-m} \pm \\ & \pm 2 \frac{\sqrt{[\sigma_\infty + \eta p_\infty + (1-\eta)p_c - \tau_\infty \cos(2\theta)]^2 + [\tau_\infty \sin(2\theta)]^2}}{1-m} \end{aligned} \quad (53)$$

If the crack is perpendicular to the minimum compressive stress ( $2\theta = \pi$  and  $\tau_\infty \geq 0$ ), then the equation (53) becomes

$$\sigma_{gg}^{\max} (2\theta = \pi) = -p_c + 4 \frac{\sigma_h + \eta p_\infty + (1-\eta)p_c}{1-m}. \quad (54)$$

Thus, using (54) the failure condition (42) can be rewritten in the form:

$$\sigma_h + \eta p_\infty + (1-\eta)p_c = T_0 \frac{b}{2a}, \quad (55)$$

or in the limit  $\frac{b}{2a} \rightarrow 0$  the failure condition (55) can be rewritten in the form:

$$p_c = -\frac{\sigma_h + \eta p_\infty}{1-\eta}. \quad (56)$$

This equation (56) shows that when the fluid is leaking through the fracture wall it changes the stress-state around the fracture and the fluid closure pressure is not governed by expression  $p_c = -\sigma_h$  as it is typically taken in calculations [Economides and Nolte, 2000; Haimson and Cornet, 2003]. This effect  $p_c \neq -\sigma_h$  was also observed experimentally, it was shown that the reopening fluid pressure (the pressure at which the preexisting crack opens) deviates from closure fluid pressure [Valko and Economides, 1995]. When the fluid pressure opens the preexisting crack, the seepage forces caused by fluid leakage are small, since the fluid does not have enough time to diffuse through the fracture wall. Thus reopening fluid pressure is equal to  $p_c = -\sigma_h$ .

## 6. Concluding remarks

In this paper I have calculated the hydraulic fracturing criterion for the elliptical cavity filled with fluid whose fluid pressure is different from the far-field fluid pressure. Far-field stress state is not hydrostatic. I consider an elliptical cavity in the permeable formation and calculate a seepage forces caused by a coupling of diffusive fluid to the rock deformation. I considered a steady-state fluid filtration from the cavity. This solution corresponds to the “long-time” solution when the fluid flux established a quasi-static distribution. As a possible application for this solution I considered two applications. *The first application* is a hydraulic fracturing of the elliptical boreholes. Since the cross-section of real boreholes could differ from the circular one. I approximated this deviation by an elliptical cross-section. *The second application* is *in situ* stress measurements. The hydraulic fracturing is a common technique for stress measurements. It is shown that if the reservoir is highly permeable than the fracture closure pressure is equal to  $p_c = -\frac{\sigma_h + \eta p_\infty}{1 - \eta}$ . Where  $\sigma_h$

is the minimum *in situ* stress,  $p_\infty$  is the far-field pore pressure;  $\eta = \frac{\alpha}{2} \frac{1 - 2\nu}{1 - \nu}$  here  $\alpha$  is the Biot-Willis poroelastic constant and  $\nu$  is the Poisson ratio. This formula shows that the poroelastic coupling must be taken into account in the highly permeable reservoirs, since nowadays it is assumed in industry that  $p_c = -\sigma_h$ .

**Acknowledgments:** This work was financed by PGP (Physics of Geological Processes) a Center of Excellence at the University of Oslo.

## References

- Biot, M. A., 1941. General theory of three-dimensional consolidation. *Journal of Applied Physics* 12, 155-164.
- Detournay, E., Cheng, A.N.D., 1988. Poroelastic response of a borehole in a non-hydrostatic stress field. *International journal of rock mechanics and mining sciences & geomechanics abstracts*, 25(3): 171-182.
- Economides, M. J., Nolte, K. G., 2000. *Reservoir Stimulation*, 3rd Edition, John Wiley & Sons, New York. 856 pp.

- Goodier, J.N., Hodge, P.G., 1958. *Elasticity and Plasticity: The Mathematical Theory of Elasticity and The Mathematical Theory of Plasticity*, John Wiley & Sons, New York. 152 pp.
- Haimson, B. and C. Fairhurst, Initiation and extension of hydraulic fractures in rock, *Soc. Petrol. Eng. J.*, pp. 310-318, Sept., 1967.
- Kolosov, G. V., 1909. On the Application of the Theory of Functions of a Complex Variable to a Plane problem in the Mathematical Theory of Elasticity, Ph.D. diss., Dorpat University.
- Lavrent'ev, M. A., Shabat, B. V., 1972. *Methods of Theory of Complex Variable Functions*. Nauka, Moscow. 736 pp..
- Lebedev, N. N., 1937. *Thermal Stresses in the Theory of Elasticity*, ONTI, Moscow-Leningrad.
- Muskhelishvili, N. I., 1977. *Some Basic Problems in the Mathematical Theory of Elasticity*. Springer, Berlin. 768 pp.
- Online data: <http://www.slb.com/media/services/evaluation/other/ems.pdf>
- Paterson, M. S., and Wong, T.-F., 2005. *Experimental rock deformation-the brittle field*. Springer, Berlin. 346 pp..
- Rice, J. R., Cleary, M. P., 1976. Some basic stress-diffusion solutions for fluid-saturated elastic porous media with compressible constituents, *Reviews of Geophysics and Space Physics*, 14, 227-241.
- Terzaghi, K. (1943), *Theoretical Soil Mechanics*, John Wiley and Sons, 528 pp., New York.
- Timoshenko, S. P., Goodier, J.N., 1982. *Theory of Elasticity*. McGraw-Hill, New York. 608 pp.
- Valko, P., Economides, M.,J., 1995. *Hydraulic fracture mechanics*. John Wiley & sons. New York. 298 pp.
- Wang, H.F., 2000. *Theory of Linear Poroelasticity with Applications to Geomechanics and Hydrology*. Princeton University Press, Princeton and Oxford. 276 pp.